

LWIR and SWIR
imaging spectroscopy
applied to drill core
and cuttings samples
of Li-pegmatites to
characterize their
modal mineralogy and
to discriminate
between coarse-
spodumene and fine-
spodumene crystals
pegmatite

August 15, 2022

SUPERVISORS:
Dr. Dr. Arjan Dijkstra
Dr. Christopher A. Hecker

This page was left blank.



LWIR and SWIR imaging spectroscopy applied to drill core and cuttings samples of Li-pegmatites to characterize their modal mineralogy and to discriminate between coarse-spodumene and fine-spodumene crystal pegmatite

JEROME W. WEAH

Student number: S2584034

Enschede, The Netherlands, August 15, 2022

Thesis submitted to the Faculty of Geo-Information Science and Earth Observation of the University of Twente in partial fulfillment of the requirements for the degree of Master of Science in Geo-information Science and Earth Observation.

Specialization: Applied Geological Remote Sensing for Earth Sciences

SUPERVISORS:

Dr. Arjan Dijkstra

Dr. Chris Hecker

THESIS ASSESSMENT BOARD:

Dr. Harald van der Werff (Chair)

Dr. Anouk Borst, (External Examiner, KU Leuven, Belgium)

DISCLAIMER

This document describes work undertaken as part of a programme of study at the Faculty of Geo-Information Science and Earth Observation of the University of Twente. All views and opinions expressed therein remain the author's sole responsibility, except explicitly stated otherwise, and do not necessarily represent those of the Faculty.

ABSTRACT

Spodumene is considered one of the most critical lithium-bearing minerals due to its high lithium content and extraction rate. The growing demand for lithium-ion batteries (LiBs) in electric vehicles and short-term supply shortages has led to spodumene mineral being the most explored mineral nowadays and listed lithium companies as a top investment priority. Most junior mining and exploration companies are immensely working to fill the current lithium supply shortage gap. However, the establishment of lithium mines is, without doubt, a significant challenge. The ability to extract lithium from spodumene minerals requires efficient and effective geological and geometallurgical optimization of block models, which is crucial to the effective development of most mining operations. Data flow into the model requires earlier knowledge of spodumene ore, geo-domain (Coarse and fine spodumene crystals size), and waste characterization is crucial. Imaging spectroscopy has been employed as an alternative technique in mapping and characterizing spodumene crystal sizes instead of conventional methods. However, with the limited studies on spodumene mapping and crystals size characterization, this research investigates the usefulness of LWIR and SWIR imaging spectroscopy applied to drill core and cuttings pegmatite samples from Birimian supergroup sequences within the Cape Coast Basin of Ghana in West Africa to map and characterize spodumene crystal sizes (coarse and fine) and other associated minerals. These samples were considered because Birimian supergroup sequences consist predominantly of granites and pegmatites, the key host lithologies of spodumene minerals. The study objectives are to develop a method to characterize spodumene and other associated minerals and to discriminate coarse and fine-spodumene crystals pegmatites based on mineralogy and possibly mineral chemistry. A total of 3 drill cores and 25 cuttings samples were used to acquire hyperspectral images in the VNIR, SWIR, and LWIR wavelength ranges. Only SWIR and LWIR datasets were investigated since important spectral features of the silicates and hydrothermal alteration minerals present in pegmatite host rocks. In addition, 50g of each 25 cuttings samples were used to acquire XRD data for comparison, and five stretched-out powder samples from specific regions on the core for XRD validation.

Spot checks on a few pixels from both SWIR and LWIR datasets were applied to manually validate spectral angle mapper (SAM) classification results. The acquired LWIR and SWIR images were preprocessed for noise reduction and reflectance to emissivity conversion. Red, Green, and Blue (RGB) composites of the out MNF bands were used to facilitate endmembers extraction. The extracted endmembers were then compared to reference spectral libraries for mineral identification and naming, applying spectral normalization and continuum removal by division approach. After the endmembers were named, spectral Angle Mapper (SAM) was applied to generate mineral classification images and mineral quantification based on the dominant minerals species in each pixel, where each pixel represents one mineral species or a mixture. Imaging spectroscopy analysis results identify spodumene minerals by their four reststrahlen features. The deepest but narrow feature at 9038nm and two broad, shallow features at 8322 nm and 11663 nm, followed by a broad weak feature near 10506 nm in the LWIR spectral range. Other identified minerals from LWIR core and cuttings datasets include quartz, microcline, and albite, and a host of mineral mixtures comprised of all identified minerals. SWIR core and cuttings datasets identified hydrothermal alteration minerals, including muscovite, ammonio smectite, montmorillonite, and lepidolite. Mineral spectral differences were based on wavelength position and shape (width, depth, and symmetrical). Their diagnostic reflectance and emissivity features that reflect variability in their mineral composition were used to distinguish identified minerals. One limitation of mineral mapping using hyperspectral LWIR and SWIR lies in the selection of mapping algorithms. Wrong classification lead to misclassification and unclassified pixels resulting in wrong interpretation.

XRD analysis identified all minerals from LWIR dataset. Muscovite and lepidolite were the only SWIR minerals observed from XRD. However, both minerals overlap in their peaks, creating difficulties in distinguishing them. SAM-LWIR cuttings (sieved and washed) were compared to XRD whole-rock cuttings (unsieved and unwashed) data. All identified cuttings minerals from both datasets revealed no statistically significant, positive, or negative relationship, with $R^2 < 0.5$. Linear correlation results of SAM-LWIR modal mineralogy against the mean spodumene crystals size revealed no statistically significant, positive, or negative relationship between modal albite and microcline. Modal spodumene and quartz show a statistically significant positive or negative relationship with spodumene crystal size, with $R^2 = 0.4439$ and $R^2 = 0.1259$. Spodumene crystal's size distinction was based on a predefined threshold value. The mean of spodumene crystals size $\geq 100\mu\text{m}^2$ in a 10cm interval; the interval is described as coarse spodumene crystal pegmatite (P1), otherwise deemed as a fine-crystal pegmatite (P2). Visual inspection of the classified LWIR images shows that dominant quartz and albite-rich zones were associated with 'P1', and dominant quartz-microcline-rich zones were associated with 'P2'.

Keywords: Hyperspectral, LWIR, SWIR, imaging Spectroscopy, Spodumene, Crystal size, Endmembers, XRD

ACKNOWLEDGEMENTS

My deepest gratitude to the almighty God, who has kept me alive and healthy to end this academic sojourn successfully.

I sincerely appreciate the ITC's excellent scholarship committee and financers for granting this fantastic life-changing opportunity.

I want to extend much appreciation to the academic staff of the department of Applied Earth Science (AES), Faculty of Geo-information Science and Earth Observation (ITC), for the intensive knowledge imparted for two consecutive years.

I gratefully acknowledge the fantastic contributions of my supervisors, Dr. Arjan Dskterjar and Dr. Christoph A. Hecker, who have tirelessly contributed insightful comments, guidance, and endless commitment to the research.

Special thanks to my mentor and thesis chairman, Dr. Harald van der Werff, for his guidance throughout my study. His insightful comments during my proposal and mid-term defense have guided me extensively—moreover, his contribution to developing a python Stript positively impacted my research.

Much acknowledgment goes to the Federal Institute for Geosciences and Natural Resources (BGR) in Hannover, Germany, for providing their spectroscopy laboratory facilities to acquire hyperspectral data.

I am grateful to Dr. Martin Schodlok and Dr. Chris A. Hecker for their assistance during data acquisition and initial image data preprocessing.

Many thanks to the COO & Chief Geologist of Atlantic Lithium Ltd, Mr. Lennard Kolff (COO), and Iwan Williams (Exploration Manager) for providing and air transporting pegmatite drill core and RC chips samples via DHL. My salute to the entire staff of Atlantic Lithium Ltd in Ghana.

I sincerely appreciate Sama Resources-Liberia president and CEO Dr. Marc Antonio Audet, for his extensive financial and moral support toward my study.

Lastly, I am grateful to my loving wife, kids, siblings, and friends for their moral support throughout the academic years.

TABLE OF CONTENT

1.	INTRODUCTION.....	1
1.1	Background and Justification.....	1
1.2	Research Objective.....	3
1.2.1	Sub Objectives	3
1.3	Research Questions.....	3
1.4	Study area.....	4
1.5	Geological setting.....	5
1.6	Thesis structure.....	5
2.	DATASET AND METHODS.....	6
2.1	Datasets.....	6
2.2	Methods	6
2.2.1	X-ray diffraction (XRD)	7
2.2.2	Hyperspectral Imaging spectroscopy.....	8
2.2.3	Hyperspectral image acquisition (HSI).....	9
2.2.4	Hyperspectral image pre-processing.....	10
2.2.5	Endmember extraction and Identification.....	12
2.2.6	Spectral Angle Mapper (SAM).....	13
2.2.7	Spodumene crystal size analysis.....	14
2.2.8	LWIR-XRD Comparative Analysis.....	15
3.	RESULTS.....	17
3.1	Image pre-processing.....	17
3.1.1	Spectral subset.....	17
3.1.2	Minimum Noise Fraction (MNF).....	18
3.2	Endmember extraction and identification.....	22
3.2.1	LWIR identified minerals.....	22
3.3	Mineral Mapping.....	28
3.3.1	Spectral Angle Mapper (SAM).....	28
3.4	X-ray diffraction analysis.....	32
3.4.1	Whole-rock XRD analysis of cuttings samples	32
3.5	Quantitative comparison: HSI and XRD on cuttings	33
3.6	Spodumene crystal size analysis	34
3.7	Core versus cuttings Mineralogy	36

4. VALIDATION.....	42
4.1 XRD Validation	42
4.2 Spectral Validation.....	43
5. DISCUSSION.....	46
5.1 Methods	46
5.2 Endmembers identification and extraction	47
5.3 Hyperspectral SAM mineral mapping	47
5.4) Comparison and validation by XRD	49
5.5 Spodumene crystal sizes analysis.....	49
6. CONCLUSION AND RECOMMENDATIONS	51
6.1 Conclusion.....	51
6.2 Recommendations.....	52

LIST OF FIGURES

Figure 2.1: A) whole-rock XRD sample GMS0519 on a glass sample holder. B) Scratched out XRD powdered sample from Quartz mineral crystal in drill core (depth, 70-70.11cm). 7

Figure 2.2: Research methodology workflow 8

Figure 2.3: A) GMS0509 core sample (depth: 70.0 – 70.10) with 12cm length and 3cm width embedded with intact mineral grains including spodumene crystals (black dotted line). B) Cuttings samples include disaggregated mineral crystals in a black shallow circular dish acquired at 1meter intervals. 9

Figure 2.4 shows two examples of the approach used to extract mean endmember spectra from regions of interest based on the color in the RGB-MNF 4,3,2 LWIR image. 12

Figure 2.5 shows two examples of the approach used to manually measure spodumene crystal size(long & short axis) directions from printed-out LWIR classified images 15

Figure 3.1: A) Reflectance spectrum from ROI before spectral subsetting indicating high noise levels(indicated by a black circle). B) Reflectance spectrum after spectral subsetting showing enhanced mineral spectral feature with little spikes (noise). 17

Figure 3.2A: Minimum Noise Fraction (MNF) output bands of drill core sample(GMS0507_depth 66.88 – 67.37m) ranging from band 1 to band 82. The first 10 output MNF bands show enhanced mineral features and less noise. Bands 11 to 82 showed poor image quality, and less mineral information was excluded for further processing. 18

..... 19

Figure 3.2B: Minimum Noise Fraction (MNF) output bands of cuttings sample (GMS0536_depth 79.0 – 80.0m) ranging from band 1 to band 70. The first 10 output MNF bands show enhanced mineral features and less noise. Bands 11 to 70 showed poor image quality, and less mineral information was excluded for further processing. 19

Figure 3.4: Minimum Noise Fraction (MNF) output bands of drill core sample(SWIR_GMS050_depth 66.88 – 67.37m) ranging from band 1 to band 260. The first 12 output MNF bands show enhanced mineral features and less noise. Bands 13 and 14 show break-in SNR, while bands 15 to 217 show poor image quality, followed by bands with continuous signals from 218-260. 20

Figure 3.5: A) Reflectance spectra of a single pixel from LWIR datasets and B) Reflectance spectra from SWIR datasets before MNF (solid black line) showing multiple spikes and after MNF (black dotted line) showing noise reduction effect. C) Emissivity spectrum resulted after reflectance to emissivity conversion. 21

Figure 3.6A: A) Continuum removed emissivity spectrum of spodumene (green) displayed together with the equivalent spectral library resampled of the USGS_GDS74 (black). Note: the black vertical line indicates emissivity minima for clarity. B) Normal emissivity spectrum of spodumene from drill core GMS0507. 22

Figure 3.6B: A) Continuum removed emissivity spectrum of quartz(blue) displayed together with the equivalent spectral library resampled of the USGS_GDS74 (black). Note: the black vertical line indicates emissivity minima for clarity. B) Normal emissivity spectrum of quartz from a core sample(GMS0507) 23

Figure 3.6D: A) Continuum removed emissivity spectrum of microcline(red) displayed together with the equivalent spectral library resampled of the USGS_GDS74 (black). Note: the black vertical line indicates emissivity minima for clarity. B) Normal emissivity spectrum of microcline from drill core GMS0507. 23

Figure 3.6C: A) Continuum removed emissivity spectrum of Albite(yellow) displayed together with the equivalent spectral library resampled of the USGS_GDS74 (black). Note: the black vertical line indicates emissivity minima for clarity. B) Normal emissivity spectrum of albite from drill core GMS0507. 24

Figure 3.6E: the so-called mixed spectrum of spodumene-quartz-albite-microcline (cyan) from core images. Note: the feature (in red circle) was observed to be associated with quartz-spodumene mixture, while the feature

(in yellow circle) was determined to be associated with albite and microcline. These features were observed in all samples of the study datasets. 25

Figure 3.7A: Spectral profiles: A) continuum removed lepidolite (red) spectra from core image and USGS_NMNH105538(black). Note: the black vertical dash line indicates spectral absorption features which can be used to identify lepidolite. B) Normal reflectance spectrum of lepidolite from drill core GMS0507. ... 25

Figure 3.7B: Spectral profiles: A) continuum removed muscovite (green) spectra from core image and USGS_GDS117(black). Note: the black vertical dash line indicates spectral absorption features, which can be used to identify muscovite. B) Normal reflectance spectrum of muscovite from drill core GMS0507 26

Figure 3.7C: Spectral profiles: A) continuum removed ammonio-smectite (yellow) and montmorillonite(blue) Muscovite (green) spectra from core image and reference spodumene from USGS_Sca-2a. Note: the black vertical dash line indicates spectral absorption features, which can be used to identify the minerals. B) Normal reflectance spectrum of montmorillonite and ammonio smectite from drill core GMS0507 27

Figure 3.8: LWIR core samples (left), Spectral Angle mapper(SAM) classification showing minerals match for spodumene, Quartz, Albite, Microcline, and mineral mixture, and SWIR core (right), SAM classification showing minerals match for muscovite, lepidolite, ammonio-smectite and montmorillonite. The color pixels represented by each mineral are more similar to the reference spectrum than darker pixels(unclassified). 3 drill core samples section are presented for illustration purposes: GMS0507 (65.90-66.00m), GMS0508 (68.40-68.50m), GMS0509 (70.00-70.10m)..... 30

Figure 3.9: Spectral angle mapper images of LWIR cuttings samples showing match for spodumene, Quartz, Albite, Microcline, mineral mixture, and unclassified pixels. The color pixels represented by each mineral are more similar to the reference spectrum than darker pixels(unclassified)..... 31

Figure 3.10: Figure 3.9: Spectral angle mapper images of LWIR cuttings samples showing match for muscovite, lepidolite, ammonio-smectite, montmorillonite, and unclassified pixels. The color pixels represented by each mineral are more similar to the reference spectrum than darker pixels(unclassified). Note: due to the spot size of the SWIR camera (6 cm), SWIR cuttings samples were chopped off at the peripheral because the sample holder was larger than the camera field of view..... 32

Figure 3.11: A) Representative whole-rock XRD diffractogram of sample GMS0514 and sample GMS0520 showing peaks of quartz, albite, microcline, spodumene, and muscovite or lepidolite..... 32

Figure 3.12: Correlation plots of HSI (LWIR) versus XRD mineral abundances on 25 cuttings samples for spodumene(green), quartz(blue), microcline(red), and albite(yellow) 33

Figure 3.13: Graphical plots of HSI (LWIR) versus XRD mineral abundance on 25 cuttings samples for spodumene(Green), quartz(blue), albite(yellow), microcline(Red), and XRD data for each mineral in orange. 34

Figure 3.14:The mean of the three largest spodumene crystals area(cyan) in each 10 cm interval plotted together with model mineralogy for quartz (blue), albite (yellow), microcline (red), and spodumene (green) relative to their depths. 35

Figure 3.15: A) Spodumene crystals size(area, in mm²) distribution plot, B) Model mineralogy (right) for quartz (blue), albite (yellow), microcline (red), and spodumene (green) plotted against their relative depths..... 36

Figure 3.16: Correlation plots of modal % of albite, microcline, quartz, and spodumene, based on SAM- LWIR versus spodumene crystal size (area, in mm², of the three largest spodumene crystals in each interval) for the available core interval of continuous ~4m core sample. 36

Figure 3.17: A,B,C) Correlation plots of HSI-SAM core versus cuttings of 100cm samples at the same depth intervals. D,E,F) HSI-SAM core versus XRD cuttings of 100cm samples at the same depth intervals. 37

..... 38

Figure 3.18: A) Correlation analysis of SAM-LWIR core (GMS0507) and cuttings (GMS0523) mineralogy plotted on a one-to-one relationship line. B) SAM-LWIR core (GMS0508) and cuttings (GMS0525) mineralogy C) SAM-LWIR core (GMS0509) and cuttings (GMS0526) mineralogy 38

..... 40

Figure 3.19: A & B) Graphical plots of SAM-LWIR core and XRD cuttings mineral abundance, C & D) SAM-LWIR core samples and SAM-LWIR cuttings mineral abundance, E & F) SAM-LWIR cuttings mineral abundance and XRD cuttings mineral abundance for continuous ~4m core sample against their relative depths. 41

Figure 4.1: scratched-out powders XRD spot-based analysis pattern of spodumene(B & E), Microcline (A & C), and Albite (D). Diffractograms of each sample show dominance of all three minerals, indicated by their color dot and sharp peaks. All scratched powders samples show a minor peak of other minerals present as inclusion..... 42

Figure 4.3: A to D, showing spectral validation on specific spots from LWIR SAM classified images for microcline, spodumene, and albite with corresponding XRD diffractogram (left). Note: the black circles indicate pixel location..... 44

Figure 4.5: A to D, showing cuttings spectral from saturated pixels and background spectrum from the sample holder. A and C) Background spectrum, B and D) spectrum from saturated pixels. Note: the black circles indicate pixel location..... 45

LIST OF TABLES

Table 2.1: Image processing activities and justifications	11
Table 2.2: threshold value for each endmember used in the rule classifier	14
Table 3.3: Percentage estimate of 25 cuttings samples from SAM classification	29
Table 4.1: Five samples scratched out core samples from XRD analysis and HSI validation. The highlighted colors for each mineral are derived from the SAM classification of the cores. The approximate depth of each scratched spot within a 10cm interval. Note: values in bold indicate the abundance percentages per scratched spot.....	42

LIST OF APPENDICES

Appendix 1: Hyperspectral classified SAM-LWIR core images of 100cm core section (GMS0507)	56
Appendix 2: Hyperspectral classified SAM-LWIR core images of 100cm core section (GMS0508)	57
Appendix 3: Hyperspectral classified SAM-LWIR core images of 100cm core section (GMS0509)	58
Appendix 4: Hyperspectral classified SAM-SWIR core images of 100cm core section (GMS0507).....	59
Appendix 5: Hyperspectral classified SAM-SWIR core images of 100cm core section (GMS0508).....	61
Appendix 6: Hyperspectral classified SAM-SWIR core images of 100cm core section (GMS0509).....	63
Appendix 7: Twenty-five classified SAM- LWIR cuttings images.....	65
Appendix 8: Twenty-five classified SAM- SWIR cuttings images.	66
Appendix 9: Twenty-five XRD diffractogram cuttings samples(unsieved and unwashed)	68
Appendix 10: Modal mineralogy proportion database of quartz, microcline, albite, and spodumene	71
Appendix 11: Twenty-five XRD cuttings samples mineral abundance database.	72
Appendix 12: Database used for the quantitative analysis, including Hyperspectral imaging and XRD.	73
.....	73
Appendix 13: spodumene crystals size analysis database	74
Appendix 14: Correlation statistical summary output of spodumene, quartz, microcline, and albite against mean spodumene crystal size.....	75
.....	76
Appendix 15: Hyperspectral cameras specification.....	77
Appendix 16: XRD sample preparation procedures	78
Appendix 17: XRD measurement using Bruker D2 phaser	79
Appendix 18: Twenty-five cuttings samples preparation procedures for hyperspectral imaging	80

1. INTRODUCTION

1.1 Background and Justification

Energy transition is crucial to the safety of our environment in reducing global energy-related CO₂ emissions from the automobile industry (Herzog et al., 2005). This transition will need lithium for battery production for electric vehicles. Research has found that lithium-ion batteries were considered the most promising cleaner battery technology due to their high energy density, efficiency, durability, and less economical (Grosjean et al., 2012). Compared with other batteries chemistry, lithium-ion batteries have a much higher voltage, recharge without affecting the complete life cycle, have twice the energy density, and have a relatively low discharge rate (Grosjean et al., 2012). These advantages make lithium-ion batteries superior to electrifying vehicles and a good contender for grid storage. Lithium-ion batteries can store generated power and supply electrical power in case of shortage or high demand, which varies daily, and seasonally (Chen et al., 2020).

Lithium was first extracted from brine by evaporation in ponds using solar energy, constituting 60% of global identified reserves (Grosjean et al., 2012). Significant increasing demand for lithium-ion batteries for electric vehicles and low supply shortages has listed lithium companies as top investment priorities for major financial institutions (Morgan, 2015). This has increased exploration and mining companies to fill the current lithium supply gap, even though the development of lithium mines is, without debt, a significant challenge (Tadesse et al., 2019). However, lithium has been extracted from lithium-bearing pegmatite, constituting 50% of global lithium production (Greim et al., 2020). The dominant lithium-bearing mineral includes spodumene, petalite, lepidolite, Amblygonite, and eucryptite. Of these minerals, spodumene (LiAlSi₂O₆) is considered the most predominant economic lithium-bearing mineral (Tadesse et al., 2019). Lithium mineral resources extraction is a complex process that requires efficient geological and metallurgical studies and model optimization in distinguishing ore from waste that contributes significantly throughout a mine life cycle (Vieceli et al., 2017). As a result, data incorporated into the model should be accurate, consistent, and substantial in delineating ore from waste. The most critical characteristics of spodumene ore evaluation are crystal size and their mineralogical association, which play a crucial role in model optimization at every stage of exploration and mining (Menendez, Vidal, J. Torano, 2004). These characteristics are crucial to mining and ore processing operations and require automated techniques for mineral mapping and crystal size measurement other than conventional mineral logging understanding that potentially could have financial consequences (Tadesse et al., 2019).

Spodumene ore processing requires coarse size fraction due to less extensive energy and high density in liberating spodumene from its gangue constituent minerals such as quartz and feldspar in the beneficiation process involving sizing, grinding, flotation, gravity, and heavy mineral separation to obtain lithium mineral. Moreover, coarse-size fraction minimizes lithium losses to floating gangue minerals other than fine-sized fractions (Tadesse et al., 2019). These advantages make coarse fraction a key priority for most mining companies in distinguishing coarse and fine crystal size intervals from drill core and cuttings. A promising lithium project currently operating in Ghana faces a challenge in distinguishing between coarse and fine spodumene crystal pegmatite in cuttings samples because cuttings samples are crushed by a diamond drill bit at the bottom of drill holes and flushed up to the surface with circulating drilling fluid, thus creating difficulties in distinguishing both crystals types (Len Kolff, Iron Ridge Resources, personal communication, November 2021). In addition, importance is attached to RC drilling (cuttings) in minimizing exploration costs than diamond drilling (core). Atlantic Lithium geologists classify pegmatite crystal size intervals based on an estimation of mean spodumene grain size, with intervals having a mean spodumene grain size of ≥ 20 mm as 'coarse grained' or 'P1' and ≤ 20 mm as 'fine grained' (Len Kolff, Iron Ridge Resources, personal communication, November 2021).

Different methods are used to distinguish grain size, including direct measurements such as sieving, gravimetric sedimentation, laser diffraction, etc. These techniques provide precise and reliable measurements for grain size fractions. However, they are destructive, time and material-consuming, and labor-intensive (Jacq et al., 2019). Recently, these techniques limitations have been addressed using imaging spectroscopy, a rapid and non-destructive application. For example, Jacq et al. (2019) applied integrated visible near-infrared (VNIR) and short-wave infrared (SWIR) hyperspectral imaging to estimate particle size distribution and fractions based on mineral percentages using partial least square regression(PLSR) models. Even though hyperspectral imaging spectroscopy shows potential for estimating particle size, the choice of methodology and appropriate techniques are paramount for evaluation.

Several methods have been extensively employed in mapping rock-forming minerals, including electron microprobe, Laser Ablation (LA) Inductively Coupled Plasma Mass Spectrometer (LA-ICP-MS), and Micro-XRF (Aylmore et al., 2018; Selway et al., 2005). However, these methods have been used adequately despite their limitation in mapping spodumene. Infrared spectroscopy has utilized its potential as an alternative method in mineral mapping in the wavelength range of VNIR(visible -near-infrared), LWIR (longwave), and SWIR (short-wave) infrared spectroscopy(Hecker et al., 2010; Kraal and Ayling, 2019; Kartika P. Savitri et al., 2021; Yuen and Richardson, 2010). Infrared imaging spectroscopy provides an alternative to capturing continuous datasets and spatial distribution between various mineral types (Greenberger et al., 2015). Moreover, with a fine spatial resolution (pixel size), imaging spectroscopy is better for detecting mineral spatial distribution in drill core and cuttings samples in the VNIR, SWIR, and LWIR spectroscopy (Kraal and Ayling, 2019). For most non-hydroxyl-bearing minerals, including spodumene, LWIR imaging has proven ideal for semi-quantitative and spatial distribution due to minerals composition and structural state having unique spectral signatures. Spectral signature of spodumene and other minerals such as quartz and feldspar are characterized by their reststrahlen features in the LWIR wavelength range ((Hecker et al., 2019, 2010; van der Meer et al., 2012). These spectral features are pronounced around 8000 – 11500 nm due to vibrational processes (Clark, 1999; 1990).

Therefore, this research investigates the potential of LWIR and SWIR imaging spectroscopy in characterizing and discriminating coarse and fine spodumene crystal pegmatite based on mineralogy and possibly mineral chemistry applied to drill core as a proxy for "cuttings" samples of the Ewoyaa lithium deposit in Ghana, West Africa. The study samples are limited to spodumene pegmatite acquired by Atlantic lithium Resources in Ghana, Birimian supergroup, a Proterozoic volcano-sedimentary basin of the West African Birimian craton.

1.2 Research Objective

The main objective is to develop a method for characterizing and discriminating fine and coarse spodumene crystal pegmatite applied to the drill core as a proxy for "cuttings" samples of the Ewoyaa lithium deposit in Ghana.

1.2.1 Sub Objectives

The following sub-objectives will be addressed to achieve the main objective of this research.

1. To assess spectral differences and separability of typical lithium pegmatite minerals in the LWIR spectroscopy.
2. To develop a classification scheme based on minerals assemblage and possibly mineral chemistry that can distinguish fine and coarse spodumene crystals pegmatite applied to drill core and test its application to cuttings of the Ewoyaa lithium deposit in Ghana using LWIR and SWIR imaging spectroscopy.
3. To compare quantitative mineral abundance in the LWIR classified images to X-ray Diffraction (XRD).

1.3 Research Questions

1. Are typical lithium minerals spectral sufficiently different from literature and existing published spectral libraries, so they can be used to differentiate these minerals from each other?
2. Which mineral(s) are associated with fine and coarse spodumene crystal pegmatite in the LWIR classified images?
3. Which mineral(s) are spectrally confused and spatially associated with spodumene in the LWIR classified images?
4. Do fine and coarse spodumene crystal pegmatite from the Ewoyaa deposit have different mineral compositions than other spodumene pegmatite deposits?
5. How well can LWIR spectroscopy quantify spodumene and other associated minerals composition compared to X-ray Diffraction (XRD)?

1.4 Study area

The study area is located in Ghana, West Africa, approximately 100km southwest of Accra, the capital city. The study area is north of Salt Pond, in the central region, and falls within the Mfantseman Municipality, the district capital of Salt Pond. Over decades, the study area has undergone mapping, trenching, and bulk sampling by the Ghana geological survey from 1963 to 1965, which gives rise to the Ewoyaa lithium deposit discovery (Kesse, 1985). The research-specific study is the Ewoyaa lithium exploration project operated by Atlantic lithium limited, Ghana, West African Craton. The area was selected for four reasons: first, the availability of datasets such as drill core and cuttings samples. Secondly, the Ewoyaa prospect will be considered the first lithium mine in West Africa based on its indicated mineral resource. The prospect will also be considered a spodumene research site for future exploration and mines for other West African lithium projects. Thirdly, No advanced mineralogy study has been conducted on this pegmatite deposit using hyperspectral imaging spectroscopy to obtain a detailed mineralogical composition. Lastly, with an indicated mineral resource, Atlantic lithium company in Ghana has a real-world problem that needs solving in distinguishing coarse-grained from fine-grained spodumene pegmatite in cuttings before the extraction process.

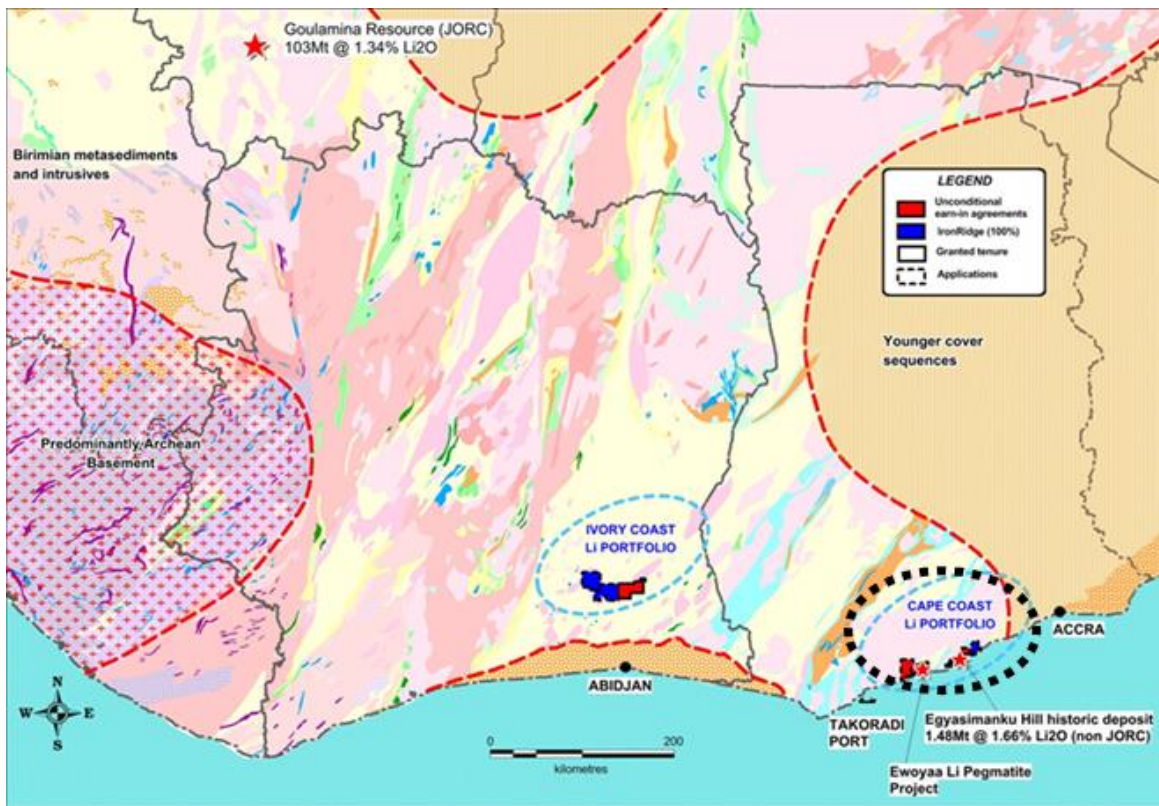


Figure 1.1: Study area (black dotted circle) map showing regional geology. Source: Atlantic Lithium Ltd.

1.5 Geological setting

The research study area is located on the western margin of the Kibi-Winneba Volcanic Belt within the Cape Coast Basin of Ghana, which covers 45% of the country's geological areas (Leube et al., 1990). It comprises a thick sequence of steeply dipping metasediments and metavolcanic of proterozoic age (2.2-2.3 Ga). It is generally referred to as the Birimian Supergroup (Leube et al., 1990). These Birimian supergroup sequences extend approximately 200km along strike north-east trending volcano-plutonic belts and volcano-sedimentary basins. These sequences appear to contain rocks representing partly lateral facies equivalents, and most sediments appear to be derived from the volcanic belt (Dzibodi-Adjimah, 1993). Birimian supergroup rocks folding, metamorphism, and high-strain along the boundaries of the Birimian basin are derived from the Eburnean (2.1 Ga) tectono-thermal orogenic event, producing isoclinal folding and metamorphism that reached the greenschist to lower amphibolite facies (Perrouy et al., 2012). The Birimian basins were intruded by extensive syn and post-tectonic granitoids during the Eburnean orogeny event (2116 -2088 Ma), including the extensive Cape Coast undifferentiated biotite granitoid pluton, which is the dominant geological feature of this region (Hirdes et al., 1992). Pegmatite intrusions, spatially associated with the pluton's margin, have been dated to 2072 Ma; they formed as a result of metasediment anatexis and may be considered the last event of the Eburnean plutonism (Hirdes et al., 1992). The local geology is underlined by three metamorphosed schist: mica schist, staurolite schist, and garnet schist. Several granitoid intruded the basin meta-sediments as small plugs. These granitoid ranges in composition from intermediate granodiorite (medium-grained) to felsic leucogranites (coarse-grained). Pegmatite intrusions generally occur as sub-vertical dykes striking North-Northeast and dipping sub-vertically East to Southeast. Pegmatite thickness varies across the project, with thinner mineralized units width between 4m and 12m; and thicker units width between 30m and 60m at the surface. Continuous structure of the mineralization strike length exceeds 20km (Len Kolff, Atlantic lithium, written comm., 2022). Pegmatite deposit was drilled to a vertical depth of approximately 180m, while the mineralized zone was modeled from the surface to a depth of approximately 200m. These estimates were based on good quality reverse circulation ("RC" or cuttings) and diamond core ("DD") drilling data. Drill hole spacing was predominantly 40m by 40m in the well-drilled mineralized portions and 80m by 80m to 100m by 100m across the strike length of the known mineralization. Geometallurgical studies identified two types of spodumene pegmatite based on their coarse-grained and fine-grained size fractions and relative weathered equivalents (IronRidge Resources, 2021).

1.6 Thesis structure

This thesis is categorized into five chapters. [Chapter 1](#) introduces the research background, justification, objectives, research questions, study area, and geological setting. [Chapter 2](#) discussed datasets, sample preparation, and methodology, including image data acquisition, image pre-processing, endmember extraction and identification, mineral mapping, quantitative comparison of LWIR and XRD mineral abundances, and spodumene crystal size analysis. [Chapter 3](#) presents results, including image pre-processing and processing, quantitative comparison of LWIR and XRD mineral abundance, and spodumene crystal size analysis. [Chapter 4](#) Validation (imaging spectroscopy and XRD), [Chapter 5](#) provides an in-depth discussion of the methods applied and the acquired results relating to the research's findings. [Chapter 6: Conclusion and Recommendations.](#)

2. DATASET AND METHODS

Data used in this study include pegmatite cores and cuttings samples provided by Atlantic lithium limited in Ghana. Both samples were used to acquire hyperspectral VNIR, SWIR, and LWIR images and XRD analytical data. The acquired LWIR and SWIR images were pre-processed to extract spectral information related to crucial mineralogies relevant to the research. The process hyperspectral images were analyzed along with XRD data to validate the usefulness of LWIR and SWIR imaging spectroscopy in identifying and mapping minerals contained in the investigated dataset. Only SWIR and LWIR datasets were investigated since important spectral features of the silicates and hydrothermal alteration minerals are present in the study dataset. The research methodologies include: acquiring VNIR, SWIR, and LWIR image data cubes, pre-processing and processing, data analysis and interpretation, and spodumene crystal size analysis. Image processing software used includes ENVI 5.6.1 + IDL 8.8.1 by Harris Geospatial solution, hyperspectral python (Hyppy3) by Wim Bakker (ITC), Microsoft Excel, and Classtract.pro algorithm (IDL source file) by Dr. Harald Werff (ITC).

2.1 Datasets

Three drill core samples with a total length of 4.46 meters at varying depths and 25 cuttings samples with a total length of 25 meters weighing 100g each were recovered at every 1-meter depth interval. These samples were extracted from twin (parallel) drill holes (GDD00** and GRC00** are displayed due to a confidentiality agreement with the company) within the high-grade spodumene pegmatite orebody. The received samples contain spodumene and other associated minerals extracted from Birimian supergroup sequences comprised of volcano-plutonic belts and volcano-sedimentary basins. Core samples were sawed in the length direction and packaged in labeled plastic. Cuttings samples were directly from the rig and not laboratory pulp samples. The samples contained varying fine to coarse particle sizes packaged in labeled plastic. Both samples were placed in a sealed rubber container before delivery.

The company extracted cuttings samples using EDM2000 and UDR300 truck-mounted mud rotary drill rigs. Bentonite drilling mud was used as a viscous drilling fluid. It is pumped down to the drill rod and circulates back to the borehole transporting cuttings samples into a pick-up pit at the surface by compressed air. Drill core samples were extracted using Sandvik ED 740/3 drill rig. The extraction process requires a drill rod rotating and a diamond bit that spanned into the ground. As the drill bit penetrates through the rock, solid rock is taken into the circular opening at the end of the bit into the core tube and recovered at the surface. Drill samples barrel were loaded onto the system with a plastic liner and then lowered at a depth of more than 180meters. Representative drill core samples were later sawed at 1meter intervals to obtain the research samples. (Len Kolff, Atlantic lithium, written comm., 2022).

2.2 Methods

Cuttings samples were prepared at the GeoScience laboratory, ITC Faculty, University of Twente, to remove bentonite fluid used during drilling, which might cause spectral confusion with other minerals. Sample preparation procedures include splitting, sieving, washing, and drying moderately. Each 100g sample was initially oven dry at 105 °C to remove moisture content and split into two equal half of 50g each using a Riffle sample splitter. Splitting procedure was done by pouring the 100g sample material into the Riffle splitter and automatically dividing it into two equal portions that discharged into two separate pans attached at the bottom of the splitter. The splitter allows a representative sample to be segregated from a bulk sample quantity without changing its properties. Half of the 100g was sieved at >0.5mm; coarse size fractions were washed and rinsed with distilled water and gently oven-dried for 72 hours at 60°C to preserve hydrated minerals. Sieving was done to segregate coarse particles from fines for hyperspectral imaging. The other half of the 100g sample was kept and later prepared for XRD analysis. Cuttings samples preparation workflow is presented in *appendix 18*. These procedures were suggested by supervisors Dr. Chris and Dr. Arjan and were initially demonstrated by Dr. Arjan.

2.2.1 X-ray diffraction (XRD)

Whole rock XRD samples were collected from the remaining 50g of each 25 cuttings samples. Samples were milled using PM 200 with two steel jaws-crusher enclosed with 7 silicon balls each for homogeneous rock powders. Samples were initially oven-dried at 105°C for moisture evaporation. Each steel jaw contains 30g of sample to obtain the instrument's balance. Samples were milled for 10 minutes at 450 rpm (rounds per minute). In addition, 5 powdered samples material (<50 mg) from targeted locations on the core were scratched with a tungsten-carbide scribe, collected on a sheet of aluminum foil, and transferred onto a sample holder consisting of a silicon wafer for XRD analysis. This method was employed to validate spectral angle mapper(SAM) classification results.

Analyses of 25 whole-rock XRD powdered samples on a non-oriented sample holder were measured using a Bruker D2 phaser instrument (Bruker Corporation, Billerica, MA, USA) at the GeoScience Laboratory of the Faculty of Geo-Information Science and Earth Observation, University of Twente. The instrument is equipped with an LYNXEYE detector and a CuK α x-ray source with a wavelength of 1.54184 Å, operated at 10 mA and 30 kV, which acquires a composite, bulk x-ray spectrum of a powder. The operator compares the spectrogram to mineral spectra in the library until an operator is happy with the match. The output is a semi-quantitative estimate of the proportions of the different selected matched minerals. Diffractogram pattern was recorded between $2\theta = 6$ to 80° at a scan step of 0.012 and integration time of 1s. In addition, a detector slit of 8 mm and a standard divergence slit of 0.6 mm were used to control areas of the illuminated sample and enhance the measurement's resolution. Measurement of targeted scratch samples was carried out using the same procedures as the whole rock.

Mineral phase identification and semi-quantification of relative mineral abundances of each phase based on the pattern relative heights were done using an automatic search and manually searching by mineral name in DIFFRAC. EVA version 3.1 software against an inbuilt reference mineral database. Performing phase identification, The below-listed structure files of each mineral phase was generated from Diffrac.EVA library. The software generated several best-match peaks, but the user selected the most likely mineral peaks from the diffractogram. Structure files include: Quartz (COD 1011176), spodumene (COD 9000346), Microcline (COD 9000943), Albite (COD 9002196), and Muscovite (COD 9001054), petalite (COD 9008304), Montmorillonite (COD 9002779) and lepidolite (COD 9000628). Petalite and montmorillonite show no prominent peaks but minor traces.

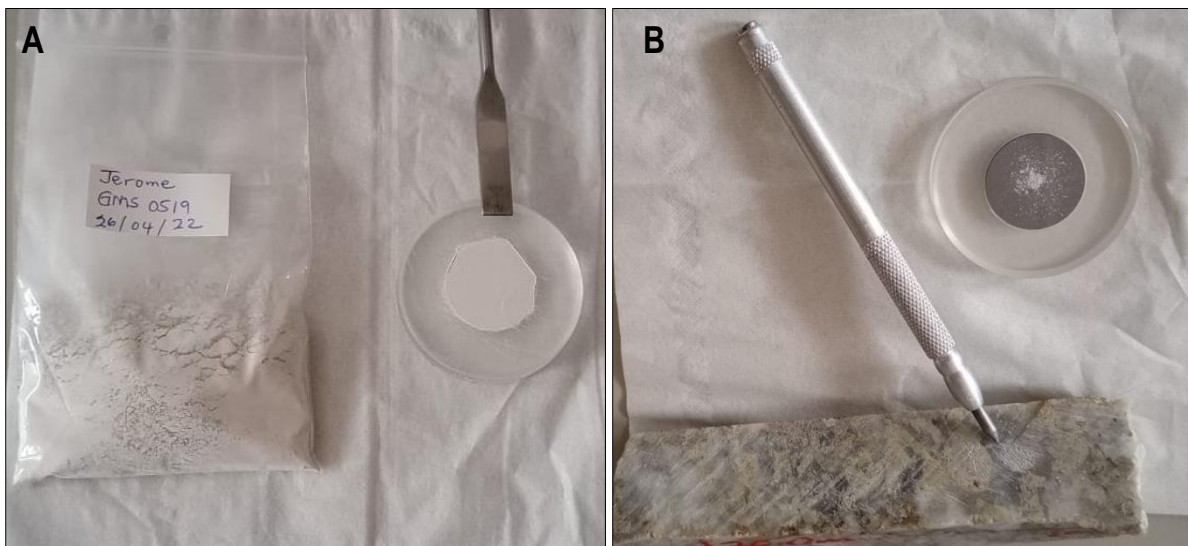


Figure 2.1: A) whole-rock XRD sample GMS0519 on a glass sample holder. B) Scratched out XRD powdered sample from Quartz mineral crystal in drill core (depth, 70-70.11cm).

2.2.2 Hyperspectral Imaging spectroscopy

Hyperspectral datasets acquired include visible near-infrared (VNIR), shortwave-infrared (SWIR), and longwave-infrared (LWIR) images. Methodologies include image data acquisition, image pre-processing, and processing and interpretation. These methods are elaborated in the below sections and summarized in the methodology flow chart shown in figure 2.2.

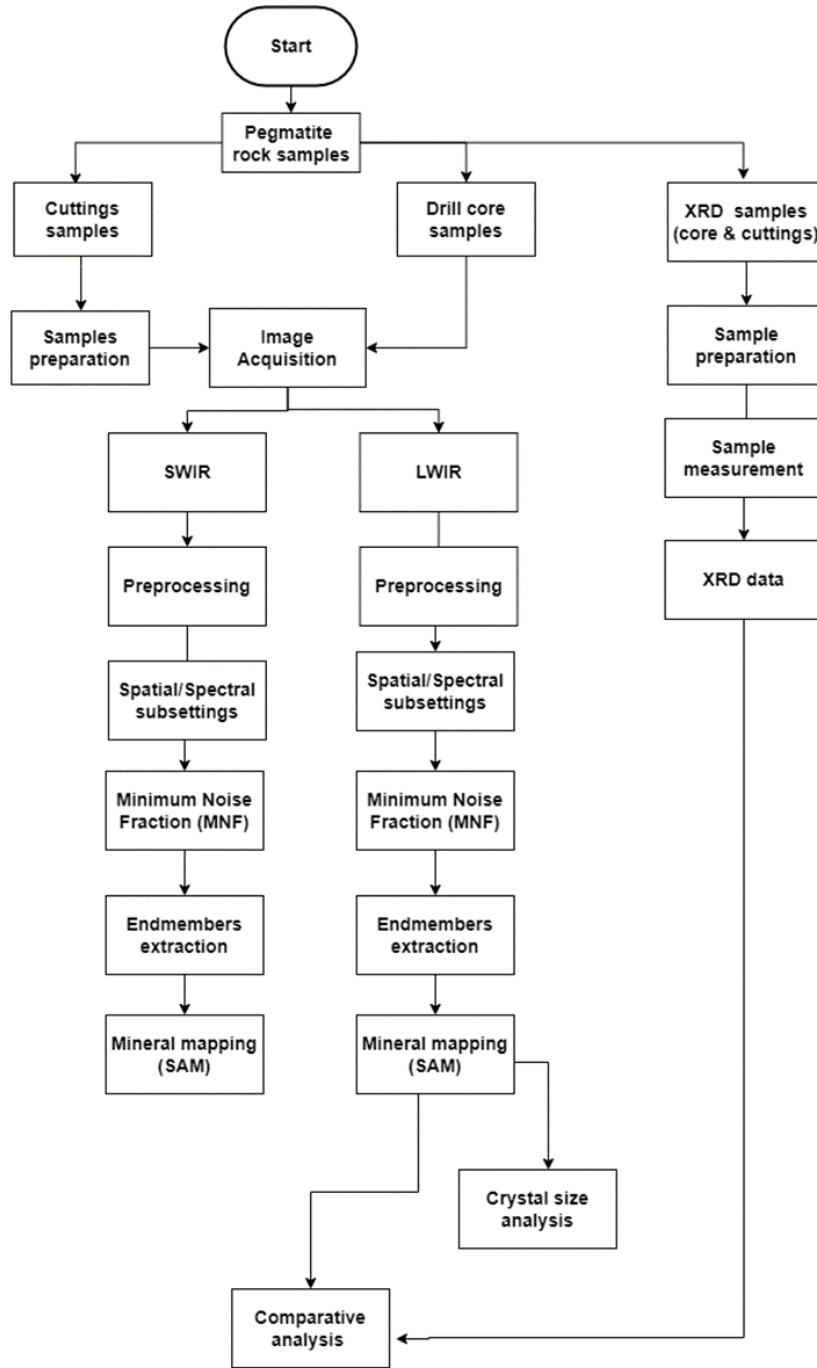


Figure 2.2: Research methodology workflow

2.2.3 Hyperspectral image acquisition (HSI)

Three continuous sawed cores samples with a total length of 4.46 meters and 25 cuttings samples recovered at 1meter depth interval were measured using the specim SisuRock imaging system located at BGR (Bundesanstalt für Geowissenschaften und Rohstoffe) in Hannover, Germany, to acquire VNIR, SWIR, and LWIR hyperspectral reflectance images. The system is equipped with 3 imaging spectrometers cameras covering the wavelength ranges of visible near-infrared (VNIR_ 400-1000 nm in 968 bands), short-wave infrared (SWIR_ 970-2500 nm in 270 bands), and longwave infrared(LWIR_ 7700-12000 nm in 100 bands). The system's spatial resolution depended on the front lenses and was set at 125 μm (VNIR), 320 μm (SWIR), and 400 μm (LWIR). These settings were maintained, except for exposure time, target start, and target stop were adjusted. Exposure time was initially set at 5.0 but adjusted to 4.0 after the first run of scans due to pixel saturation. Adjusting exposure time was essential to get less saturated pixels from the crystal surfaces of the phenocrysts. Target start and stop were required to obtain sample start and end scan positions.

The system is non-destructive and can scan over 100 boxes of core samples within a few minutes (Nikonow et al., 2019). Core sample surfaces without meters marks were laid out according to their depth in the scanline direction and measured sequentially, resulting in a hyperspectral data cube with a coarse spatial resolution and exceptionally high spectral resolution. Due to oversight, a few sample surfaces with meter marks were scanned. However, those samples did not have any issues with further processing and results. The scanning platform was made of an aluminum plate. It includes aluminum trays and movable magnetic balls to keep samples in position. Samples were photographed before scanning to keep track of the original samples. The length of each core sample was measured while on the platform to capture the sample's target start and stop values. Camera settings used for core scanning were maintained for cuttings samples. Cuttings samples were imaged in a circular shallow metal dish painted with black spray paint to minimize background reflectance interference. Each cuttings sample represents a mixture of rock fragments from an approximate depth of one(1) meter. For illustration, core and cuttings samples are shown in figure 2.3. Camera specifications and measurement platform are presented in *appendix 14*.

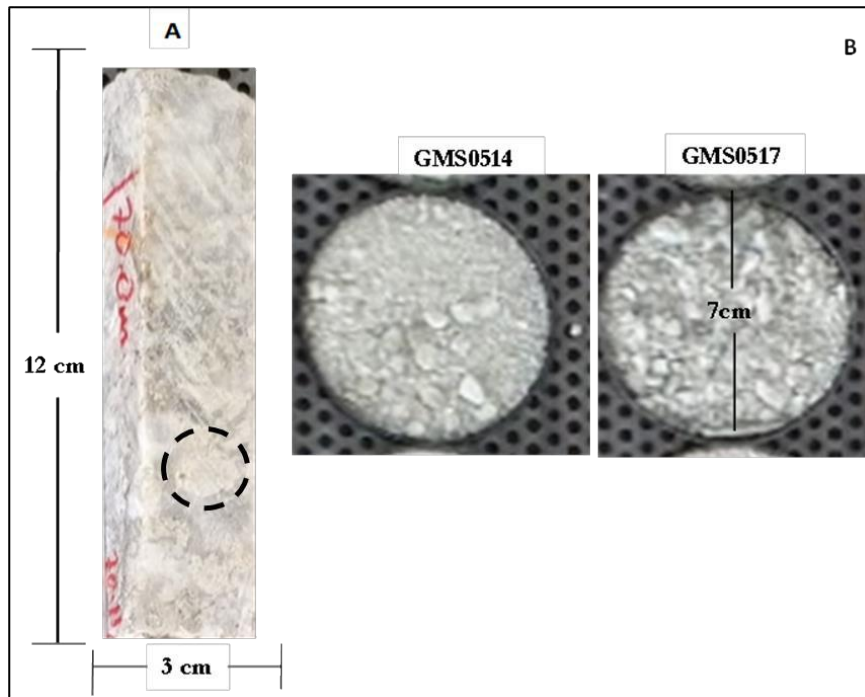


Figure 2.3: A) GMS0509 core sample (depth: 70.0 – 70.10) with 12cm length and 3cm width embedded with intact mineral grains including spodumene crystals (black dotted line). B) Cuttings samples include disaggregated mineral crystals in a black shallow circular dish acquired at 1meter intervals.

2.2.4 Hyperspectral image pre-processing

Hyperspectral core and cuttings datasets were initially preprocessed by Dr. Martin Schodlok (BGR, Germany) using BGR HyProc batch processing chain from Harris, which uses OWL processing chain Version 4.10 due to miscalibration, dropout pixels, and striping resulting in noisy spectral bands. These pre-processing steps include raw data conversion and de-striping. Raw data (DN values) were converted to reflectance values using a diffuse reflecting aluminum standard and dark current measurements on a blackbody. A de-striping method was applied to improve the signal-to-noise ratio of the hyperspectral images for further processing and analysis, i.e., endmember extraction to facilitate mineral mapping. Image spatial and spectral information was preserved during pre-processing while applying noise reduction.

Additional pre-processing of cores and cuttings LWIR datasets involves four steps. First, convert each image data cube (raw DN value) to reflectance images using the manifest file in a dark and white reference calibration tool in HyPpy3 software. Second, spatial and spectral subsetting was performed on both datasets for further noise reduction. Spatial subsetting was executed to remove unwanted margins and artifacts from image acquisition. Spectral subsetting was done to eliminate noisy spectral bands and bands at the peripheral of the required spectral range of LWIR imaging cameras. Before subsetting, core and cuttings images data cube original spectral bands were 288 ranging from band 1 to band 288, corresponding to the wavelength range of 6923 nm to 22206 nm. These subsetting processes delineated both LWIR datasets and subset 82 spectral bands ranging from band 25 to band 106, corresponding to a wavelength range of 8038nm to 12021nm. These processing steps were also applied to core and cuttings SWIR datasets. SWIR image data cube original spectral bands before subsetting were 270 ranging from Band 1 to Band 270, corresponding to the wavelength range 989nm to 2503nm. These subsetting processes delineated SWIR images and subset 268 spectral bands ranging from Band 1 to Band 263, corresponding to a wavelength range of 1000 nm to 2500 nm.

The third step involves minimum noise fraction (MNF) algorithm to reduce spectral dimensions to be analyzed while preserving spectral features (Luo et al., 2016). MNF transformation is similar to principal components but orders the data according to the signal-to-noise ratio, thereby reducing data dimensionality for further processing (Luo et al., 2016). MNF transformation was applied using subsetted cores and cuttings LWIR images as an input file. MNF procedure involves two steps: first, forward MNF transform was performed to estimate noise statistics resulting in output MNF bands and eigenvalue statistics sorted in descending order, allowing users to select the numbers of output MNF components. The statistics were inspected for individual output MNF components and their corresponding eigenvalues. Lower MNF bands contain less noise and high eigenvalues, which contain most mineral information. Higher MNF bands typically contain lower eigenvalues and higher noise percentages resulting in most of the noisy bands in the investigative datasets. Using only bands with higher eigenvalue in subsequent processing separated the noise from the data, thus improving spectral processing results. Examination of the eigenvalue shows that the first 10 MNF components from each cores and cuttings LWIR images contain most of the mineral information, while the rest of the bands progressively contain lower signal to noise ratio. Therefore, based on inspection of MNF bands, an eigenvalue cutoff of 3.5 was applied for all cores and cuttings LWIR images due to images containing different noise levels. Secondly, inverse MNF was performed using the selected 10 MNF components for each core and cuttings LWIR datasets in transforming MNF bands back to their original image space of 82 bands.

MNF processing steps employed for LWIR images were also applied to the core and cuttings SWIR images but with different cutoff eigenvalues. An eigenvalue cutoff of 7.5 was applied to all core and cuttings SWIR images resulting in the first 12 MNF being selected for inverse MNF transformation in transforming the bands back to their original image space of 268 bands. Finally, LWIR and SWIR image data cubes were produced with a minimum noise level compared to the Reflectance (Raw) data cube. In the final pre-processing steps, LWIR reflectance images were converted to emissivity values to avoid highlighting features not representative of minerals in the study datasets.

Therefore, the pre-process reflectance core and cuttings LWIR datasets were converted to apparent emissivity values by applying Kirchhoff's law ($e = 1 - r$), where “e” stand for emissivity, “r” represents the reflectance image(s). The value 1 represents the reflectance scale factor used during data acquisition (in this case, 10000). This equation was used as input variables in the spectral math tool of ENVI 5.6.1 + IDL 8.8.1 image processing software by Harris geospatial. The below equation (i) was used in the conversion process.

$$(10000.0 - b1) \quad \text{equation (i)}$$

b1 – represent an image file

10000.0 - reflectance scale factor

Hyperspectral image pre-processing

The main image processing activities are summaries in Table 2.1

Activities	Purpose
Manual endmember extraction (ROI) and Identification	Generate mean endmembers. Identify endmembers by comparing them with the reference spectral library (USGS) and GMEX spectral interpretation manual.
Mineral mapping_Spectral angle mapper (SAM) classification	To produce a mineral spatial distribution map and determine relative mineral abundances in the study samples. Additionally, to facilitate spodumene crystals measurement.
Spodumene crystal size analysis	To distinguish Coarse-crystal size (P1) and fine-crystal size (P2) intervals based on predefined threshold values.
Mineral quantification comparative analysis (HSI & XRD)	To quantify identified minerals in the study datasets

Table 2.1: Image processing activities and justifications

2.2.5 Endmember extraction and Identification

Endmember extraction is a crucial process used to facilitate mineral mapping. Semi-quantitative endmembers extraction using the region of interest approach was executed based on the color images used to identify specific mineral species and determine their locations on the core. This approach is illustrated in figure 2.4 and demonstrated by displaying Red, Green, and Blue (RGB) MNF components (MNF-4, MNF-3, MNF-2) to enhance mineral crystals to facilitate the digitization of specific regions on the core representing similar pixels. This approach was used to define representative pixels of different color clusters/regions, creating a direct association between end members and image data cube for subsequent processing procedure, i.e., mineral mapping, as indicated by (Hecker et al., 2019; Portela et al., 2021; Kartika P Savitri et al., 2021). An initial 10 ROI were digitized at varying diameters based on different colors, representing 10 distinct endmembers candidates. A mean spectrum was extracted from each distinct material representing different surfaces. Afterward, endmembers with similar shapes and wavelength positions were later averaged to remove duplicates. Finally, five(5) distinct endmembers candidates, including mixed endmembers, were determined from core and cuttings LWIR datasets. A similar approach was applied for the SWIR datasets, resulting in four (4) distinct endmembers candidates.

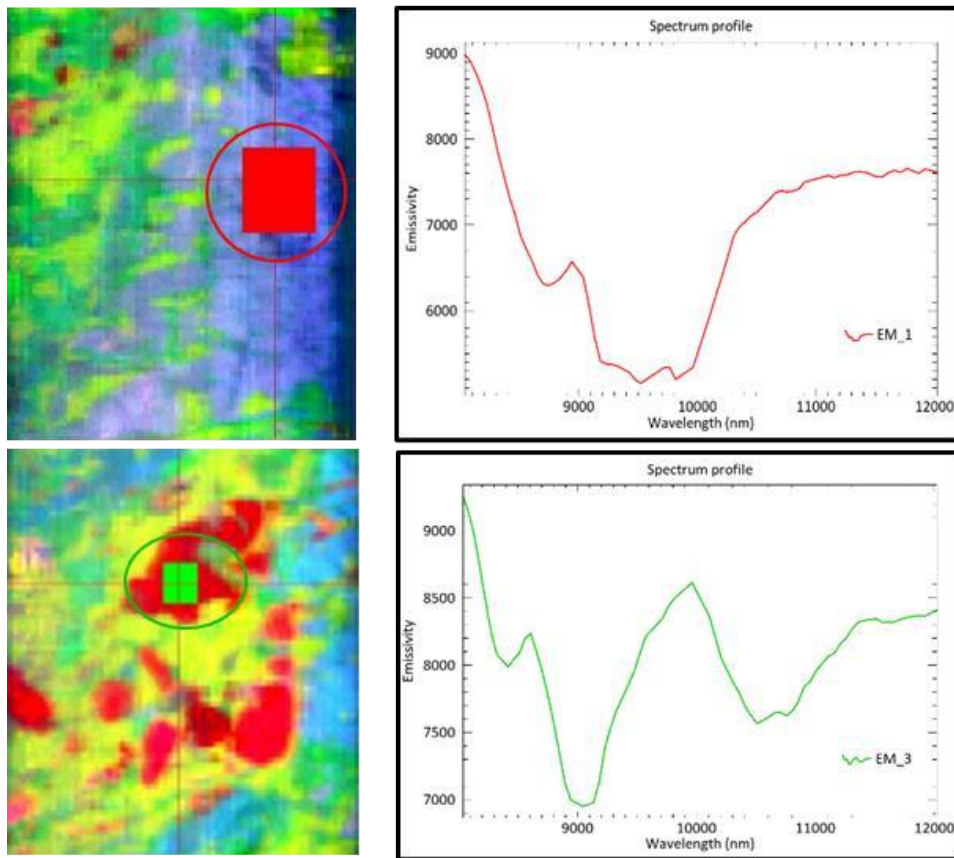


Figure 2.4 shows two examples of the approach used to extract mean endmember spectra from regions of interest based on the color in the RGB-MNF 4,3,2 LWIR image.

Mineral identification is also crucial for hyperspectral mineral mapping. Misidentification of minerals could lead to wrong automatic classification and misinterpretation. Therefore, an accurate mineral database is paramount for good classification results. Minerals that match the five endmembers candidates were determined based on physical inspection of the core in conjunction with digitally extracted spectra. The existing open-source (USGS) spectral libraries comprise 390 minerals of the Nicolet™ Fourier Transform Infra-Red (FTIR) interferometer spectrometers covering the range from 1.12 to 216 μm, and high-resolution next-generation (hi-resNG) models of Analytical Spectral Devices (ASD) field portable spectrometers comprises of 473 minerals covering the range from 0.35 to 2.5 μm were compiled using ENVI 5.6.1 + IDL 8.8.1 image processing software (Clark, 1999; Salisbury et al., 1991). Both libraries were resampled to the study dataset wavelength ranges (8.0 to 12.0 μm and 1.0 to 2.5 μm) and used as an input file in the spectral analyst algorithm in ENVI 5.6.1 + IDL 8.8.1 to minimize endmembers search challenge and compared image endmembers to reference spectral library. Image spectral and reference USGS spectra were normalized for comparison and mineral naming based on spectral characteristics (shape, width, and symmetry) using the equation $((S1 - \text{Min}(S1)) / (\text{Max}(S1) - \text{Min}(S1)))$ as input parameter in the spectral math algorithm in ENVI 5.6.1 + IDL 8.8.1. Visual comparison of the observed image spectra to the resample USGS spectral libraries confirmed the presence of spodumene, quartz, albite, and microcline in the LWIR datasets except for mixed endmembers. ASD library plus G-MEX spectral interpretation field manual also confirms the presence of montmorillonite, muscovite, ammonia smectite, and lepidolite in the SWIR datasets. These mineral endmembers were used as training samples for mineral mapping.

Mineral mapping

Mineral mapping entails training samples (in this case, endmembers assigned to a specific mineral class), resulting in a mineral spatial distribution map and quantification of each mineral abundance percentage. A spectral angle mapper algorithm was employed to map dominant minerals and determine their relative abundances. The below subsection discusses the algorithm in detail.

2.2.6 Spectral Angle Mapper (SAM)

Spectral Angle Mapper (SAM) algorithm was employed to produce classified image maps of core and cuttings LWIR and SWIR datasets showing mineral spatial distribution (Kruse et al., 1993). The algorithm compares radian angles between a reference spectrum and each image spectrum as vectors in feature space (Kruse et al., 1993). A small angle indicates a close match to the reference spectrum. SAM classifier works on the overall subset spectral range displayed by the identified endmembers rather than individual reflectance or emissivity diagnostic features since the classifier cannot be set to only focus on specific diagnostic features of each endmember. The classifier was selected because it is a rapidly famous classification method (Dennison et al., 2004). Each core and cuttings LWIR image was classified using a single spectral library comprised of five mean extracted endmembers associated with the image datasets and a set of threshold values used in the rule post classifier. SAM classification was performed using bands ranging from 1 to 82, corresponding to the wavelength range 8038 nm – 12021 nm. Rule post-classifier was performed on the five LWIR rule images to minimize unclassified pixels and misclassification using a set of threshold values (Table 2.2). These threshold values were determined based on each image histogram and, in some cases, by "trial and error." Classification results were cross-checked by randomly inspecting individual pixel spectrums using RGB-MNF images as reference. Finally, classified mineral maps consisting of five mineral classes were generated. For core and cuttings SWIR datasets, a single spectral library comprised of ten mean extracted endmembers and a single threshold (0.12 radians) was set to produce a spectra match. The resulting mineral classes were combined during post-classification. SAM classification was performed using bands ranging from 193 to 245, corresponding to wavelength range 2105nm – 2402 nm. These spectral ranges were subsetted before applying SAM classification due to minerals overlap. Finally, classified mineral maps consisting of four mineral classes were generated after post-classification.

Mineral	Minimum thresholds value
Mix spodumene	0.05
Quartz	0.55
Microcline	0.09
Albite	0.05
spodumene	0.26

Table 2.2: threshold value for each endmember used in the rule classifier

2.2.7 Spodumene crystal size analysis

Spodumene crystal size characterization plays a crucial role in lithium extraction from spodumene pegmatite during beneficiation and floatation. As a result, a model should be optimized to distinguish coarse and fine spodumene crystal sizes based on either mineralogy, mineral chemistry, textures, or the combination (Menéndez et al., 1303). Several methods and instruments are developed for measuring mineral grain size, including sieving, gravimetric sedimentation, Coulter Counter analysis, laser diffraction, scanning electron microscope, X-ray diffraction, etc. (Cao et al., 2021). Although these techniques effectively provide precise and reliable measurements for a particular range of grain size fractions, they are destructive, time- and material-consuming, and labor-intensive. However, this study employed a manual approach to measure spodumene crystal size from print-out classified LWIR hyperspectral drill core images on a 1:1 scale to the physical core samples. The core samples were used for measuring spodumene crystals size because core crystals are well fixed in positions without disintegration and have better control over sample depth than cuttings samples that are crushed into multiple smaller fragments and flushed to the surface with circulating drilling fluid. Spodumene crystals size analysis was performed by measuring the three largest spodumene crystals size within every 10 cm intervals from print-out LWIR core images. A standard 30 centimeters ruler was applied to measure crystal long and short axis used to calculate crystal area **[short axis(d1)* long axis(d2)]**, as shown in figure 2.5. Crystals area were recalculated using the formula **[A = pi * d1/2 * d2/2]**, considering ellipses as approximate crystals shape. A total of 132 crystals (long and short axes) were manually measured from ~4m continuous LWIR core samples. Forty-two representative spodumene crystals were measured from the core section labeled as sample GMS0507, fifty-seven from GMS0508, and Thirty-three from GMS0509. Coarse spodumene crystal (P1) and fine spodumene crystal (P2) were distinguished based on a predefined threshold value. If the mean of the three largest spodumene crystals size in a 10 cm interval was larger than a threshold value $\geq 100 \text{ mm}^2$, the interval was described as a coarse spodumene crystal interval; otherwise, the interval was deemed fine-crystal.

This threshold value is somewhat subjective but was based on an inspection of the whole cored ~4 m interval and was judged to capture the crystals variability of the section drill hole. Note that this crystal criterion is different from that used by the geologists of Atlantic Lithium, who classify the crystal sizes of pegmatite intervals based on an estimation of the mean grain size, with intervals having a mean spodumene grain size $\geq 20 \text{ mm}$ as ‘coarse grained’ or ‘P1’, and $\leq 20 \text{ mm}$ as ‘fine-grained.’

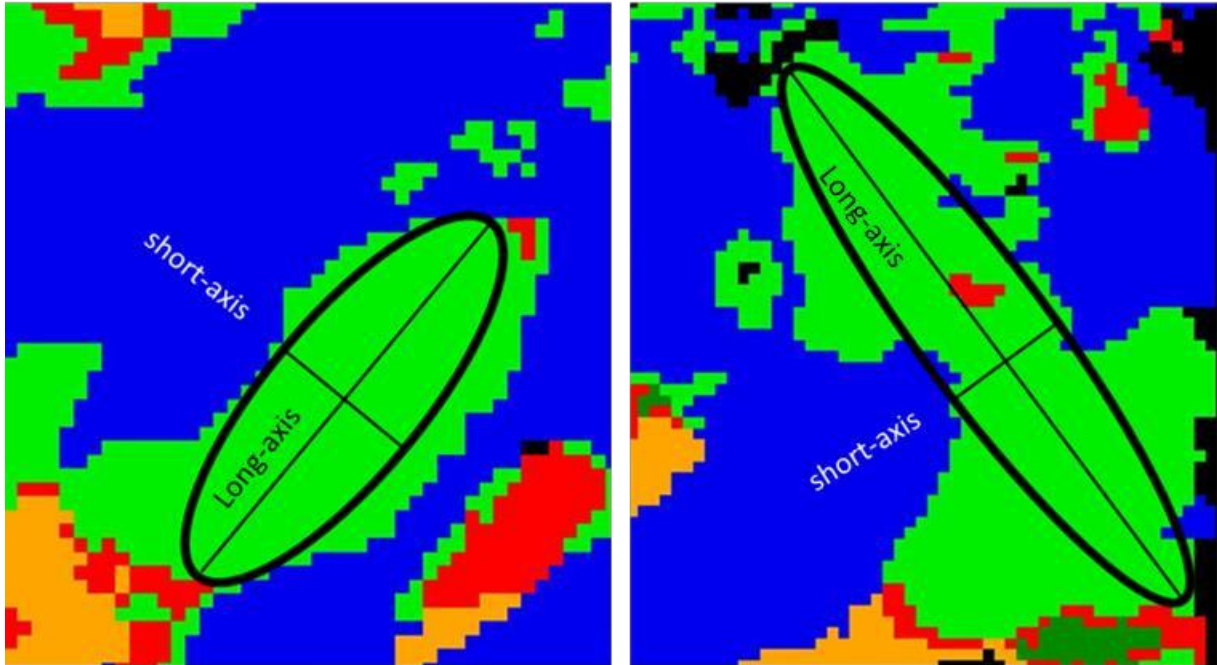


Figure 2.5 shows two examples of the approach used to manually measure spodumene crystal size (long & short axis) directions from printed-out LWIR classified images

2.2.8 LWIR-XRD Comparative Analysis

SAM-LWIR cuttings mineralogy (sieved and washed) and XRD whole-rock cuttings (unsieved and unwashed but milled) mineral abundances on all 100cm samples were compared to assess the performance of LWIR spectroscopy in mapping spodumene and other associated minerals. Before performing comparative analysis, a database comprised of 25 cuttings samples was compiled for both HSI and XRD. Similar minerals observed from both datasets were used in the analysis. These minerals include spodumene, quartz, albite, and microcline. SAM-LWIR database was recalculated to exclude unclassified pixels and distribute mixed mineral abundance percentages across each constituent mineral. This was done by subtracting the total unclassified pixels from the total pixels of each 100cm LWIR core sample to obtain the total classified pixels used in calculating mineral abundance estimates for spodumene, quartz, albite, and microcline. Based on visual inspection of the mixed spectrum shape and wavelength position, an assumption was made to identify spodumene as the strongest feature in the mixture based on its wavelength position at 9038nm. Mineral mixture abundances were distributed across each constituent mineral in the mixture, with 50% allocated to spodumene, quartz 20%, albite 15%, and microcline 15%.

The relative value was added to the pure mineral estimate to produce each mineral's relative abundance used for the comparative analysis. For example, samples GMS0509 contained 15% pixels of spodumene and 1.5% mixed pixels; 50% was allocated to spodumene, amounting to 0.75, which was added to the pure spodumene percentage (Total 15.75%). The calculation continues for the rest of the minerals in all samples. Quantitative comparative analysis was done using a linear correlation coefficient approach. A method that compared two-variable strengths to understand and assess their statistical relationship. R-squared is a goodness of fit measure for regression models. It also tells us how well the regression model explains the observed data. Correlation coefficient was calculated between two variables based on a trendline (regression line) and sample distribution of each mineral abundance from both datasets. Therefore, LWIR and XRD cuttings mineral abundances were compared and assessed based on the method employed.

In addition, SAM-LWIR mineralogy on all 100cm core samples and SAM-LWIR mineralogy on 100cm cuttings at exactly the same depth intervals were correlated to established mineralogical relationships in distinguishing **'P1'** and **'P2'**. Finally, drill core modal mineralogy for quartz, spodumene, albite, and microcline on ~4 m continuous core samples were correlated with spodumene crystals size data to establish a quantitative relationship associated with both datasets. The data employed were recalculated due to unrealistic percentage values for the unclassified pixels, thus reducing the percentages of other minerals. The database was recalculated using the above mention procedures. In addition to the correlation analysis, a graphical representation of SAM-LWIR and XRD mineral abundance was plotted against relative depth to understand mineralogy trends with both datasets.

3. RESULTS

This chapter presents all results of the pre-process and process methodologies, including spectral subsetting, minimum noise fraction, endmember extraction and identification, mineral mapping (spectral angle mapper), spodumene crystal size, and comparative mineral analysis. Throughout this section, specific samples were selected for illustration.

3.1 Image pre-processing

3.1.1 Spectral subset

Spectral subsetting was executed to initially reduce noise and maintain the targeted wavelength range to enhance mineral spectral features essential for the study. Before subsetting core and cuttings, LWIR and SWIR datasets original wavelength range goes from 6923nm to 22206 nm for LWIR and 989 nm to 2503 nm for SWIR. Figure 3.1A displayed a mean spectrum from a region of interest (ROI) before spectral subset. The spectrum shows negative reflectance values and multiple spikes indicating noisy bands ranging from 6923nm to 8000 nm and 12500 nm to 22000 nm, respectively. After spectral subsetting, the wavelength range goes from 8000 nm to 12000 nm for LWIR and 1000 nm to 2500 for SWIR. Figure 3.1B displays a mean enhanced spectrum from the same ROI after spectral subsetting showing minimum spikes.

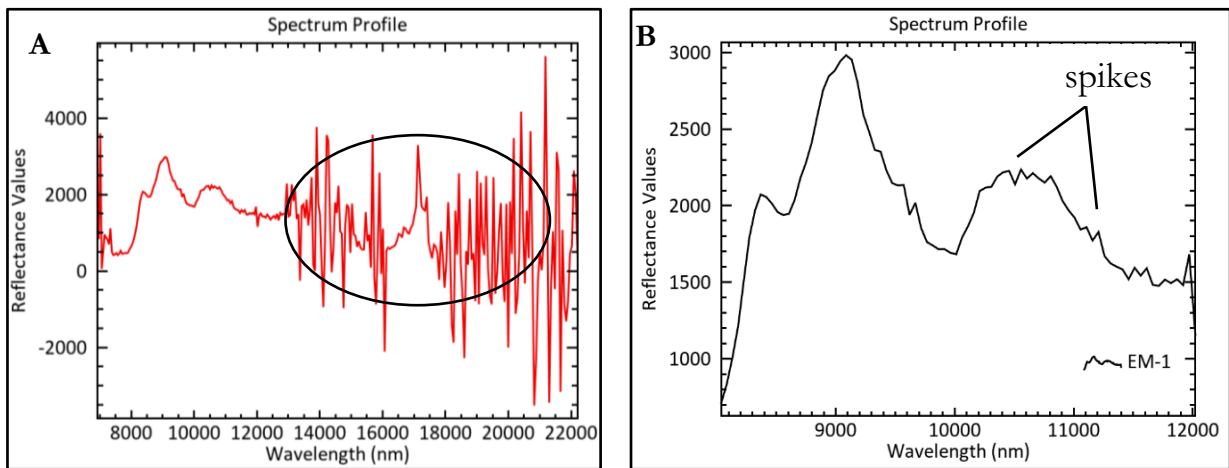


Figure 3.1: A) Reflectance spectrum from ROI before spectral subsetting indicating high noise levels(indicated by a black circle). B) Reflectance spectrum after spectral subsetting showing enhanced mineral spectral feature with little spikes (noise).

3.1.2 Minimum Noise Fraction (MNF)

Output MNF bands and eigenvalue statistics of the preprocess hyperspectral core and cuttings LWIR images after forward MNF transformation are displayed below. Figure 3.2A and B show an example of a sample image from 3 cores and 25 cuttings LWIR images. Core sample (GMS0507) and cuttings sample (GMS0536) illustrates varying level of signal (mineral information) and noise per component. Figure 3.3 illustrate an eigenvalue plot for LWIR core image. The plots fall sharply and flatten out, separating signal from noise level. Eigenvalue increase corresponds to a decrease in noise level as displayed by the first 10 MNF bands for both core and cuttings LWIR datasets. A decrease in eigenvalues corresponds to an increase in noise level indicated by MNF bands ranging from 11 to 82 for core and 11 to 70 for cuttings datasets. Minimum changes were observed below the cutoff point displaying degrading image quality corresponding to their low eigenvalues. These components were not included in the inverse MNF transformation. The procedures were also repeated for core and cuttings SWIR datasets. Results show that the first 12 output MNF bands contained signals corresponding to their high eigenvalues. Band 13 to band 14 show break-in signal-to-noise level followed by a continuous trend of noisy bands ranging from 15 to 217 and a continuous signal trend from band 218 to band 260. Based on the results, the first 12 MNF components were selected for inverse MNF transformation.

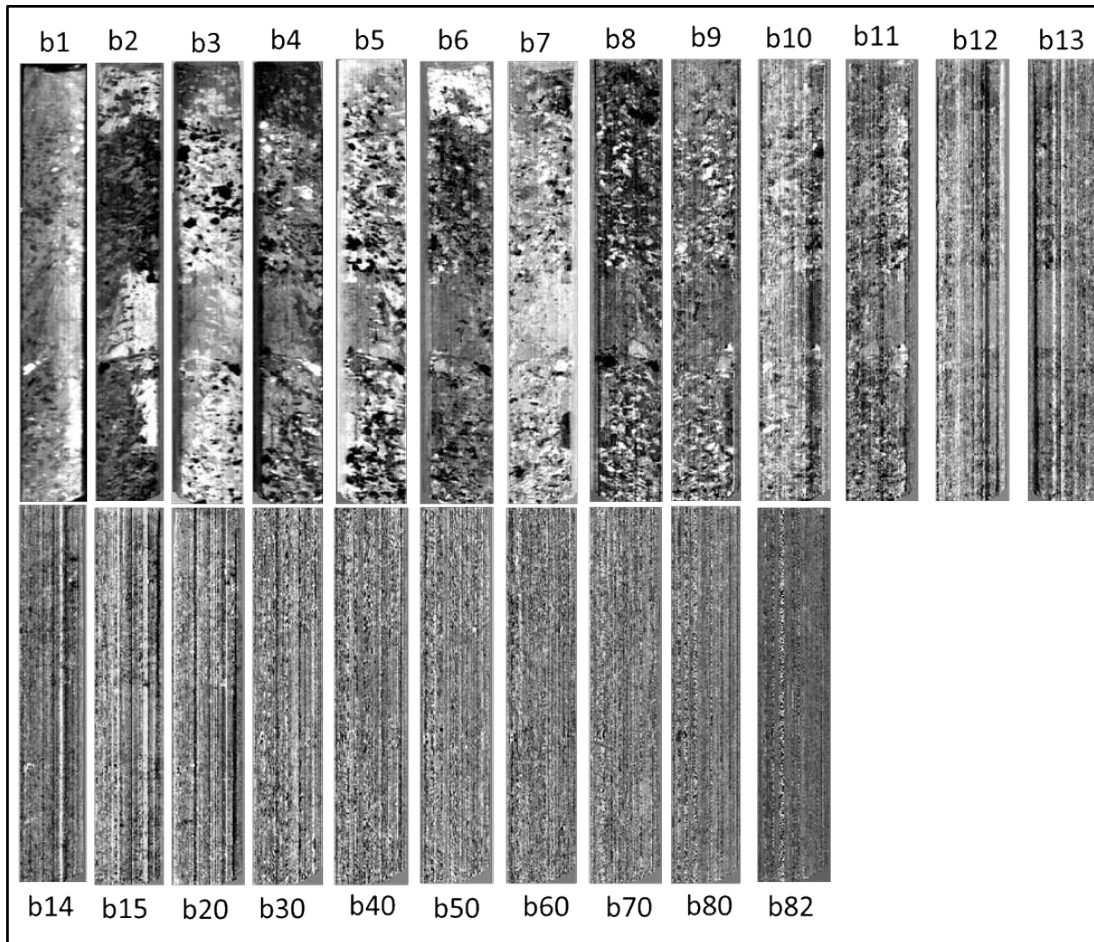


Figure 3.2A: Minimum Noise Fraction (MNF) output bands of drill core sample(GMS0507_depth 66.88 – 67.37m) ranging from band 1 to band 82. The first 10 output MNF bands show enhanced mineral features and less noise. Bands 11 to 82 showed poor image quality, and less mineral information was excluded for further processing.

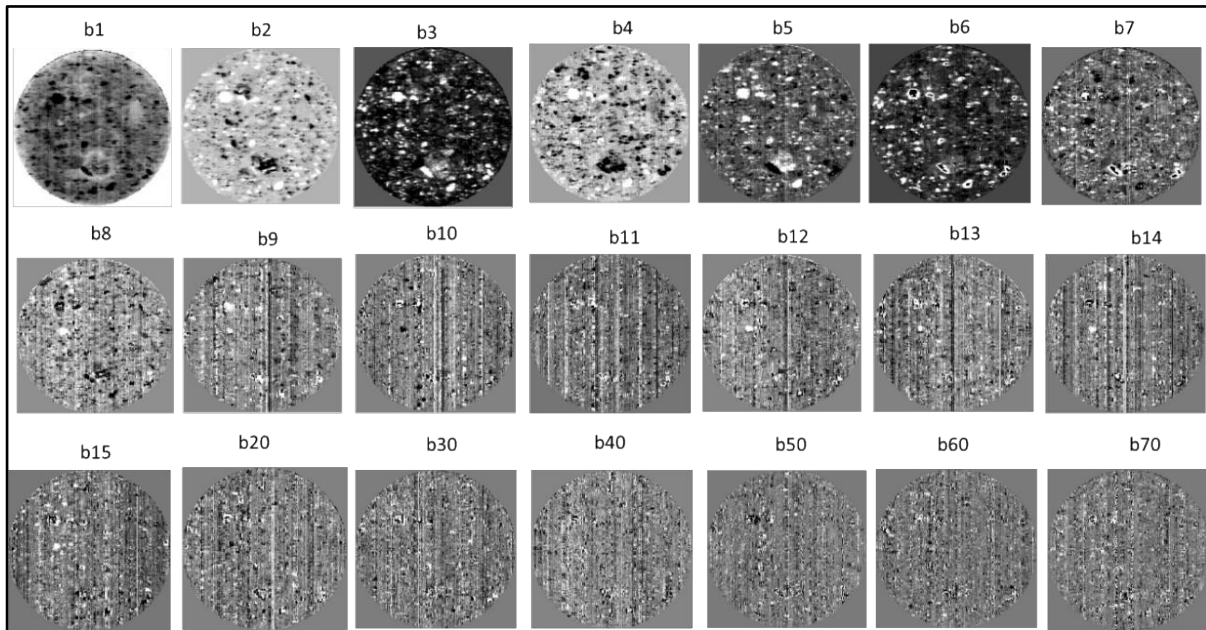


Figure 3.2B: Minimum Noise Fraction (MNF) output bands of cuttings sample (GMS0536_depth 79.0 – 80.0m) ranging from band 1 to band 70. The first 10 output MNF bands show enhanced mineral features and less noise. Bands 11 to 70 showed poor image quality, and less mineral information was excluded for further processing.

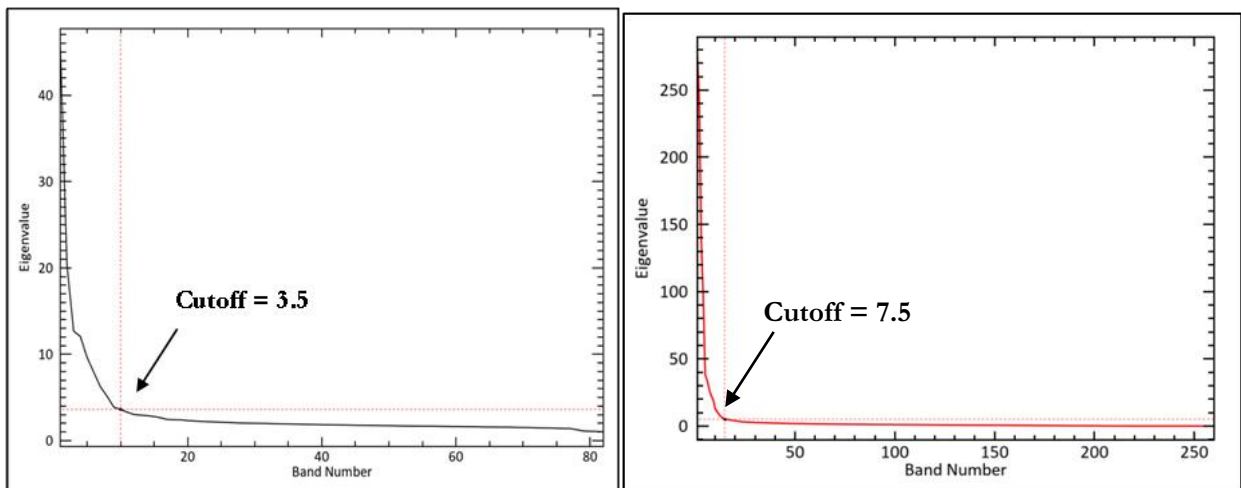


Figure 3.3 Left: Eigenvalue plot of LWIR sample_GMS0507, right: Eigenvalue plot of SWIR sample_GMS0507

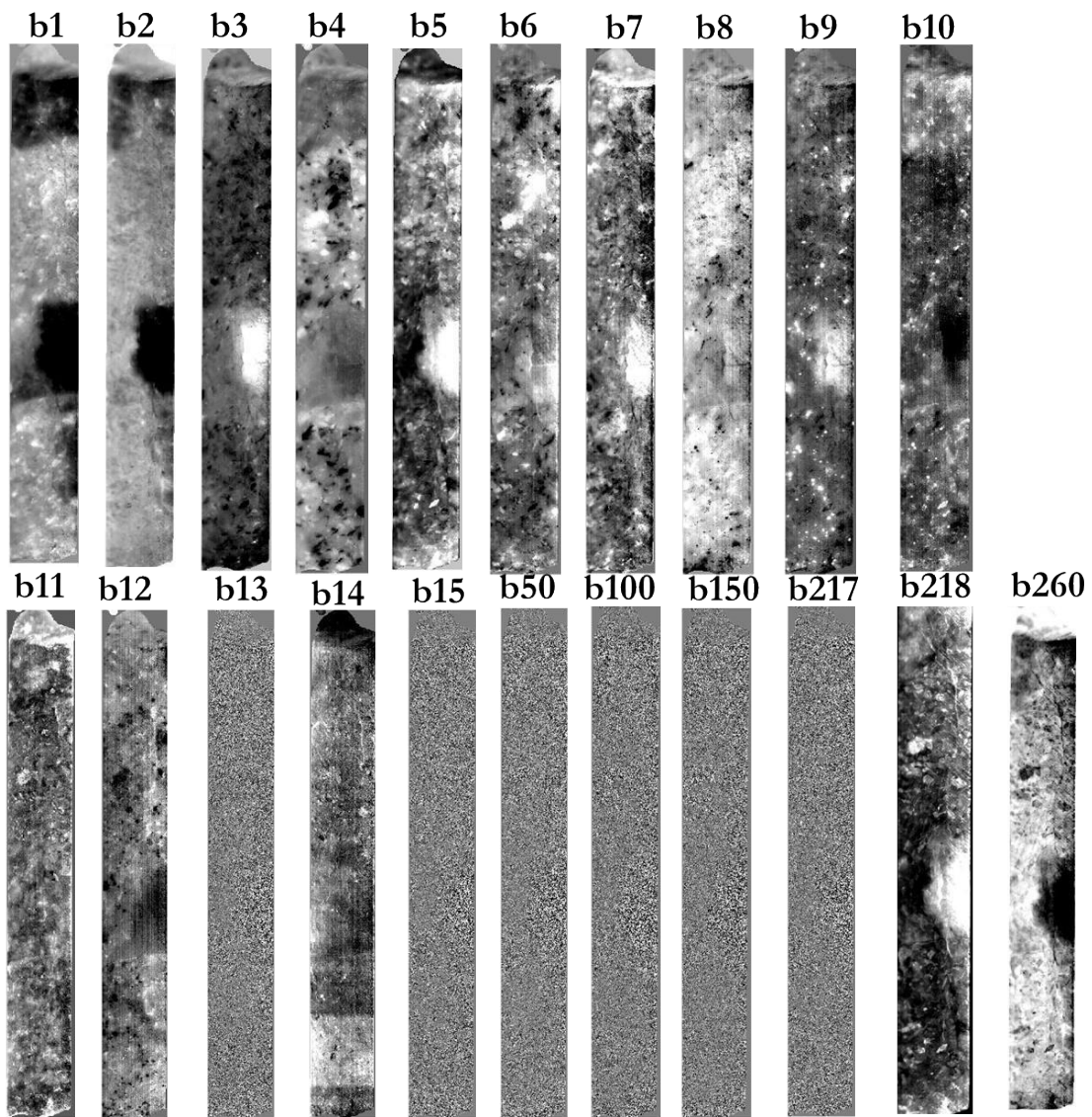


Figure 3.4: Minimum Noise Fraction (MNF) output bands of drill core sample(SWIR_GMS050_depth 66.88 – 67.37m) ranging from band 1 to band 260. The first 12 output MNF bands show enhanced mineral features and less noise. Bands 13 and 14 show break-in SNR, while bands 15 to 217 show poor image quality, followed by bands with continuous signals from 218-260.

Finally, noises were suppressed after applying the forward and inverse MNF transformation. Noise suppression is demonstrated in the reflectance spectrum, as shown in Figures 3.5 A and B. The original reflectance spectrum (solid black line) in Figures 3.5A and B shows multiple spikes indicating false positive mineral emissivity and absorption features. These were eliminated, as shown in the resulting reflectance spectrum (black dotted line) extracted from the same pixel. Emissivity spectrum generated after reflectance to emissivity conversion is illustrated in Figure 3.5C.

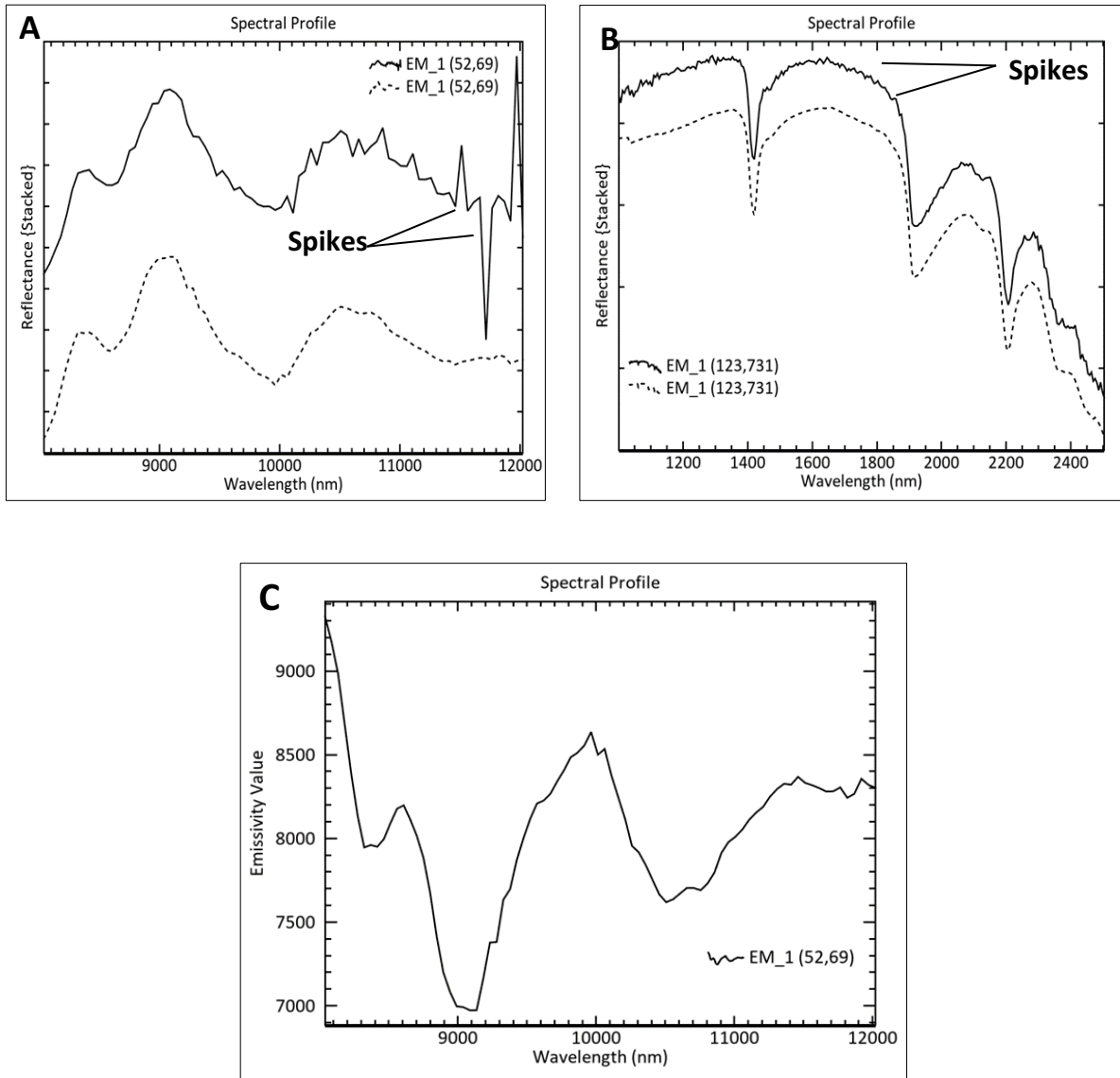


Figure 3.5: A) Reflectance spectra of a single pixel from LWIR datasets and B) Reflectance spectra from SWIR datasets before MNF (solid black line) showing multiple spikes and after MNF (black dotted line) showing noise reduction effect. C) Emissivity spectrum resulted after reflectance to emissivity conversion.

3.2 Endmember extraction and identification

Imaging spectroscopy investigation identified five unique endmembers from core and cuttings LWIR images, including an endmember mixture and four endmembers from core and cutting SWIR images. The mixed spectrum was included in the classification process to determine mineral abundances and observed to be a combination of spodumene-quartz and spodumene-albite-microcline extracted from LWIR datasets. These mixtures were identified around 8300 nm and 9600 nm. LWIR endmembers spectral signature shows significant differences in shape and wavelength position of their emissivity minima and emissivity peak, while SWIR endmembers spectral signature also differs in their shapes but significantly overlaps in the wavelength positions of their deepest features. LWIR and SWIR images distinct spectral features are shown within the reshtstrahlen bands (8000 nm to 11500 nm) and absorption bands (1000 nm to 2500 nm), respectively. Visual comparison of the observed spectrum to the reference spectrum confirmed the presence of quartz, microcline, albite, and spodumene from LWIR dataset and montmorillonite, ammonia smectite, lepidolite, and Muscovite from SWIR dataset, as shown in figure 3.6A-E and figure 3.7A-C. Continuum removal by division was applied to all spectra.

3.2.1 LWIR identified minerals

Spodumene exhibit three emissivity peaks at 8512 nm, 9963 nm, and 1146 nm, and multiple emissivity minima at 8322 nm, 9086 nm, and 10506 nm. These features are due to the OH stretching bond, distinguishing spodumene from other silicate and lithium-bearing minerals. Spodumene features were observed to be overlapping with other minerals like quartz, albite, and microcline. This could be attributed to spodumene broad features covering the full LWIR wavelength range. Spodumene and quartz overlap around 8322nm and 9086nm, while albite and microcline at 9183 nm. Multiple features observed were pronounced in the USGS spectrum but displayed a slight shift in their wavelength positions around 10400nm. This may be attributed to different instruments and sample types.

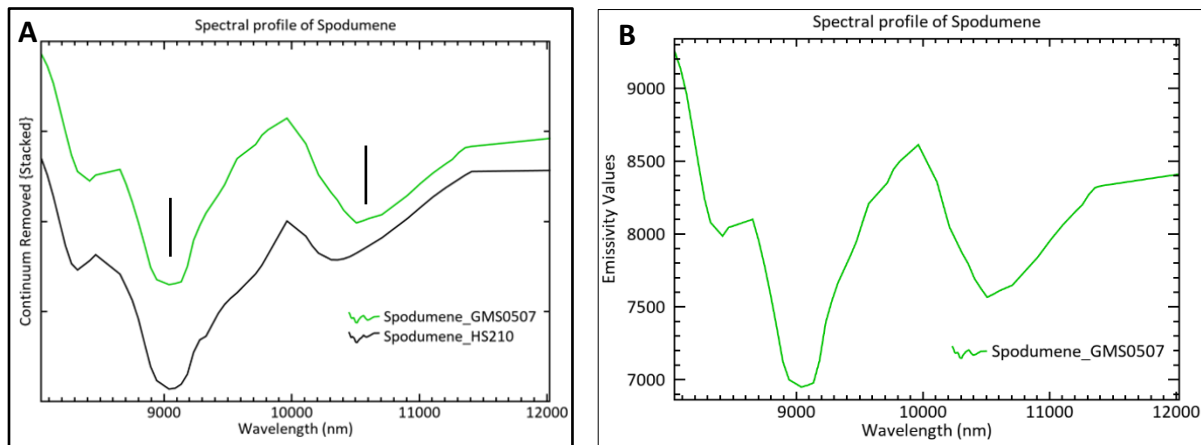


Figure 3.6A: A) Continuum removed emissivity spectrum of spodumene (green) displayed together with the equivalent spectral library resampled of the USGS_GDS74 (black). Note: the black vertical line indicates emissivity minima for clarity. B) Normal emissivity spectrum of spodumene from drill core GMS0507.

Quartz spectrum includes prominent reststrahlen doublet, one at a shorter wavelength around 8274 nm and another at a longer wavelength around 9135 nm. These were observed in the study dataset due to its fundamental stretching vibration of silicates. In between the doublet is a sharp trough feature at 8607 nm. The strongest reststrahlen bands of quartz produce a relatively simple W-shaped signature in its emissivity spectrum and M-shape in its reflectance spectrum. The USGS spectrum also confirmed these distinct features, as shown in figure 3.6B.

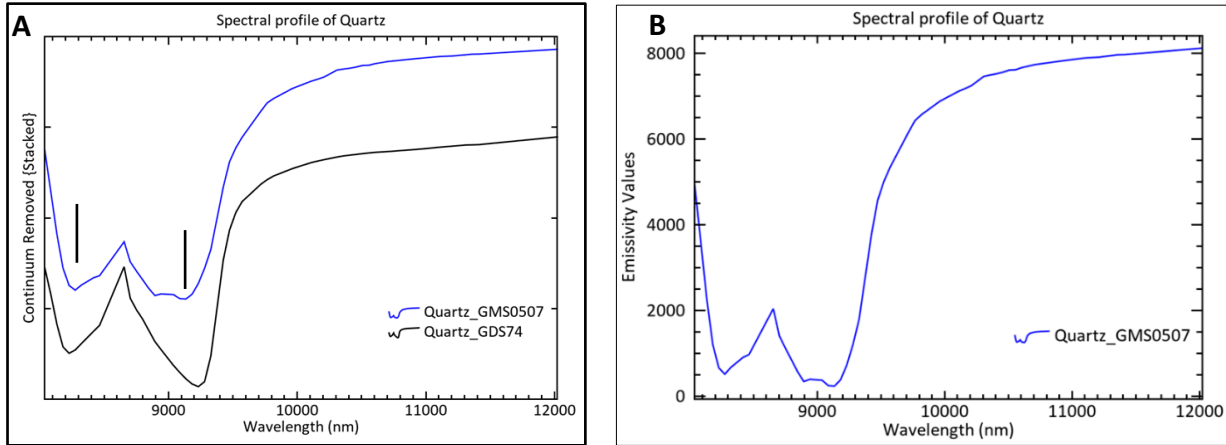


Figure 3.6B: A) Continuum removed emissivity spectrum of quartz(blue) displayed together with the equivalent spectral library resampled of the USGS_GDS74 (black). Note: the black vertical line indicates emissivity minima for clarity. B) Normal emissivity spectrum of quartz from a core sample(GMS0507)

Microcline spectrum display four prominent reststrahlen features. The first pronounced broad feature center around 8702 nm and a weak triplet feature around 9135 nm, 9474 nm, and 9815 nm, respectively. These features are due to the fundamental stretching vibration of silicates. A corresponding USGS microcline spectrum validates microcline features observed in the image data (figure 3.3).

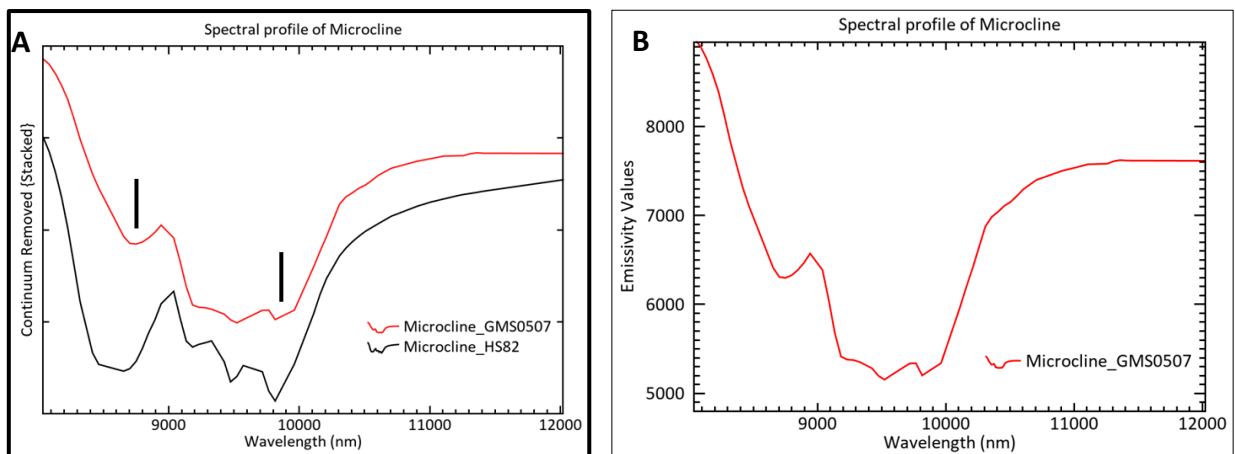


Figure 3.6D: A) Continuum removed emissivity spectrum of microcline(red) displayed together with the equivalent spectral library resampled of the USGS_GDS74 (black). Note: the black vertical line indicates emissivity minima for clarity. B) Normal emissivity spectrum of microcline from drill core GMS0507.

Albite exhibit four distinct spectral features. First, a broad feature at 8702 nm, followed by a subtle feature at 9183 nm and two doublet features at 9571 nm and 9963 nm. These emissivity minima relate to multiple emissivity peaks at 9038 nm, 9280 nm, 9767 nm, and 10308 nm, respectively. These features distinctively distinguish albite from microcline. However, the distinction is minimal and can be seen in the shift of their wavelength position, thus creating difficulties in distinguishing albite from microcline. Multiple features observed were pronounced in the USGS spectrum but displayed a slight shift in their wavelength positions.

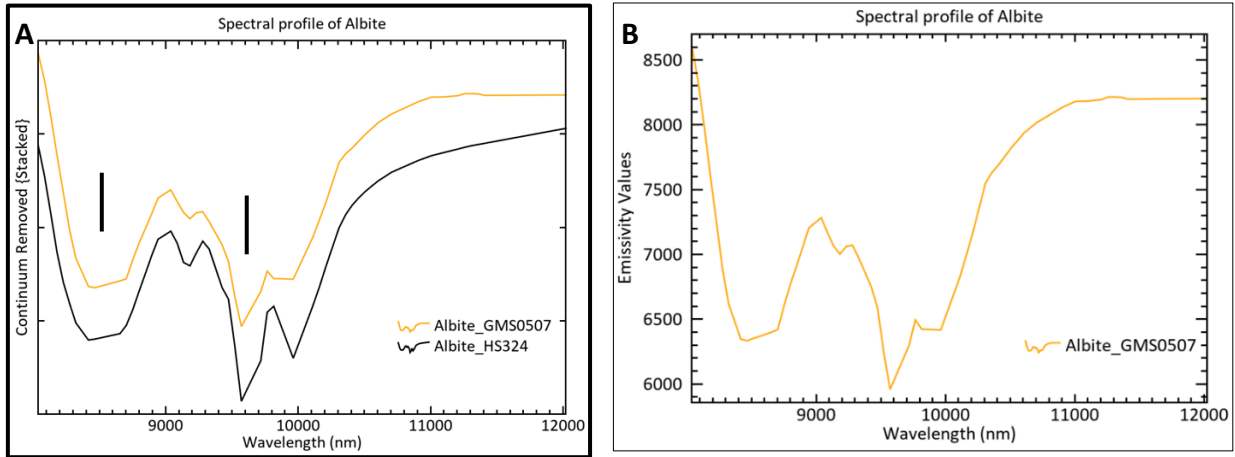


Figure 3.6C: A) Continuum removed emissivity spectrum of Albite(yellow) displayed together with the equivalent spectral library resampled of the USGS_GDS74 (black). Note: the black vertical line indicates emissivity minima for clarity. B) Normal emissivity spectrum of albite from drill core GMS0507.

Spectral mixture identified in this study includes spodumene-quartz and spodumene-albite-microcline mixture. Spectral mixture of spodumene-quartz was observed at 8417 nm, while spodumene-albite-microcline was observed at 9571 nm and 9815 nm. Visual inspection of the so-called mixed spectral (shape and wavelength position) identified spodumene as the strongest feature in the mixture based on its deepest emissivity minima at 9038 nm. Spodumene's second and third emissivity features at the wavelength positions 8417 nm and 9571 and 9815 nm were significantly distorted. Due to spodumene being the strongest feature in the mixture, an assumption was made to allocate 50% of mixture abundance to spodumene, with the rest distributed across quartz, albite, and microcline. Distortion and shift in spodumene spectrum as the result of the mixture were observed in all samples, as shown in figure 3.6E.

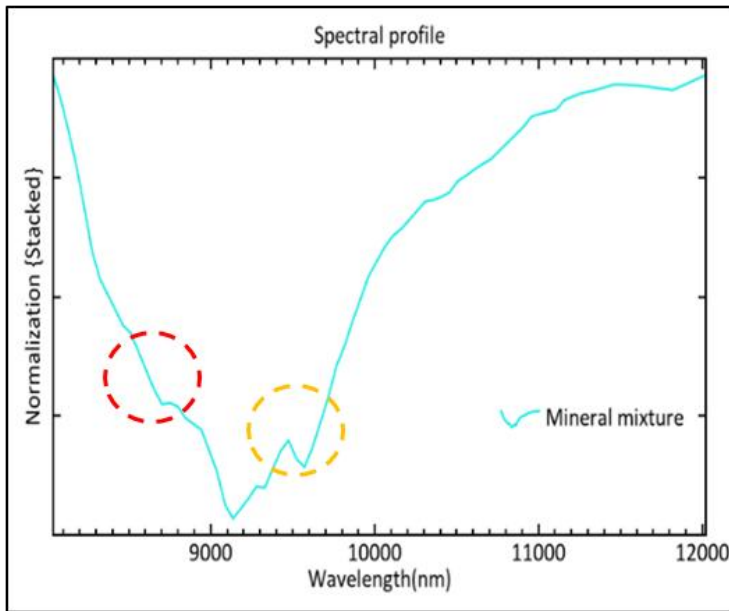


Figure 3.6E: the so-called mixed spectrum of spodumene-quartz-albite-microcline (cyan) from core images. Note: the feature (in red circle) was observed to be associated with quartz-spodumene mixture, while the feature (in yellow circle) was determined to be associated with albite and microcline. These features were observed in all samples of the study datasets.

3.2.2 SWIR identified minerals endmembers

Lepidolite can be characterized by an intense feature around 1420 nm due to an overtone of the OH stretching fundamental, which can be used to distinguish the mineral from muscovite. A broad, shallow feature at 1920nm indicates that a small amount of water is present (Clark, 1999; 1990). The bands near 2206nm, 2357nm, and 2469nm are due to combination bands involving OH stretch and possibly Al-OH- bending mode, which overlapped with muscovite, making distinguishing both minerals challenging. Due to OH combination modes, lepidolite also contains weak bands at 1256nm and 1329nm.

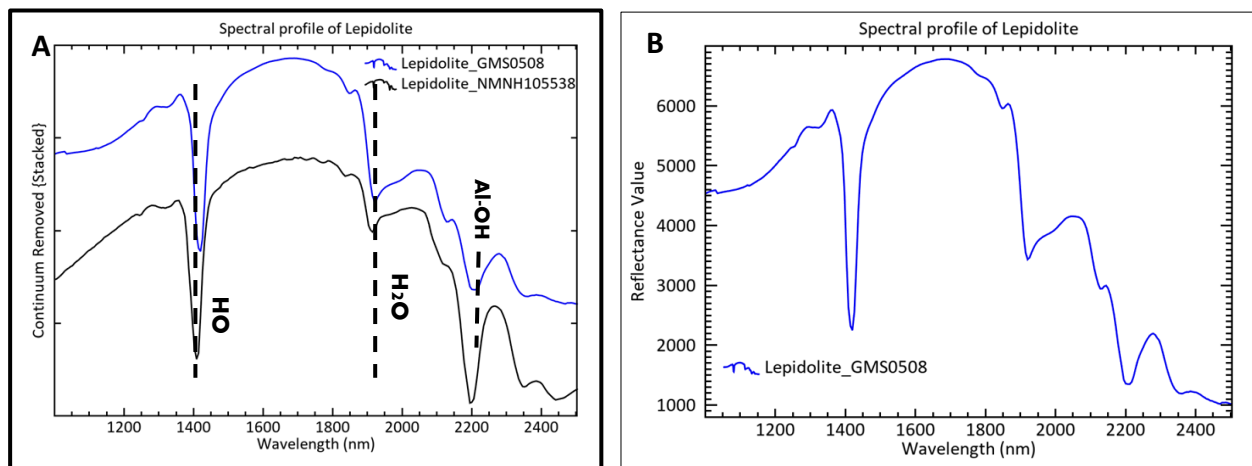


Figure 3.7A: Spectral profiles: A) continuum removed lepidolite (red) spectra from core image and USGS_NMNH105538(black). Note: the black vertical dash line indicates spectral absorption features which can be used to identify lepidolite. B) Normal reflectance spectrum of lepidolite from drill core GMS0507.

Muscovite is characterized by features that appear in two well-defined spectral regions originating from OH Vibrations. A narrow feature registered around 1420nm in the OH stretching region and a weak and broad feature around 1920nm originates from H₂O stretching vibrations. The Al-OH stretch region registered 2357nm and 2469nm, respectively. These features coincide with the reference spectra of the USGS library and GMEX spectral interpretation booklet.

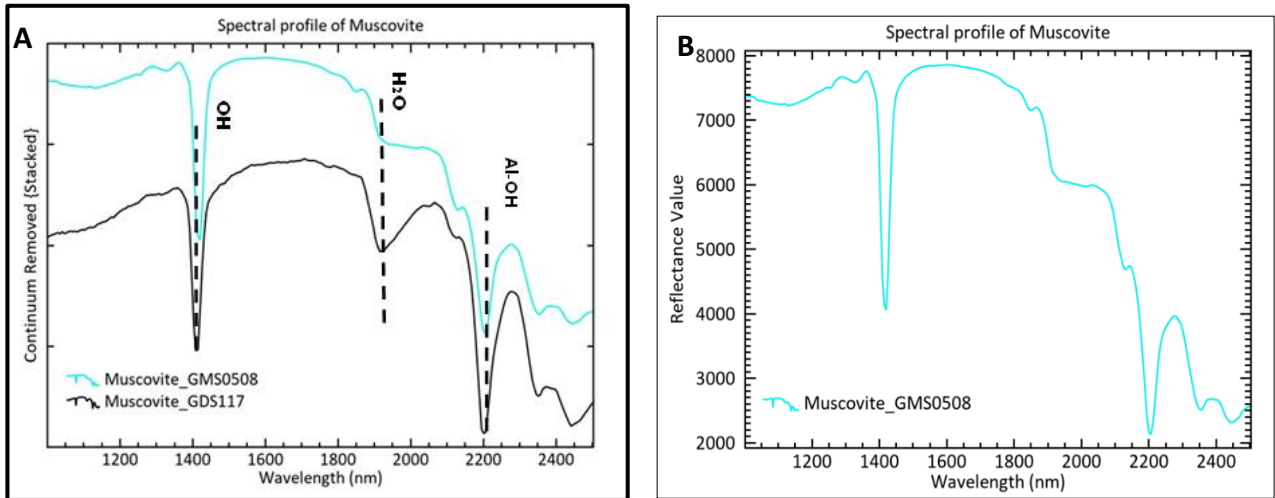


Figure 3.7B: Spectral profiles: A) continuum removed muscovite (green) spectra from core image and USGS_GDS117(black). Note: the black vertical dash line indicates spectral absorption features, which can be used to identify muscovite. B) Normal reflectance spectrum of muscovite from drill core GMS0507

Smectite group

Montmorillonite and ammonio smectite spectra were identified by one narrow feature around the OH and H₂O stretching region at 1420 nm and 1942 nm, associated with three shoulders at 1358 nm and 1662 and 2082 nm, respectively. The broad feature at 1942 nm is presumably due to water in the montmorillonite structure. The feature at 1420nm arises from hydroxyl stretching vibrations. A prominent feature was observed at 2206 due to the Al-OH bond.

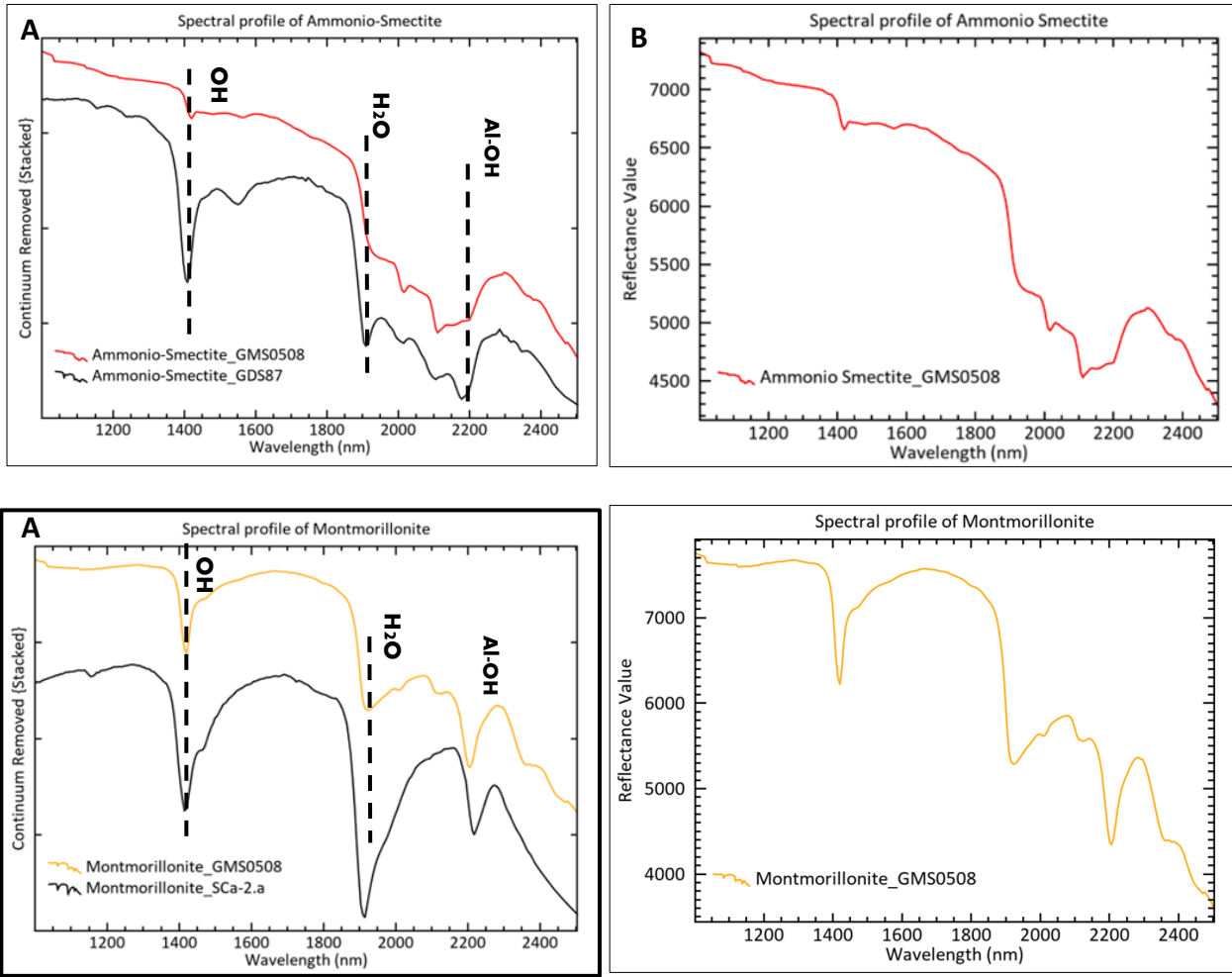


Figure 3.7C: Spectral profiles: A) continuum removed ammonio-smectite (yellow) and montmorillonite(blue) Muscovite (green) spectra from core image and reference spodumene from USGS_Sca-2a. Note: the black vertical dash line indicates spectral absorption features, which can be used to identify the minerals. B) Normal reflectance spectrum of montmorillonite and ammonio smectite from drill core GMS0507

3.3 Mineral Mapping

3.3.1 Spectral Angle Mapper (SAM)

LWIR and SWIR images were used as input files in the SAM classifier to generate mineral classification images based on the dominant mineral species in each pixel. Each pixel represents one mineral species or a mixture. Five mineral endmembers, including spodumene, quartz, albite, microcline, and a mixed mineral spectrum from LWIR core and cuttings dataset, were used as training samples to generate classified LWIR image maps. Similarly, four mineral endmembers, including Muscovite, lepidolite, montmorillonite, and ammonia-illite-smectite from SWIR core and cuttings datasets, were used as training samples to generate classified SWIR image maps. SAM classification resulting from 3 core and 25 cuttings samples shows that not all pixels were classified. However, more than 50% of pixels were classified as presented below in figures 3.8, 3.9, and 3.10. Six(6) short 10 cm core samples sections (one per original 100 cm sample bag number labeled as GMS0507, GMS0508, GMS0509) and 25 cuttings samples of both LWIR and SWIR are presented for illustration purposes: GMS0507 (65.9-66.0 m), GMS0508 (68.4-68.5 m), GMS0509 (70-70.11 m). Cuttings samples GMS0512 (55 – 56 m) to GMS0521(64 – 65 m). The total LWIR and SWIR core sample depths and cutting images are displayed in appendices 1 to 8. According to SAM results, the composition of these samples are as follows:

LWIR Core data:

GMS0507 (depth: 65.9 – 67.37m): spodumene(4.62 %), quartz (26.63 %), microcline (4.75 %), Albite (5.45 %) and mixture(0.35 %), and unclassified pixels (58.18 %)

GMS0508 (depth: 67.37 – 69.2m): spodumene(13.13 %), quartz (32.05%), microcline (10.56%), Albite (12.81%) and mixture(1.73 %), unclassified (29.69 %)

GMS0509 (depth: 69.2 – 70.34m): spodumene(14.36 %), quartz (38.43 %), microcline (5.16 %), Albite (10.96 %) and mixture(0.92 %), unclassified (30.13 %)

Cuttings samples: Percentage estimate of minerals identified from 25 cuttings samples are displayed in table 3.3

Cuttings samples_Mineral abundance %								
sample #	depth_from(m)	depth_To (m)	spodumene	Quartz	microcline	Albite	mixture	unclassified
GMS0512	55	56	14.20	11.66	31.37	3.99	0.54	38.24
GMS0513	56	57	12.87	16.82	30.31	2.68	0.62	36.71
GMS0514	57	58	27.70	15.69	16.19	0.45	0.29	39.68
GMS0515	58	59	21.83	12.28	25.93	0.98	0.42	38.56
GMS0516	59	60	32.23	9.84	18.90	0.29	0.16	38.57
GMS0517	60	61	10.18	21.00	9.68	0.40	0.17	58.57
GMS0518	61	62	16.74	12.53	22.45	1.39	0.10	46.80
GMS0519	62	63	22.46	14.97	18.05	1.49	0.17	42.85
GMS0520	63	64	15.66	11.85	28.36	1.18	0.12	42.84
GMS0521	64	65	18.37	23.40	16.79	1.83	0.30	39.31
GMS0522	65	66	13.56	17.26	25.85	2.29	0.28	40.77
GMS0523	66	67	19.65	20.57	11.80	1.72	0.12	46.14
GMS0524	67	68	14.83	8.51	24.91	0.78	0.08	50.89
GMS0525	68	69	11.49	11.47	22.27	1.94	0.09	52.73
GMS0526	69	70	21.01	14.44	16.33	0.38	0.21	47.64
GMS0527	70	71	21.89	16.15	13.31	1.09	0.20	47.36
GMS0528	71	72	9.83	23.52	7.05	1.57	0.52	57.50
GMS0529	72	73	10.16	18.61	12.16	1.63	0.40	57.04
GMS0530	73	74	16.63	13.98	16.20	1.53	0.41	51.26
GMS0531	74	75	23.05	15.97	11.57	0.60	0.58	48.23
GMS0532	75	76	24.15	15.85	8.56	1.14	0.65	49.65
GMS0533	76	77	18.90	17.16	9.94	1.50	0.42	52.08
GMS0534	77	78	14.64	14.32	10.84	2.35	0.29	57.56
GMS0535	78	79	30.90	12.23	10.43	0.65	0.40	45.40
GMS0536	79	80	30.80	11.36	10.37	0.46	0.45	46.55

Table 3.3: Percentage estimate of 25 cuttings samples from SAM classification

SWIR Core data:

GMS0507 (depth: 65.9 – 67.37m): muscovite (25.83 %), lepidolite (34.96 %), ammonio-smectite (18.29 %), montmorillonite (0.53 %) and unclassified pixels (21.37 %)

GMS0508 (depth: 67.37 – 69.2m): muscovite (46.01 %), lepidolite (13.41 %), ammonio-smectite (10.21 %), montmorillonite (13.59 %) and unclassified pixels (16.75 %)

GMS0509 (depth: 69.2 – 70.34m): muscovite (49.58 %), lepidolite (15.10 %), ammonio-smectite (1.20 %), montmorillonite (7.63 %) and unclassified pixels (26.47 %)

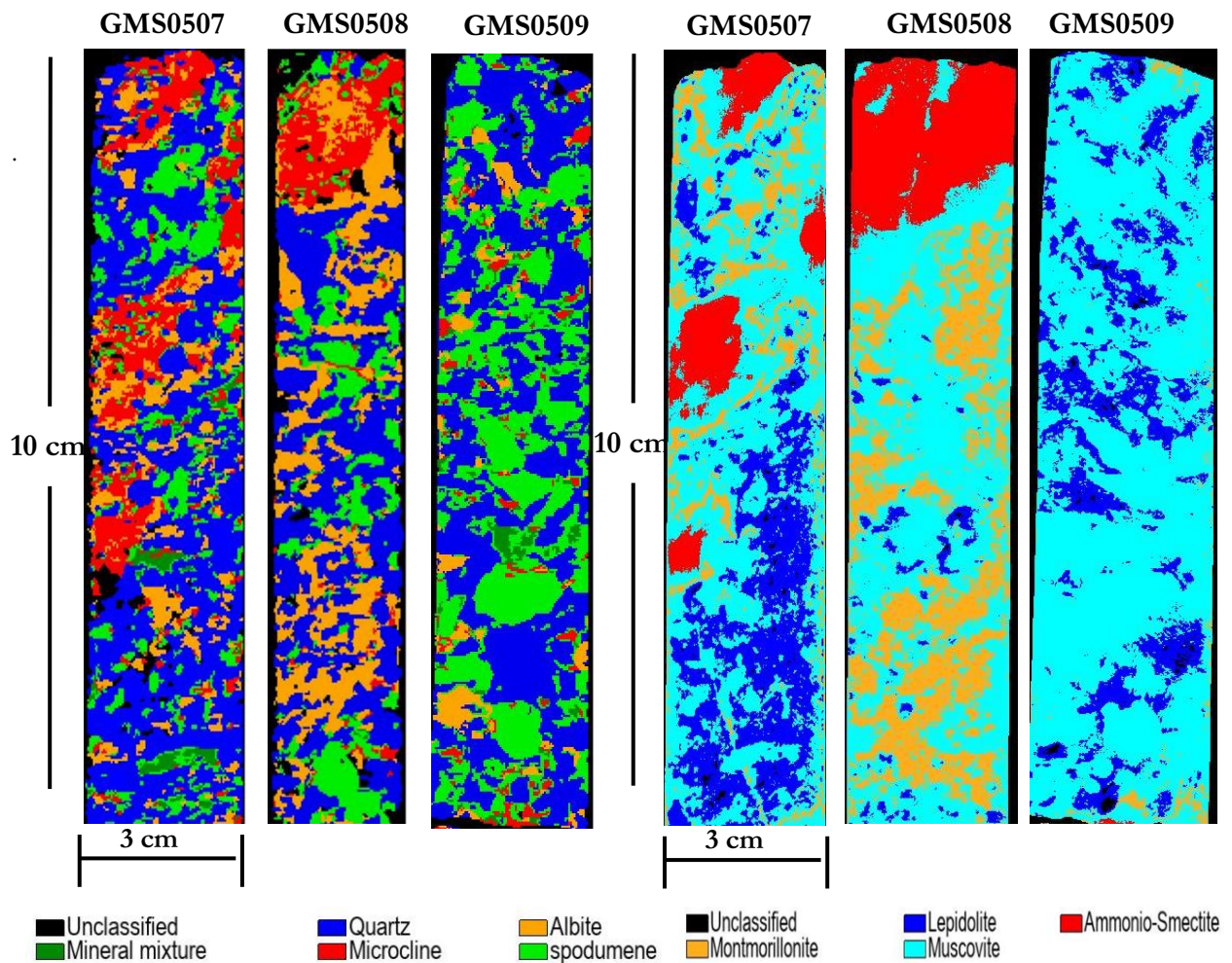
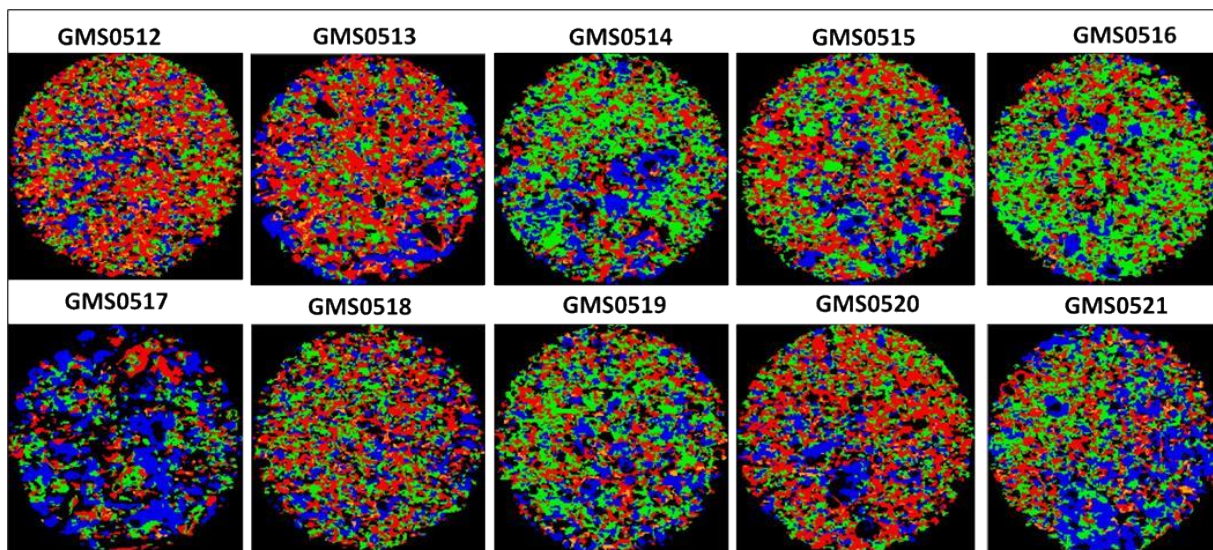
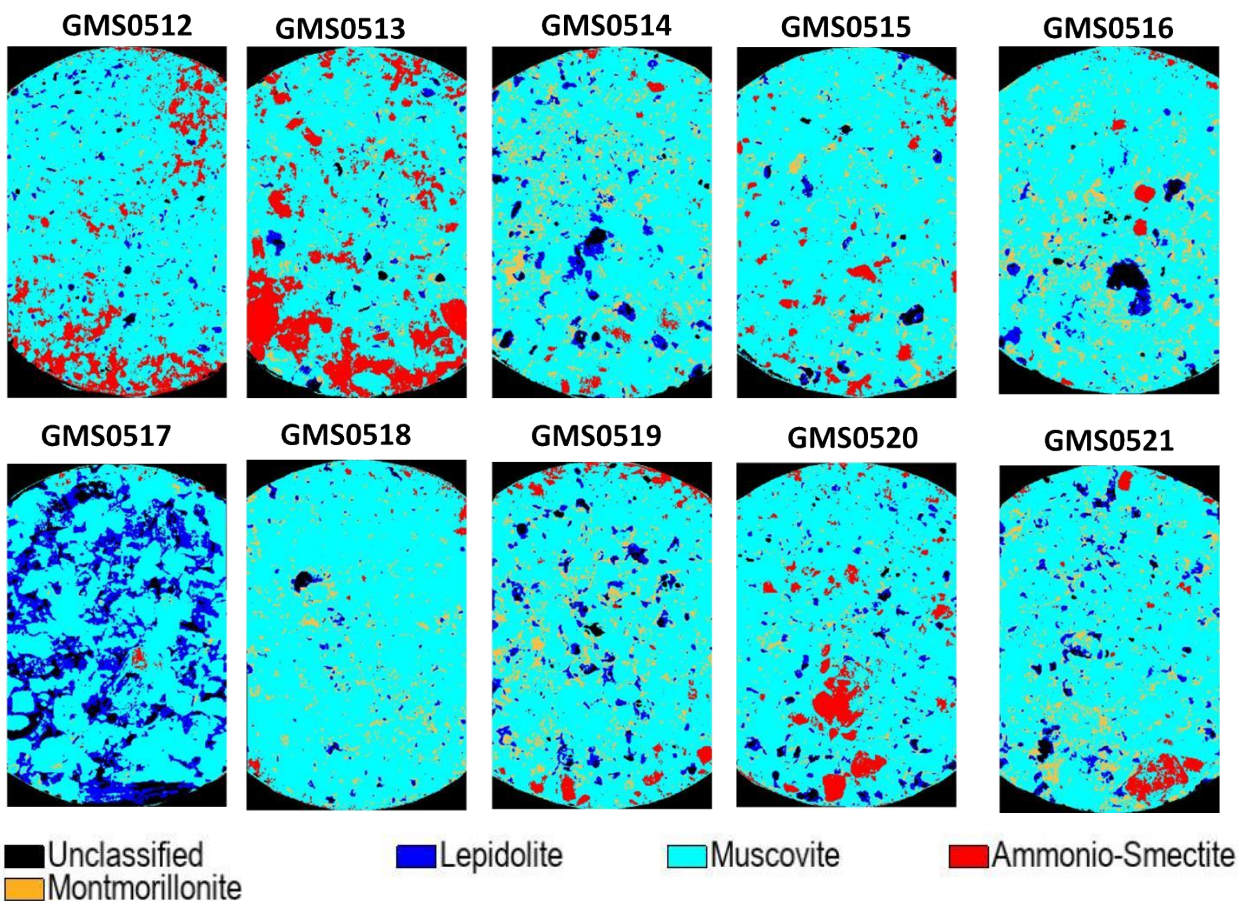


Figure 3.8: LWIR core samples (left), Spectral Angle mapper(SAM) classification showing minerals match for spodumene, Quartz, Albite, Microcline, and mineral mixture, and SWIR core (right), SAM classification showing minerals match for muscovite, lepidolite, ammonio-smectite and montmorillonite. The color pixels represented by each mineral are more similar to the reference spectrum than darker pixels(unclassified). 3 drill core samples section are presented for illustration purposes: GMS0507 (65.90-66.00m), GMS0508 (68.40-68.50m), GMS0509 (70.00-70.10m)



Unclassified
 Mineral mixture
 Quartz
 Microcline
 Albite
 Spodumene

Figure 3.9: Spectral angle mapper images of LWIR cuttings samples showing match for spodumene, Quartz, Albite, Microcline, mineral mixture, and unclassified pixels. The color pixels represented by each mineral are more similar to the reference spectrum than darker pixels (unclassified).



Unclassified
 Montmorillonite
 Lepidolite
 Muscovite
 Ammonio-Smectite

Figure 3.10: Figure 3.9: Spectral angle mapper images of LWIR cuttings samples showing match for muscovite, lepidolite, ammonio-smectite, montmorillonite, and unclassified pixels. The color pixels represented by each mineral are more similar to the reference spectrum than darker pixels(unclassified). Note: due to the spot size of the SWIR camera (6 cm), SWIR cuttings samples were chopped off at the peripheral because the sample holder was larger than the camera field of view.

3.4 X-ray diffraction analysis

3.4.1 Whole-rock XRD analysis of cuttings samples

XRD patterns of 25 cuttings samples detected albite, quartz, microcline, spodumene, muscovite, or lepidolite, and possibly minor traces of other minerals such as petalite and montmorillonite in < 1.0%. For illustration, figure 3.11 displayed a diffractogram of two samples (GMS0514 and GMS0520). The rest of the samples diffractograms and data are shown in *appendix 9*. Other hydrothermal alteration minerals detected from SWIR data were not observed in the XRD pattern, except for Muscovite or lepidolite. An intense sharp peak identified quartz in all samples at 26.7 2-theta(degree). Microcline and albite had adjacent peaks and, in some samples, shows overlapped. Their proximity and overlaps are due to both minerals originating from the feldspar group of minerals. Albite displays four prominent peaks at approximately 22.0, 24.3, 28.5, and 30.2 in all samples at 2-theta (degree). At the same time, microcline shows a single peak at 27.5 degrees. Spodumene displays two shallow but prominent peaks at 30.7 and 32.0 degrees. Muscovite shows a single isolated peak identified at 8.9 degrees and traces of minor peaks overlapping major peaks in the diffractogram. Muscovite and lepidolite had overlapped, creating difficulties in distinguishing both minerals. This overlap was also observed from spectroscopy analysis.

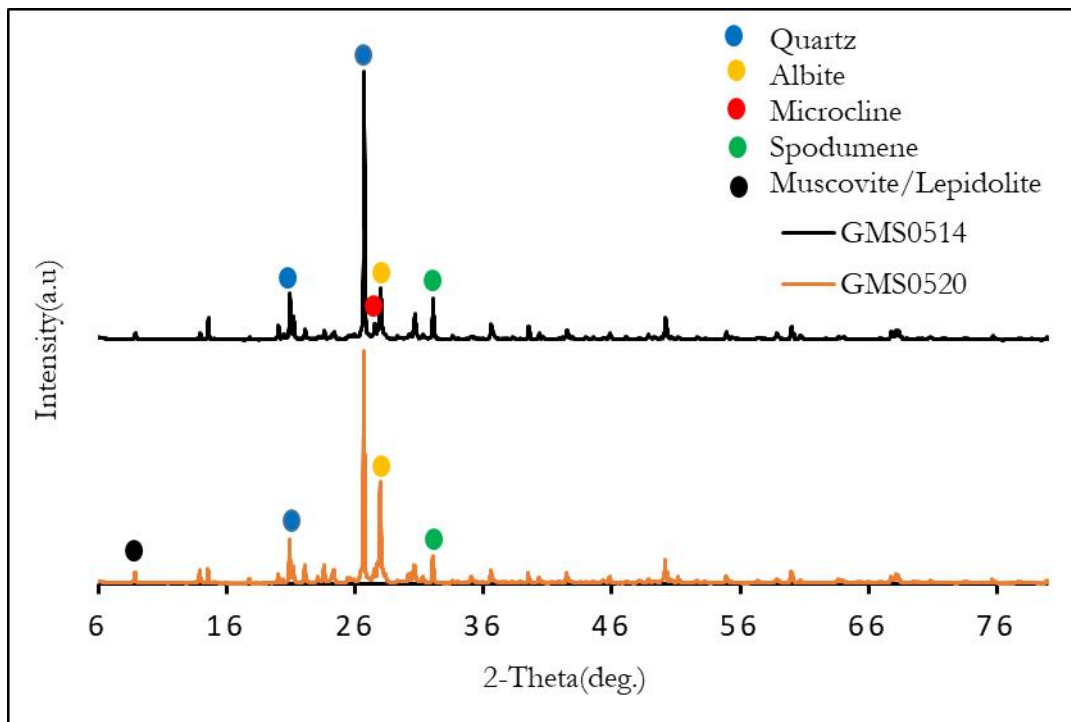


Figure 3.11: A) Representative whole-rock XRD diffractogram of sample GMS0514 and sample GMS0520 showing peaks of quartz, albite, microcline, spodumene, and muscovite or lepidolite.

3.5 Quantitative comparison: HSI and XRD on cuttings

Modal mineralogy determined by the SAM method on screened (>0.5 mm) and washed cuttings samples at all 100 cm intervals were compared to the results of whole-rock XRD analysis on milled (unscreened, unwashed) cuttings. The database used for this analysis is displayed in *appendix 12*. It includes mineral abundance estimates from SAM-LWIR and XRD cuttings. Figure 3.12 displayed a mineral abundance plot for minerals common in all datasets (HSI and XRD), including spodumene, quartz, albite, and microcline. The calculated correlation coefficient from a linear regression for selected samples revealed no statistically significant positive or negative relationship between both datasets, except for quartz with $R^2 < 0.1766$ and $p\text{-value} < \alpha$ ($\alpha = 0.05$). Additionally, a graphical representation of HSI and XRD mineral abundance for all 100cm cuttings samples were plotted against their relative depths (figure 3.13).

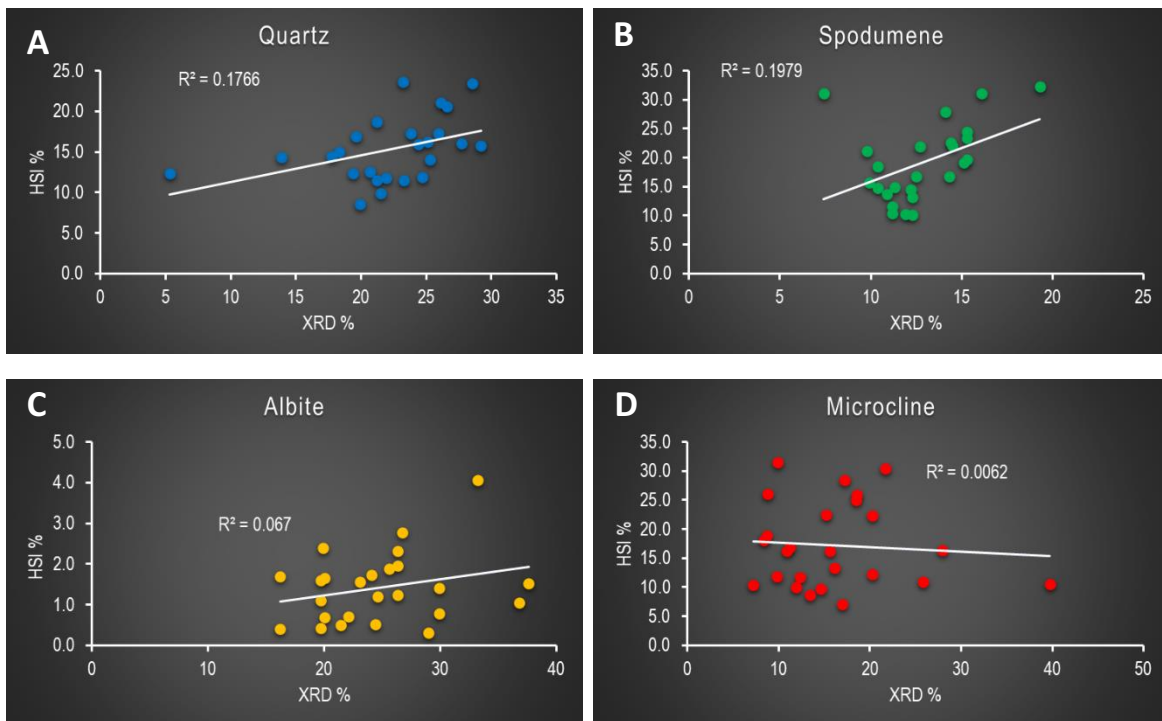


Figure 3.12: Correlation plots of HSI (LWIR) versus XRD mineral abundances on 25 cuttings samples for spodumene(green), quartz(blue), microcline(red), and albite(yellow)

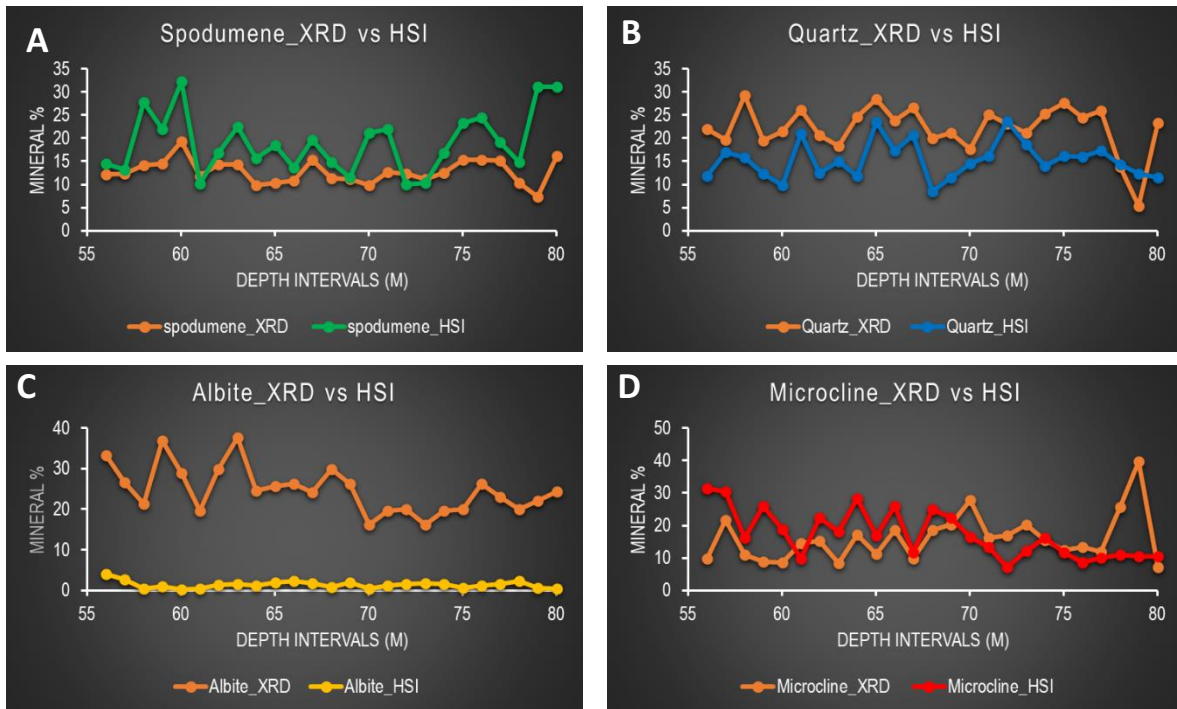


Figure 3.13: Graphical plots of HSI (LWIR) versus XRD mineral abundance on 25 cuttings samples for spodumene(Green), quartz(blue), albite(yellow), microcline(Red), and XRD data for each mineral in orange.

3.6 Spodumene crystal size analysis

Modal mineralogy of spodumene, quartz, albite, and microcline determined by SAM method on continuous ~4m LWIR core were plotted together with the mean of the three largest spodumene crystals size in every 10cm intervals against their relative depths, as illustrated in Figure 3.14. Visual inspection of the plots shows variations in mineral abundance and spodumene crystals size (area, in mm²). Based on a predefined threshold, If the mean of the three largest spodumene crystals size in a 10 cm interval was larger than a threshold value ≥ 100 mm², the interval was described as coarse spodumene crystals (P1); otherwise, the interval was deemed fine spodumene crystal(P2). Spodumene crystals cluster labeled from 'a to b' were mainly described as 'P2' intervals with crystals size < 60 mm², corresponding to depth intervals 65.9 to 67.4 meters, while those labeled from 'c to h' were dominantly described as 'P1' intervals with crystals size > 150 mm² but with some 'P2' intervals mixed, corresponding to depth intervals 67.5 to 69.1meter. Spodumene crystals cluster labeled from 'i to j' were mainly described as 'P2' intervals, corresponding to depth intervals 67.8 to 68.7 meters. Those labeled from 'm to n' were mainly classified as 'P1' intervals, corresponding to depth intervals 69.6 -70.3 meters, but with some 'P2' intervals mixed labeled from 'k to l' corresponding to depth intervals 69.2 to 69.9meters. The relationship between the mean of the three largest spodumene crystals size and modal spodumene, albite, quartz, and microcline, was determined based on a linear correlation calculation, as illustrated in Figure 3.16. The result revealed no statistically significant positive or negative relationship between modal albite and microcline and spodumene crystal size. Modal spodumene revealed a statistically significant positive relationship with spodumene crystal size, with $R^2 = 0.4439$, and modal quartz revealed a negative relationship with $R^2 = 0.1259$. However, the summary output for modal quartz show statistically significant with P-values $< \alpha$ (consider alpha = 0.05), as shown in *Appendix 14*.

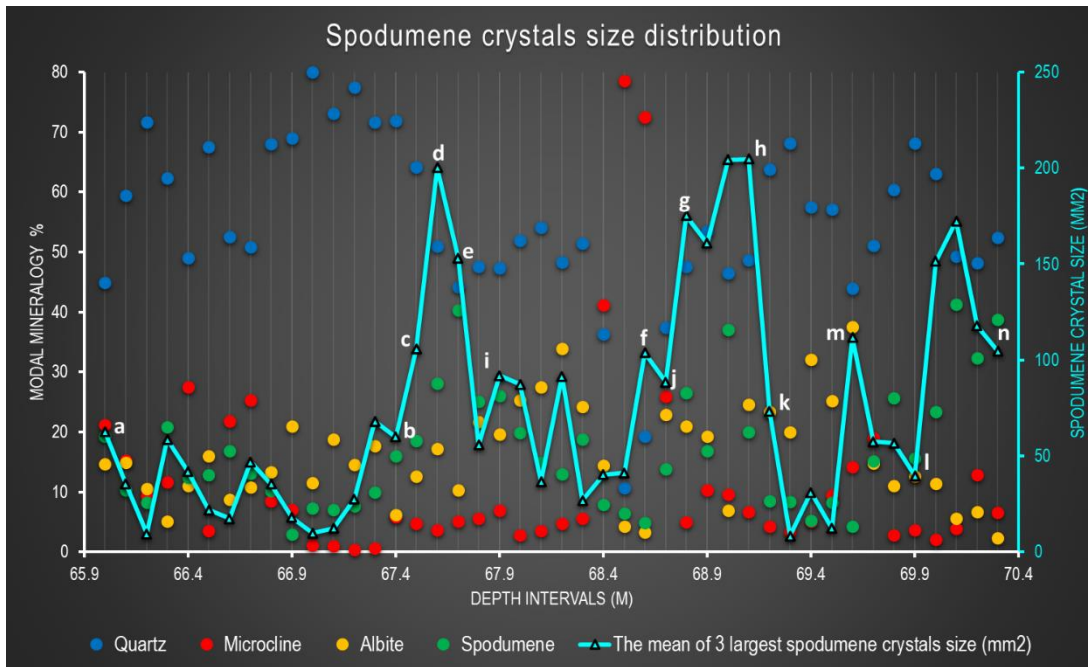


Figure 3.14: The mean of the three largest spodumene crystals size (cyan) in each 10 cm interval plotted together with model mineralogy for quartz (blue), albite (yellow), microcline (red), and spodumene (green) relative to their depths.

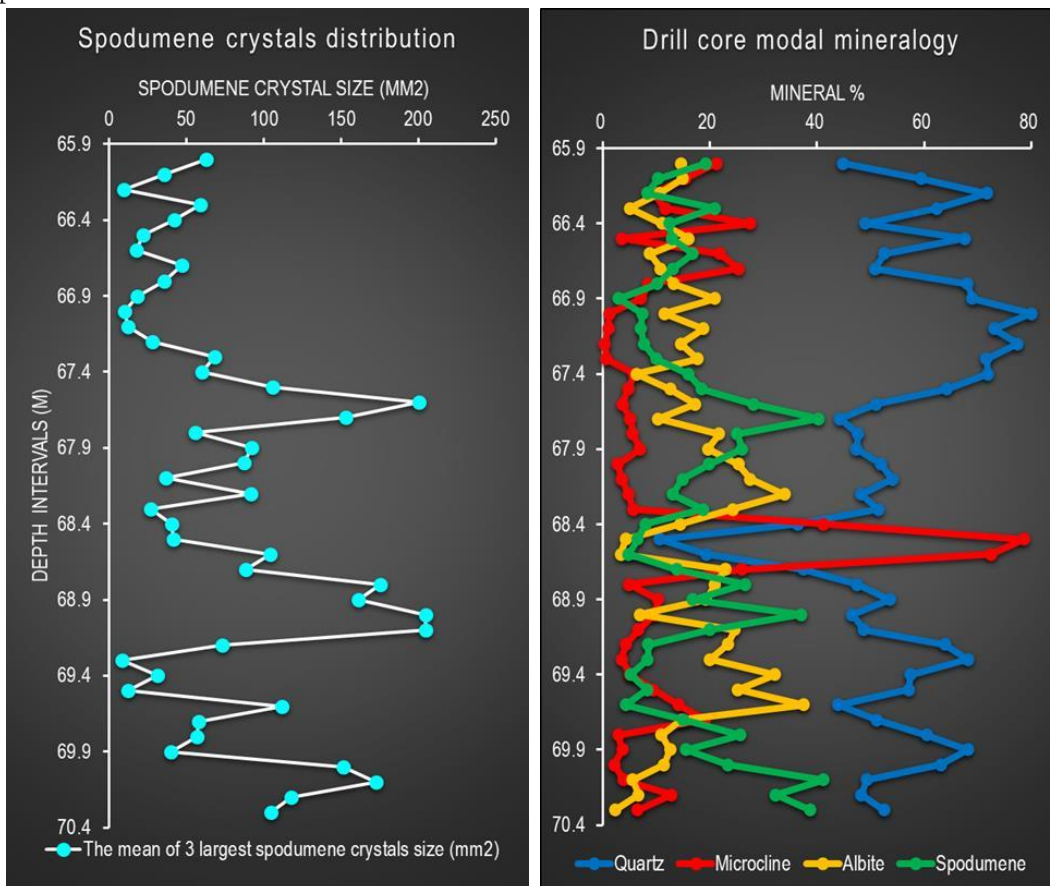


Figure 3.15: A) Spodumene crystals size(area, in mm²) distribution plot, B) Model mineralogy (right) for quartz (blue), albite (yellow), microcline (red), and spodumene (green) plotted against their relative depths.

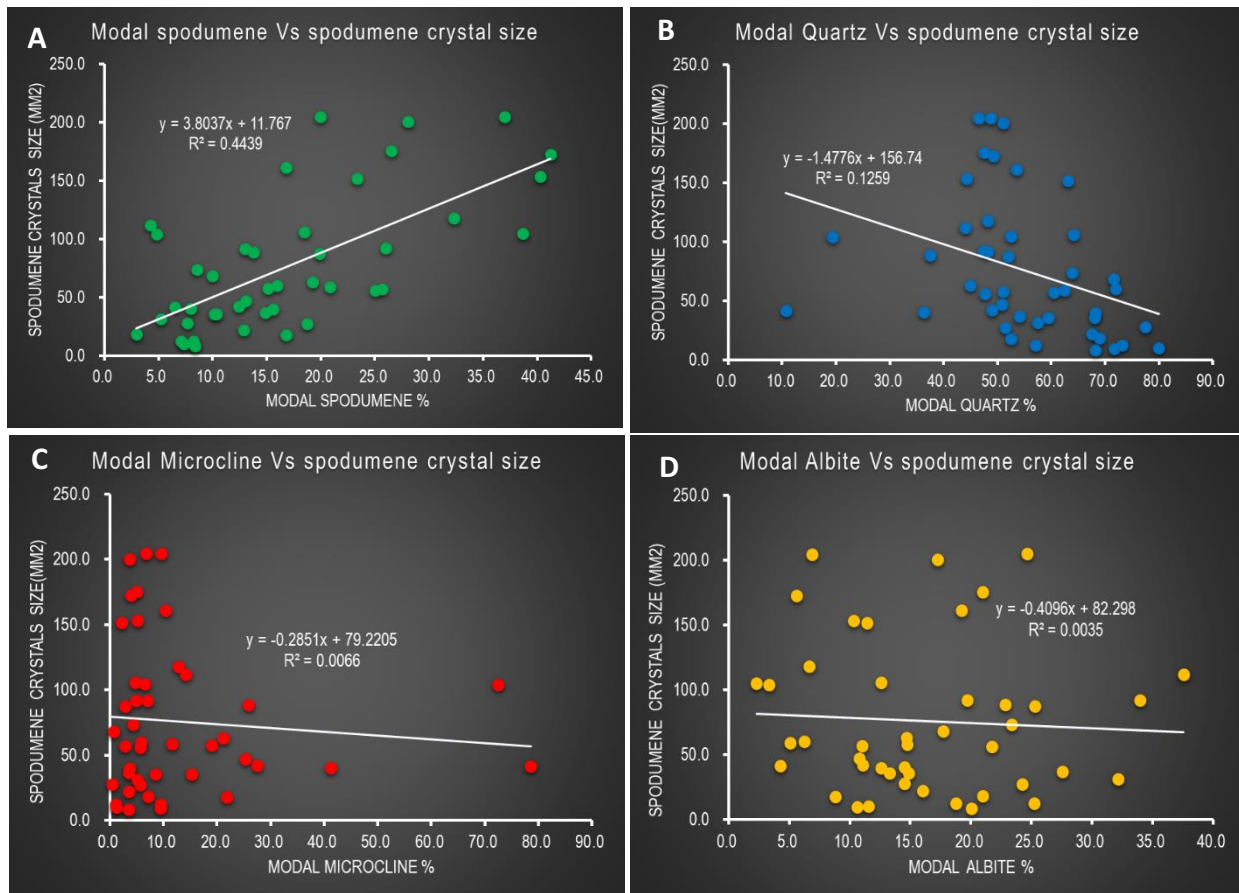


Figure 3.16: Correlation plots of modal % of albite, microcline, quartz, and spodumene, based on SAM-LWIR versus spodumene crystal size (area, in mm², of the three largest spodumene crystals in each interval) for the available core interval of continuous ~4m core sample.

3.7 Core versus cuttings Mineralogy

The modal mineralogy in the core as determined by the SAM-LWIR classification method was compared to the modal mineralogy in the sieved and washed cuttings, also determined by the SAM-LWIR method, and to the modal mineralogy in the unsaved, unwashed cuttings as determined by XRD. For this purpose, datasets from both methods determined to be extracted from twin drill holes (GDD00** and GRC00**) at exactly the same depth intervals were plotted and linearly correlated, thus establishing a relatively simple mineralogical proxy between both datasets. The result revealed no statistically significant positive or negative relationship between both datasets at any reasonable uncertainty level. Moreover, given the low number of points, the number of degrees of freedom ($df = 4$) was also attributed to the non-significant results. Each 100cm core section labeled GMS0507, GMS0508, GMS0509, and cuttings samples labeled GMS0523, GMS0525, and GMS0526 were determined to be extracted from exactly the same depth intervals. Furthermore, The above datasets were plotted on a one-to-one relationship line to cross-check any issue derived from sample preparation(sieved and washed) relative to the non-statistically significant results. In addition, graphical representations of both datasets are presented to match the so-called samples determined to be from precisely the same depth intervals for confirmation (figure 3.22 A and B).

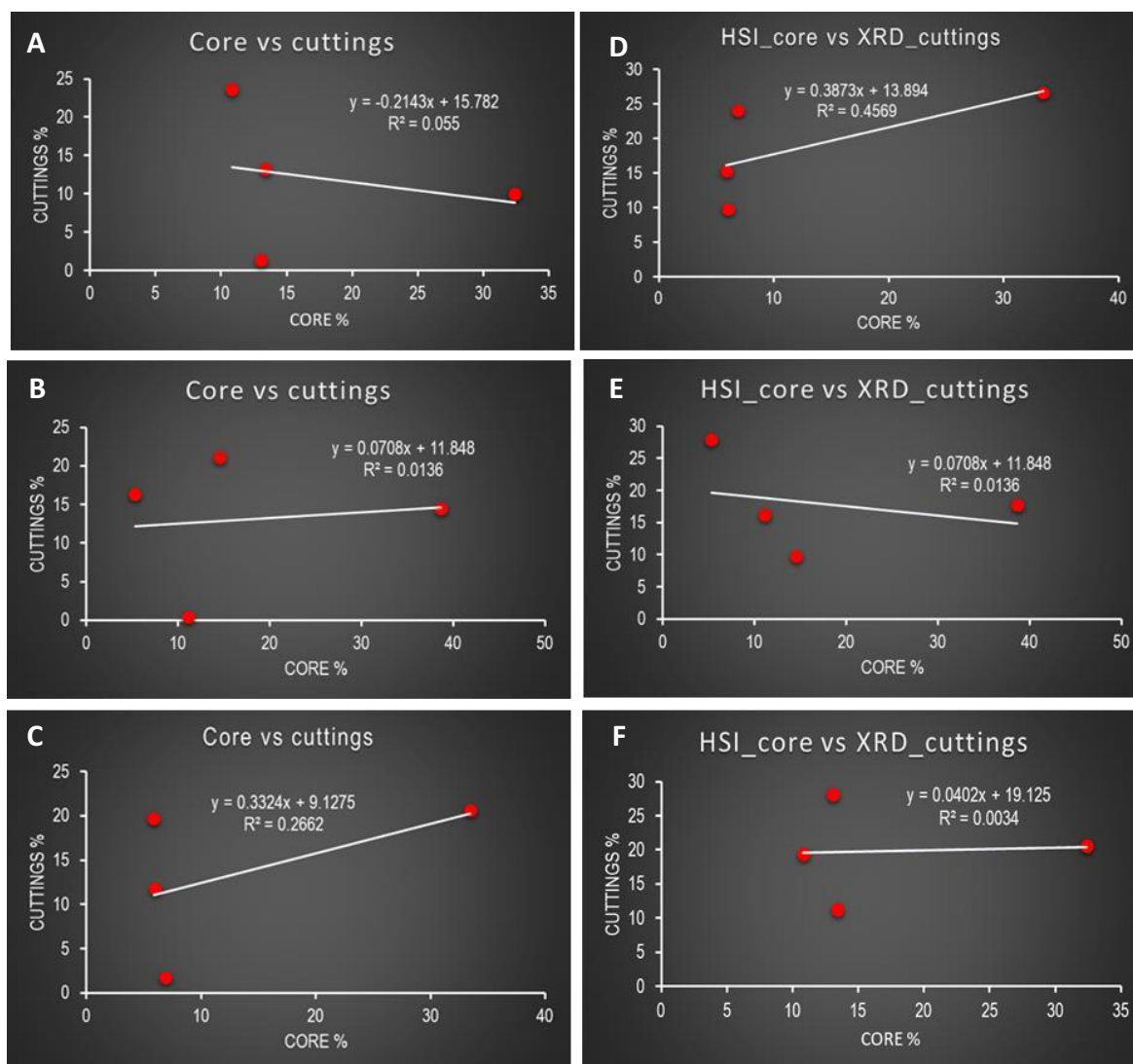


Figure 3.17: A,B,C) Correlation plots of HSI-SAM core versus cuttings of 100cm samples at the same depth intervals. D,E,F) HSI-SAM core versus XRD cuttings of 100cm samples at the same depth intervals.

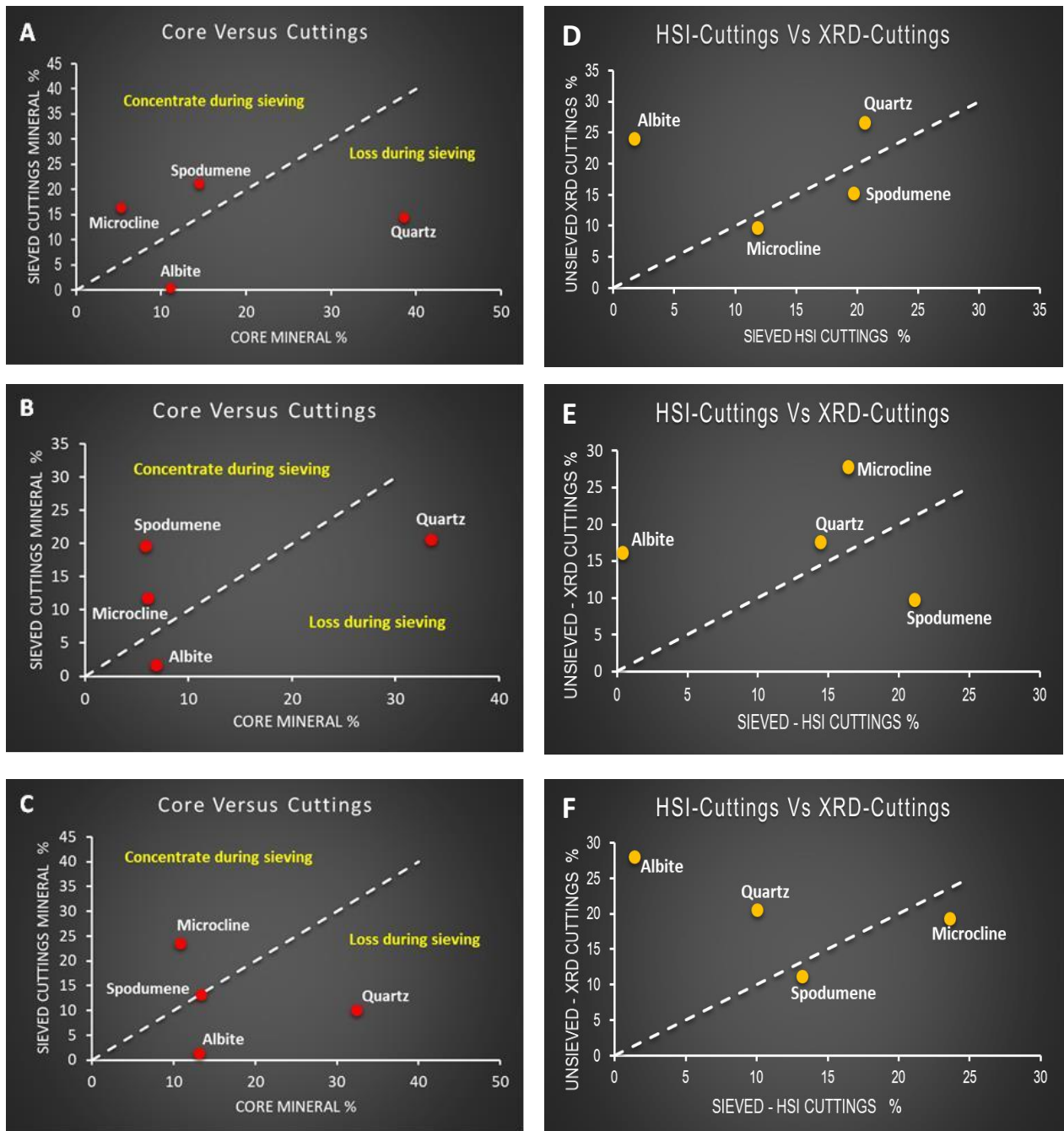
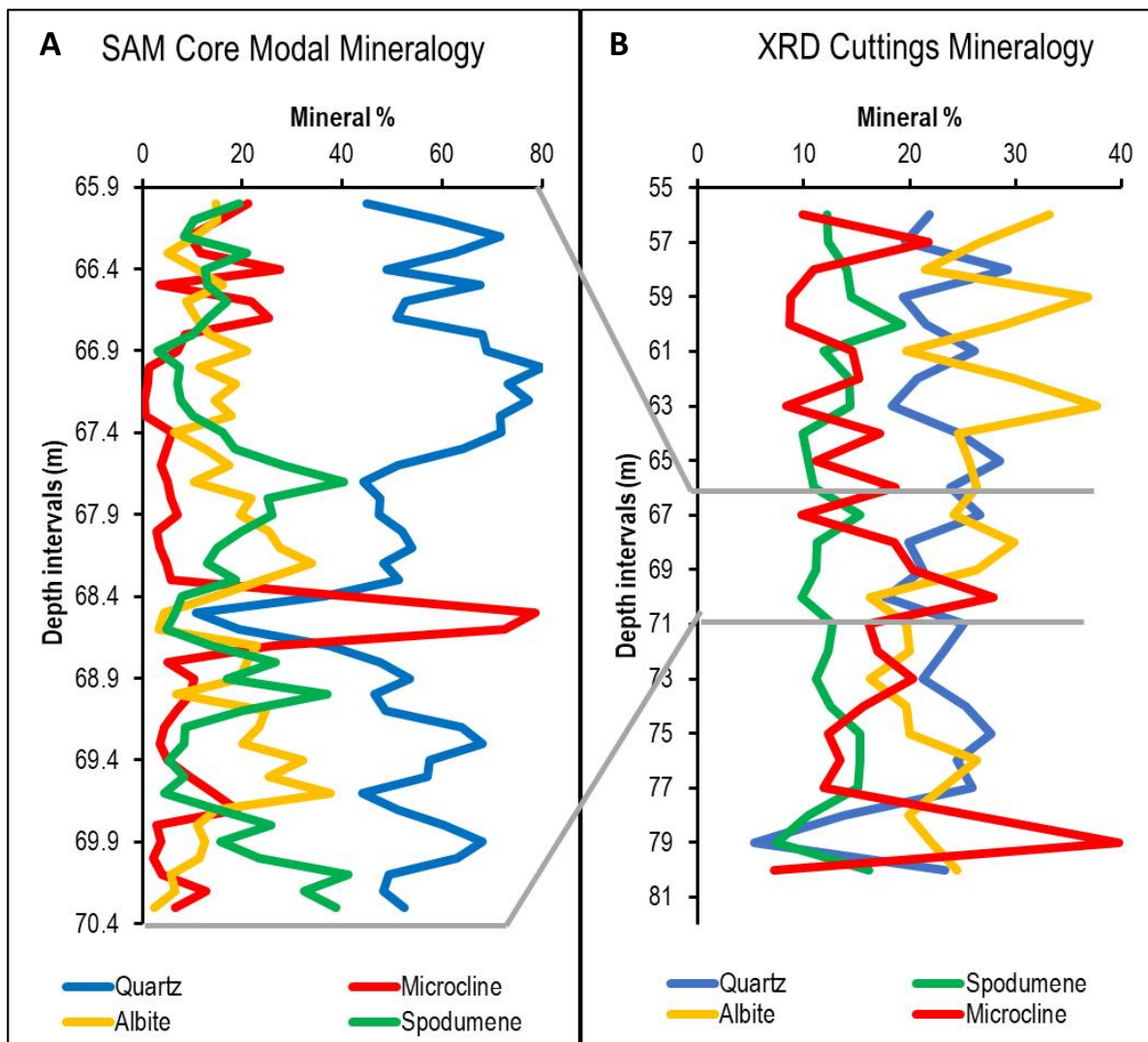
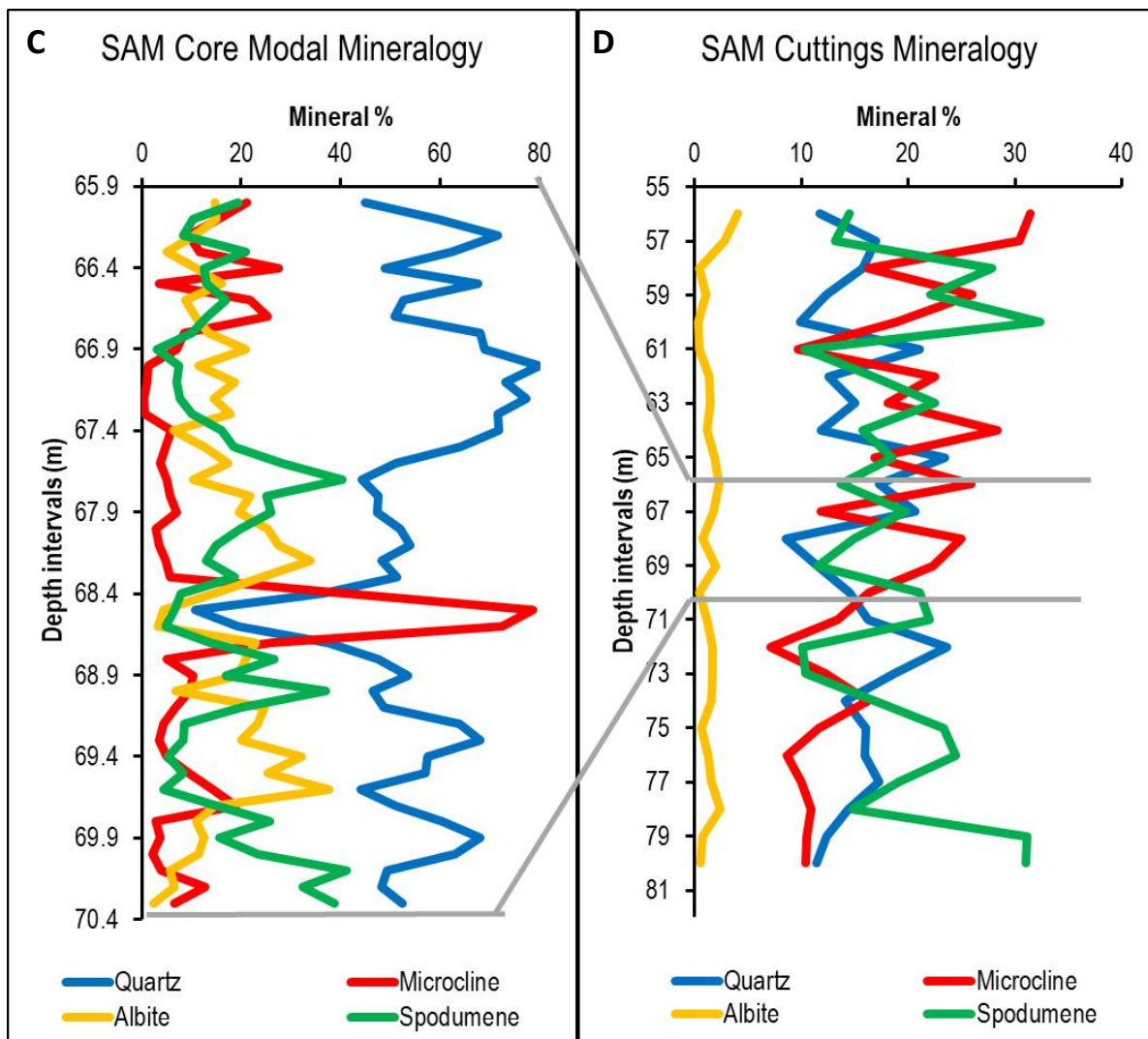


Figure 3.18: A, B, C) Correlation analysis of SAM-LWIR core against SAM-LWIR cuttings mineralogy and D, E, F) SAM-LWIR cuttings against XRD cuttings mineralogy plotted on a one-to-one relationship line.





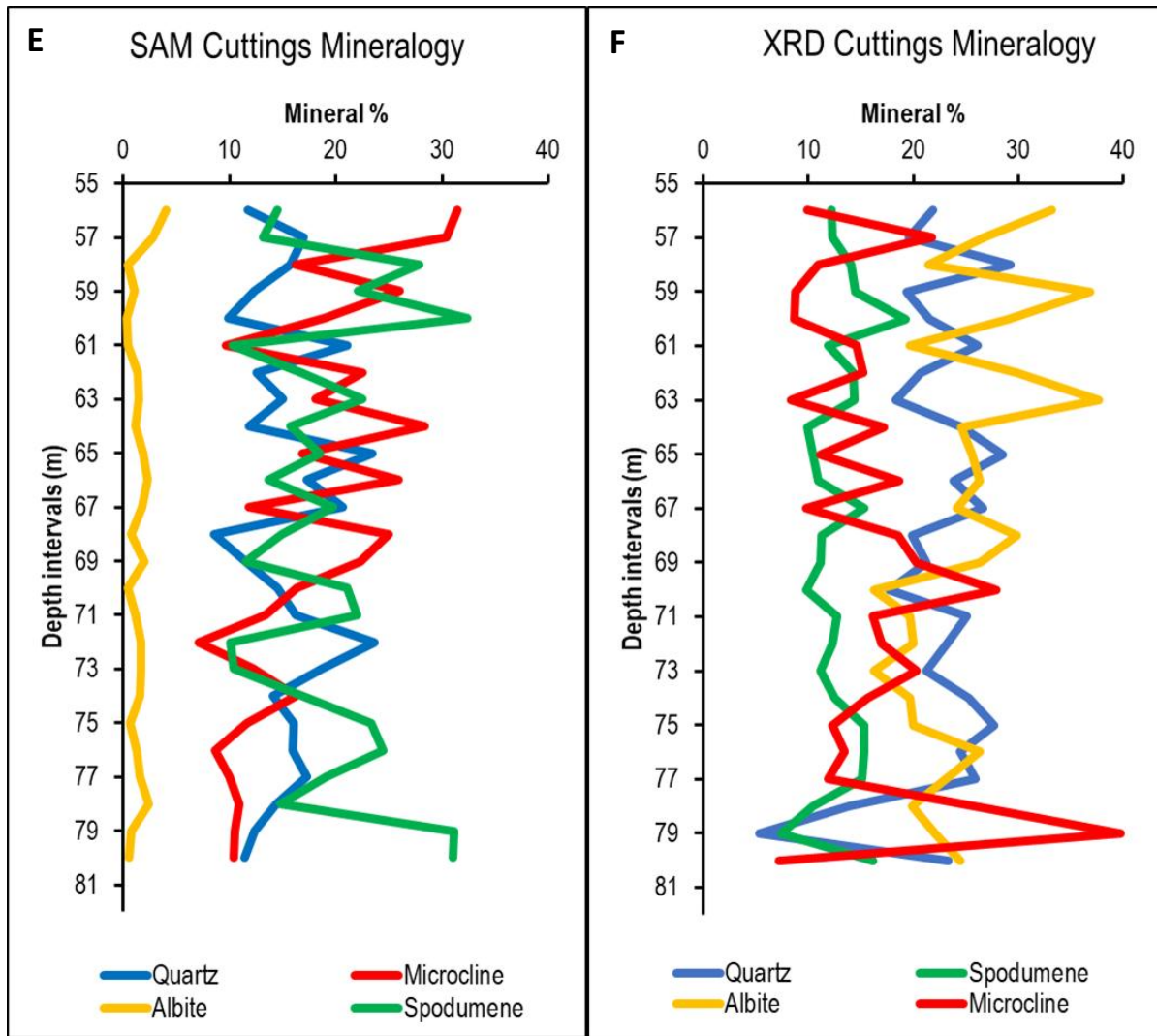


Figure 3.19: A & B) Graphical plots of SAM-LWIR core and XRD cuttings mineral abundance, C & D) SAM-LWIR core samples and SAM-LWIR cuttings mineral abundance, E & F) SAM-LWIR cuttings mineral abundance and XRD cuttings mineral abundance for continuous ~4m core sample against their relative depths.

4. VALIDATION

4.1 XRD Validation

Five scratched-out spots in selected locations on the core were analyzed using XRD based on SAM-LWIR classified images from different depths in all 100cm core samples of the investigative datasets. Each scratched spot represents different mineral species of dominant spodumene, albite, and microcline identified from SAM classified images. Mineral identification shows several best match peaks generated by the DIFFRAC. EVA version 3.1 software for spodumene, quartz, microcline, and albite (table 4.1). All scratched powders samples show minor peaks of other minerals present as inclusion.

ID	depth(m)	XRD code	HSI	Microcline_XRD %	Albite_XRD %	Quartz_XRD %	Spodumene_XRD %	Muscovite/lepidolite %
A	66.69	22111	Microcline	58.5	22.1	4.7	2.9	11.7
B	69.93	22115	Spodumene	7.8	16.2	2.4	60.6	13.1
C	68.25	22116	Microcline	47.9	24.6	2.6	9.3	15.6
D	68.98	22117	Albite	5.5	78.1	1.4	6.8	8.2
E	69.62	22125	Spodumene	22.1	21.1	1.4	36.7	18.7

Table 4.1: Five samples scratched out core samples from XRD analysis and HSI validation. The highlighted colors for each mineral are derived from the SAM classification of the cores. The approximate depth of each scratched spot within a 10cm interval. Note: values in bold indicate the abundance percentages per scratched spot.

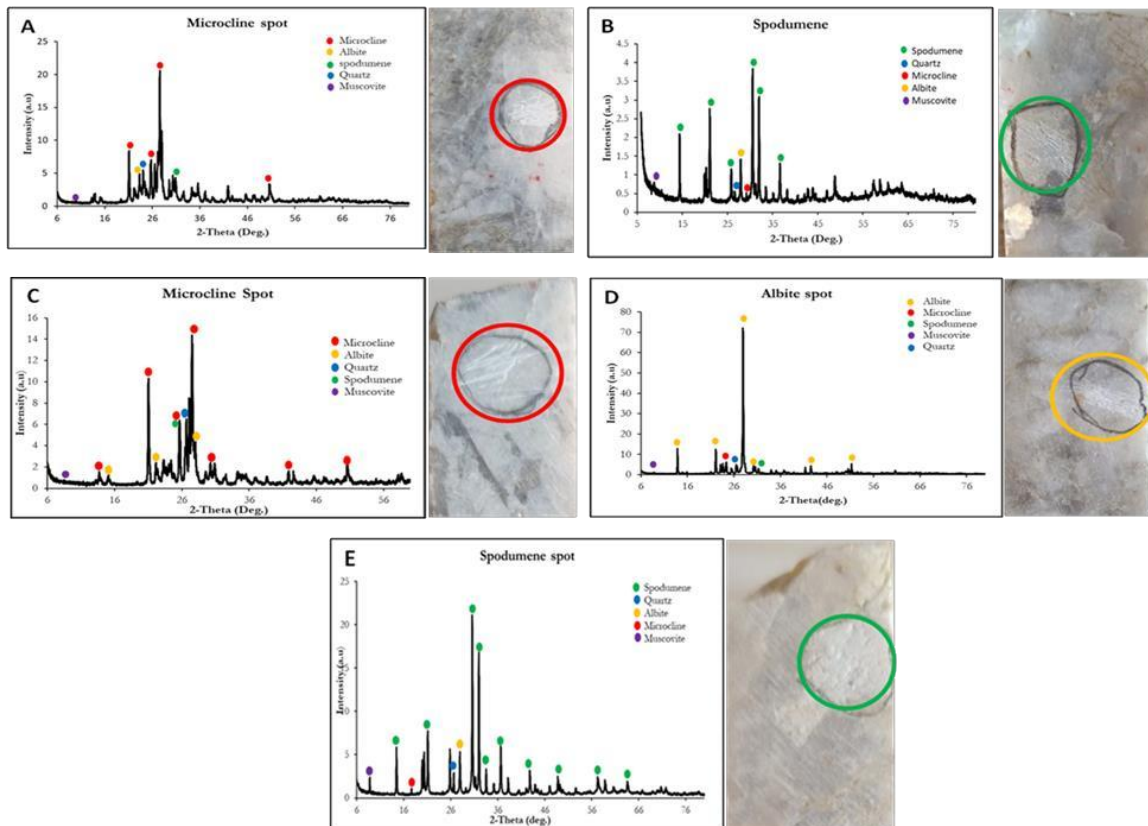
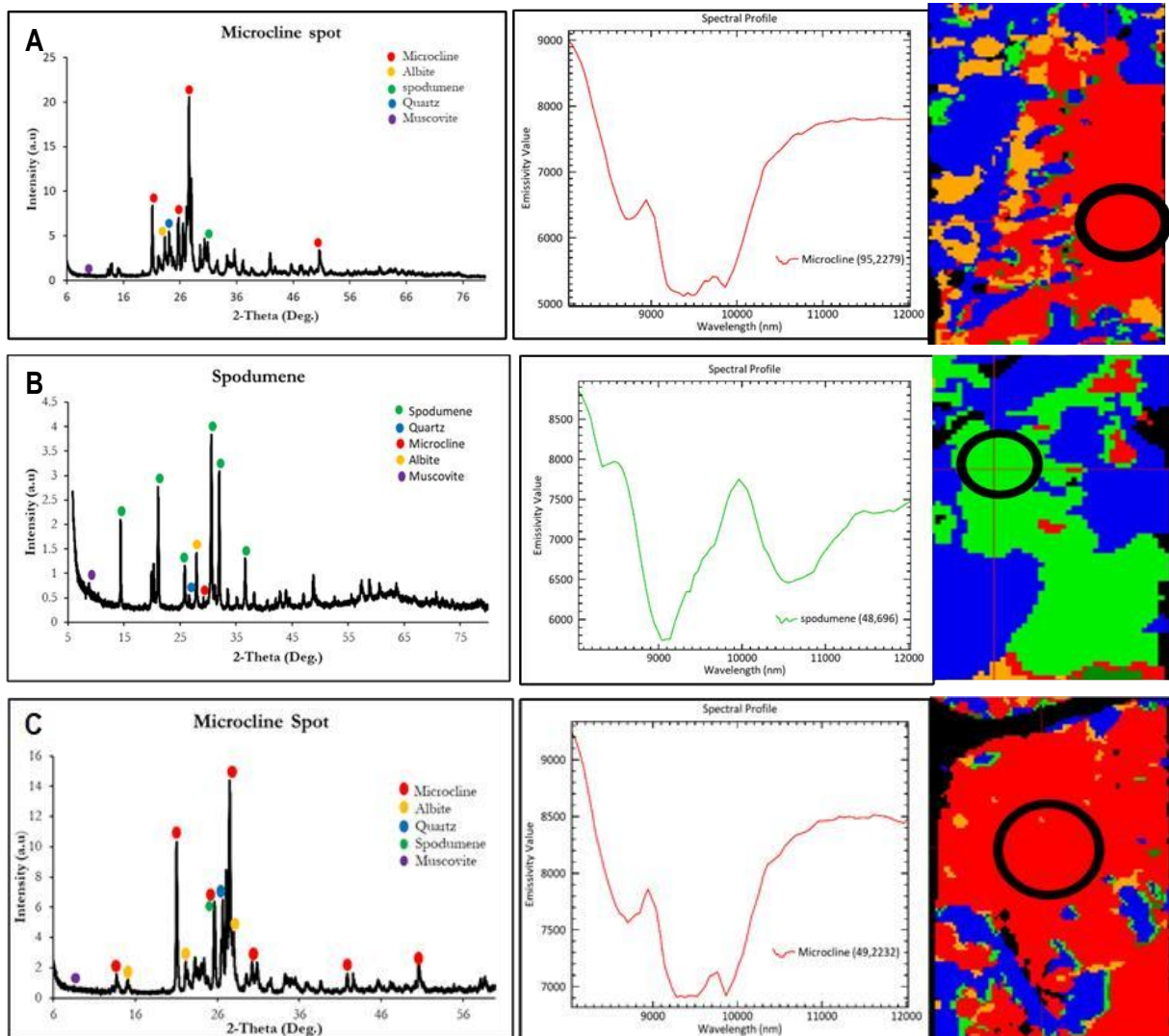


Figure 4.1: scratched-out powders XRD spot-based analysis pattern of spodumene(B & E), Microcline (A & C), and Albite (D). Diffractograms of each sample show dominance of all three minerals, indicated by their color dot and sharp peaks. All scratched powders samples show a minor peak of other minerals present as inclusion.

4.2 Spectral Validation

In addition to XRD spot check analysis, spectral verification was done on the same spots used for XRD analysis on LWIR SAM classified images. This was done by randomly inspecting and verifying spectra from spots in the images. Moreover, a few classified and unclassified features in the LWIR and SWIR classified images were also checked. Visual inspection of the unclassified pixels in the core and cuttings were generally related to pixel saturation and background interference from the sample holder. Saturation pixels were derived from image data acquisition due to instrument exposure time for a single measurement. This leads to a negative emissivity value after reflectance to emissivity conversion. Lastly, the cuttings samples holder was very shallow, and sample fragments were not nicely interconnected to restrict infrared light from penetrating; as a result sample holder background was also imaged and produced weird spectral which were not representative of the pure mineral spectral used for classification, thus classifying as unclassified pixels in the SAM classifier (figure 4.5 A to D).

Results from spectral validation of various spots spectrum show a perfect match for each identified SAM classified mineral (figures 4.3 A to D, figure 4.4 E to F).



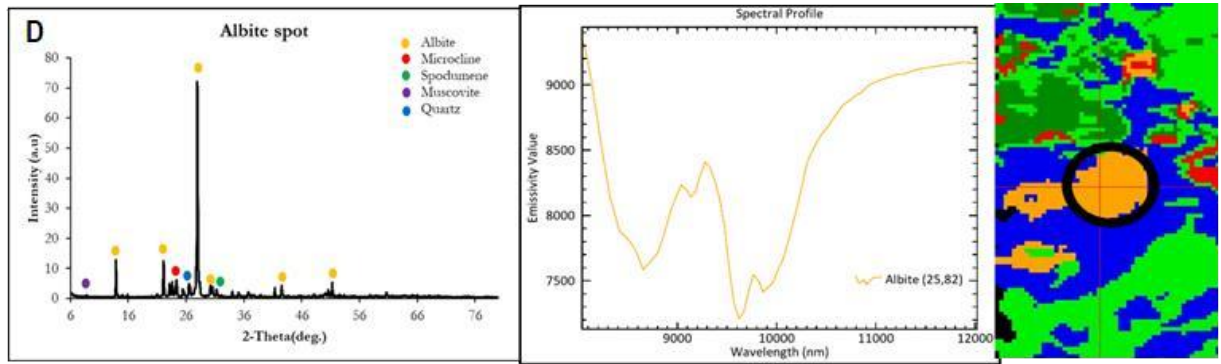


Figure 4.3: A to D, showing spectral validation on specific spots from LWIR SAM classified images for microcline, spodumene, and albite with corresponding XRD diffractogram (left). Note: the black circles indicate pixel location.

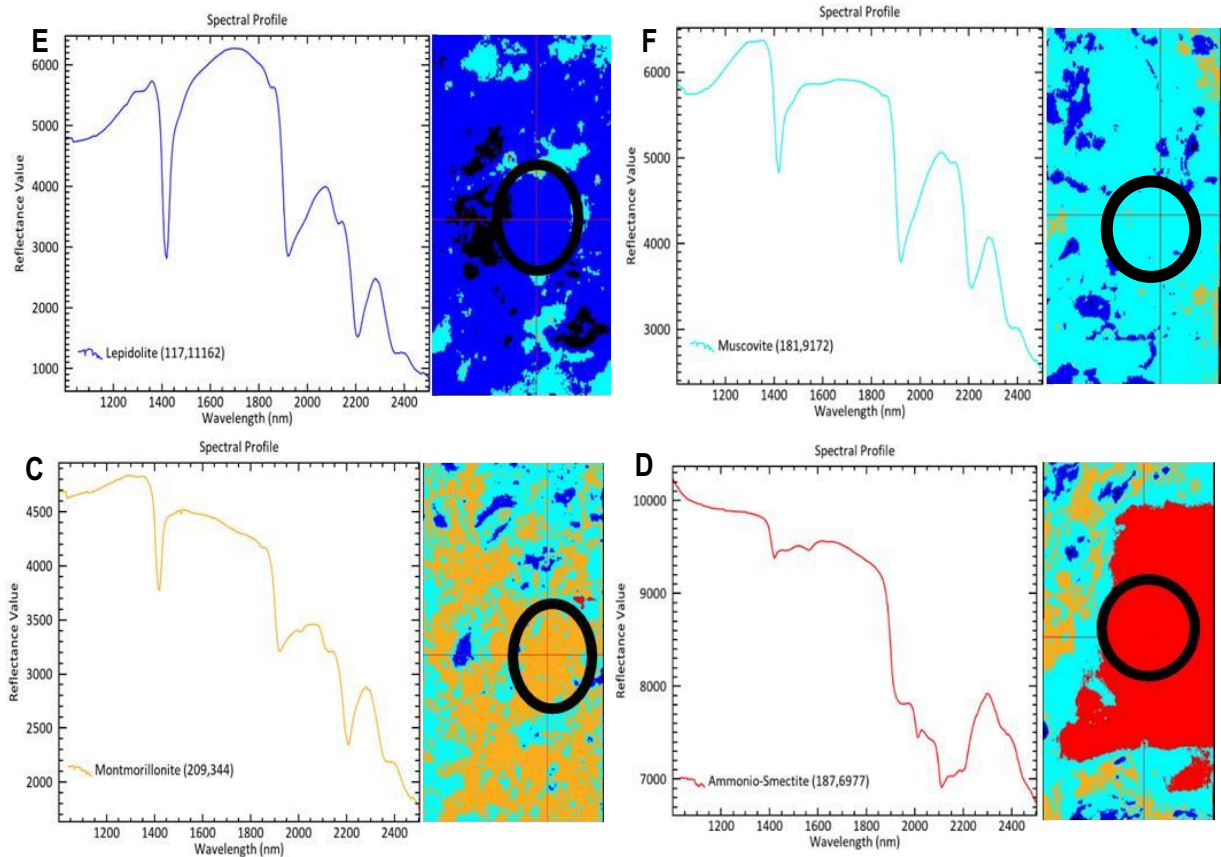


Figure 4.4: E to H, showing spectral validation on specific spots from SWIR SAM classified images for muscovite (F), lepidolite(E), montmorillonite(G), and ammonio – smectite (H). Note: the black circles indicate pixel location.

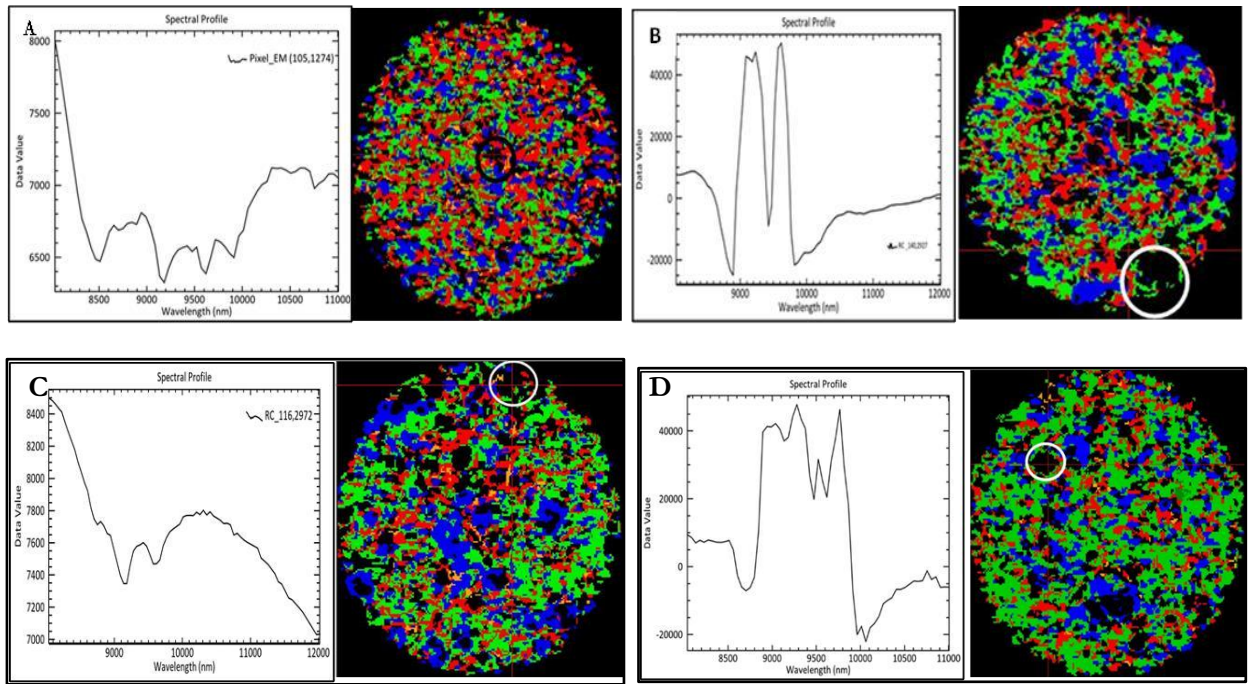


Figure 4.5: A to D, showing cuttings spectral from saturated pixels and background spectrum from the sample holder. A and C) Background spectrum, B and D) spectrum from saturated pixels. Note: the black circles indicate pixel location.

5. DISCUSSION

This chapter discusses methods and results in chapters two and three. Mineral identification and mapping, spodumene crystal size analysis, comparative analysis, and discrepancies derived from methods employed are discussed in detail. Spodumene crystal size data was integrated with SAM-LWIR mineralogy to display crystal size distribution and minerals associated with P1 and P2. This study excluded SWIR datasets for quantitative and crystal size analysis because they could not provide relevant information relating to research objectives.

5.1 Methods

Pegmatite core and cuttings samples were used to acquire hyperspectral images in the longwave-infrared (LWIR) of 6923 nm to 22206 nm and shortwave-infrared range (SWIR) of 989 nm to 2503 nm wavelength ranges. These wavelength ranges encompass noisy spectral bands, which decrease image quality and negatively influence detecting targeted minerals of interest for the research. These subsetted bands ranged from 8000nm to 12000 nm for LWIR and 1000 nm to 2500 nm for SWIR. Subsetted ranges were significant in detecting target minerals of interest. The acquired hyperspectral core and cuttings show some artifacts derived from image acquisition, such as pixel saturation resulting in an exponential increase of reflectance values, thus leading to negative emissivity and background reflectance interference.

Additionally, saw marks on cores derived from the drilling process create noise in specific regions. Pixel saturation and background reflectance interference were observed in all core and cuttings LWIR and SWIR images resulting in increased unclassified pixels, as presented in figure 4.5 and appendices 1-8. These conditions could have been attributed to the self-emission effect when samples were exposed to infrared light. Some mineral surfaces are very transparent; when exposed to light beyond their ability to be contained, it causes saturation. In addition to the scanning instrument's slow pace, minerals with low heat capacity get warmer faster and emit energy. This has distorted some spectral information creating a weird shape in the endmember identification and mapping, resulting in more unclassified pixels. However, improving acquisition procedures and increasing the quantity of cuttings samples would help resolve these issues.

Two basic algorithms were involved in preprocessing the acquired images for noise reduction and enhancing mineral spectral features. These include minimum noise fraction transformation for further noise reduction and facilitating endmembers extraction and spectral angle mapper (SAM) for mineral mapping. The red, green, and blue(RGB) MNF 4,3,2 were used to facilitate manual digitization of different color regions representing a specific mineral in the investigative dataset for endmembers extraction using a simple semi-quantitative method (Region of interest, ROI). However, this method is prone to little error in the digitization process, which could lead to including regions out of the defined ROI. Multiple ROI were digitized, and endmembers were extracted due to minerals showing different color hues. Endmembers of similar shape and wavelength positions were averaged, and final endmembers were used for mineral mapping by spectral angle mapper (SAM) algorithm. XRD validated the identified minerals from SAM-classified LWIR and SWIR images. Prior to mineral quantification, minerals relative abundances from SAM-LWIR were inclusive of unclassified pixels and mineral mixture, resulting in false positive abundances for each mineral. Their presence influenced the quantification. Therefore, the unclassified pixels were subtracted from the total pixels for each interval to obtain the total classified pixels. The obtained classified pixels were divided by each mineral's classified pixels and multiplied by 100 to get the relative abundance percentage for each mineral used to develop the modal mineralogy used for comparative analysis. Manual spodumene crystal size measurements from print-out classified LWIR core images were employed. Results were plotted and correlated with modal mineralogy against their relative depth.

5.2 Endmembers identification and extraction

Mineral identification is the most significant aspect of the presented Hyperspectral LWIR and SWIR analysis. Wrong identification of minerals would lead to misinterpretation of SAM classification results. Therefore, an excellent spectral library is crucial for sound classification. LWIR and SWIR identified significant differences in the minerals they detect in the exact pixel location of the images. For instance, sample GMS0507 of the LWIR detected microcline as one feldspar group of minerals but within the same pixels of the SWIR data shows ammonia smectite mineral. This indicates that the SWIR wavelength range was sensitive to identifying hydrothermal alteration minerals not detected by LWIR. Mineral identification in the LWIR images was not challenging compared to the SWIR. Mineral endmembers detected in the LWIR had distinct features in distinguishing various minerals except for albite and microcline, which look similar but different in their emissivity minima. Albite was detected by its subtle feature and doublets at 9571nm and 9963nm, and microcline by its triplets emissivity minima at 8512 nm and 9963 nm.

The mixed spectrum identified from LWIR dataset closely matched the lepidolite spectrum from USGS library. However, it was not convincing to consider the spectrum as lepidolite (Figure 3.6E). The so-called mixed spectrum had a strong spodumene feature at 9038 nm. However, the spectrum was observed to be distorted at 8417nm wavelength position of quartz, thus creating a quartz-spodumene mixture. Similarly, the mixed spectrum was distorted at 9571 and 9815nm, thus creating a microcline-albite-spodumene. Generally, all identified spectra in the LWIR wavelength range had significant overlaps, thus creating challenges in selecting the correct threshold values. For example, all four identified LWIR endmembers overlapped at 9038nm. The SWIR range identified four distinct but significantly overlapped endmembers at 2206nm, indicating the presence of Al-OH. Mineral identification was challenging due to such overlap. For example, the lepidolite spectrum overlapped with muscovite at 2206nm, 2357nm, and 2469nm, creating challenges in distinguishing both minerals. This was confirmed in the XRD analysis, with both minerals peaks overlapping at 8.9 2-theta degrees. Similarly, montmorillonite and ammonia smectite also show identical overlaps but were not detected from XRD.

5.3 Hyperspectral SAM mineral mapping

Hyperspectral imaging is non-contact, non-destructive, with little to no sample preparation technique. It is traceable, measurable, fast, and cheap with respect to other mineralogical methods—the instrument measures ‘only’ the top 1 to 100 micrometers. It provides critical insights into regional to mine scale exploration in near real-time. Hyperspectral allows us to observe the distribution of silicate and hydrothermal alteration minerals in the study datasets. Changes in mineralogy at varying depths were observed from 3 drill core and 25 cuttings samples (figures 3.9 and 3.10). This technique also detects and calculates minerals abundances present in the study dataset below 1 %, which seems challenging using other mineral mapping methods. Hyperspectral imaging spectroscopy also allows scanning continuous core sample length and 100 core boxes in a few minutes, while other methods only use a small section of samples for scanning or to be prepared for powder (Nikonow et al., 2019). With this technique, minerals are difficult to miss except for non-spectrally minerals. The spatial relationship between minerals can also be observed in addition to mineral distribution.

Minerals at the edges of the SWIR cuttings samples were chopped off (figure 3.10 and appendix 8) due to the sample holder size being larger than the hyperspectral camera field of view. This was not applied to the LWIR cuttings samples because the LWIR camera field of view was larger to capture the total diameter of the sample holder. Mineral mapping depends on the mapping algorithm and pure endmembers associated with the images to be classified. Endmembers were also used as training samples for the classification. SAM classification was applied to the core, and cuttings processed LWIR and SWIR images. The algorithm is straightforward but requires a predefined threshold by a user to attain a logical result. For the SWIR core and cuttings datasets, spectral bands were subsetted before SAM classification. A threshold value (0.12 radian) and a single spectral library were applied to all SWIR samples. With this threshold value, over 70% of the pixels were unclassified.

Modifying the classification involves using the entire spectral library of 10 endmembers. Similar mineral classes were combined into one class in the post-classification. This reduces unclassified pixels and thereby assigning over 60% of the minerals. The four(4) identified minerals (montmorillonite, muscovite, lepidolite, and ammonio smectite) overlaps at 2206 nm due to their Al-OH composition. This overlap was observed from the XRD analysis. These minerals were distinguished by their proportion of H₂O at 1925nm and hydroxide OH features at 1400nm compared to their 2206nm features. Some minerals have a deep water feature, and others are shallow and broad. For example, montmorillonite has a significantly deeper water feature than smectite (Figure 3.7c), whereas lepidolite exhibits deep water feature than muscovite, but both minerals can be distinguished by their OH features. Muscovite has a shallow but broad OH feature compared to lepidolite with a deep but broad OH feature (figure 3.7a & b). Random inspection of selected pixels shows < 1% misclassification when applying such techniques to the SWIR datasets since the classifier cannot be set to only focus on specific diagnostic features of each endmember to distinguish minerals spectrally. One advantage of the SWIR data is that it contains less noise than LWIR data. However, its major limitation is that most clay minerals' spectral feature potential overlap at 2206nm, making mapping difficult.

LWIR mineral mapping involves using a single threshold value (in this case, 0.12 radians) for all endmembers. This resulted in dominant unclassified pixels and misclassification, resulting in misinterpretation. Dominant unclassified pixels were due to the low threshold value, saturated pixels, and background interference from the cuttings samples holder(figure 4.5). Background spectrum was highly distinct from input endmembers used in the SAM classifier. In addition, misclassified pixels were observed due to minerals endmembers overlapping at varying wavelength positions. For example, sample GMS0508 microcline was classified as albite while quartz and spodumene show some inclusion but in <0.5%. Charoy et al.(2001) also confirm such inclusion from their study on spodumene-petalite-eucryptite mutual relationships and alteration patterns in Li-rich aplite- pegmatite dykes, northern Portugal. Therefore, to match and best fit endmembers using the SAM classifier, appropriate multiple threshold value settings were applied using intermediate rule images in the rule post classification.

Selecting multiple threshold values depended on histogram inspection and, in some cases, by trial and error. This was challenging in selecting the correct threshold values to match a specific mineral endmember. During threshold determination, it was noticed that the process was time-consuming and challenging to determine the accurate threshold for each endmember of the study datasets. As a result, some samples were not fully classified due to the determined threshold values applied. In this study, all LWIR samples used one endmember spectral library and a single set of threshold values. Observation shows that not all pixels were classified. There will always be unclassified pixels that cannot work on a particular threshold value. For example, in LWIR core and cuttings datasets, a threshold of 0.12 radian resulted in most quartz and spodumene pixels being unclassified but using a larger threshold for quartz and spodumene, over 50% of pixels were classified. This observation shows that a smaller threshold leads to most of the minerals being unclassified, thereby missing some information in most samples of the study datasets. A higher threshold solves the issues in minimizing unclassified pixels and produces minimum misclassification in some samples. For example, in a 100cm section of the core labeled as GMS0507, microcline was classified as spodumene but in < 0.5%. It was also observed that less mineral abundance from cuttings samples could be attributed to sample preparation(sieving, washing, and moderate oven-dried). For example, albite and quartz were in low abundance in all cuttings samples. At the same time, spodumene and microcline were mainly concentrated during the sample preparation process.

Manual spectral validation was done by randomly checking individual pixel spectrums and comparing SAM-assigned endmember minerals with the spectra since the classifier cannot be set to only focus on specific diagnostic features of each endmember to distinguish minerals spectrally. This procedure was done for a few samples to show that SAM correctly assigned most of the minerals using the predefined threshold values. However, some pixels were not correctly assigned. Using the rule post classifier, SAM classification was improved by setting a threshold for each mineral endmembers (Table 2.2). However, still, there were a few more pixels unclassified, but over 50% of the mineral were assigned after improvement.

5.4) Comparison and validation by XRD

Hyperspectral LWIR core, cuttings, and XRD analysis provide essential information for quantitative comparison of mineral abundance estimates. The linear correlation coefficient was applied to establish a relationship between both datasets. XRD analytical technique was able to identify minerals that do not have a spectral response and therefore estimates volume percentages of all mineral constituents present in the study dataset, which infrared spectroscopy does not. These validations were made for all minerals similar to both datasets. Quantitative comparison results show a weak positive correlation. After correlation calculation, an unexpected relationship for all minerals with a coefficient of $R^2 < 0.5$ between both techniques was observed, given that one analysis was done on washed and sieved cuttings and the other on unprocessed, milled cuttings. Both techniques were expected to correlate because samples were collected from the same pegmatite host rock and geological settings, which might be attributed to SAM classification results, sample preparation (Sieving and milling), and differences in sample types (powder samples used for XRD and coarse size cuttings samples used for HSI). Mineral proportions of sieved material were less than those of the unsieved material contributing to this poor relationship. SAM classification relies solely on thresholds, making mineral mapping difficult, thus producing low percentage estimates. Preparation of cuttings samples for both XRD and spectroscopy plays a crucial role in the poor relationships between the two techniques. Samples were sieved ($>0.5\text{mm}$) for hyperspectral imaging, reducing the mineral percentage. For example, more albite and quartz were lost in the sieving process. At the same time, microcline and spodumene were concentrated, as evidenced by SAM results (figure 3.19). Contrary to the SAM cuttings result, the mineral proportion from XRD produces contrary results. For example, from the graphical presentation of both data, quartz and albite showed a high mineral proportion. In contrast, microcline and spodumene showed a low proportion. This justified the above-listed factors creating a weak relationship between both techniques. SAM classification results validated by XRD were done in two steps. First, the whole rock analysis on all 100cm cuttings samples confirms minerals detected by SAM-LWIR and SWIR. XRD could not detect some hydrothermal alteration minerals detected by SWIR except for muscovite or lepidolite. Both minerals overlapped at 8.9 2-theta degrees from the generated diffractogram, confirming overlaps from SAM-SWIR results. Additionally, the selected spots from core samples based on SAM classification for spodumene, microcline, and albite were validated by XRD. The results confirmed the presence of minerals in high abundance with minor inclusion of other constituent minerals. These validations have proven the study results to be valid and fact-based.

5.5 Spodumene crystal sizes analysis

LWIR Imaging spectroscopy has proven useful in generating modal mineralogy and enhancing spodumene crystal size surfaces for effective measurement. Modal mineralogy plot revealed quartz as the dominant mineral in a $\sim 4\text{m}$ continuous core sample (figure 3.15). As mentioned in section 2.2.7, measurement of Spodumene crystals considering the long and short axes provides essential information in determining spodumene crystals size in each 10cm interval. The method was useful in estimating spodumene crystals size in each interval by calculating the mean of the three largest crystals used to generate the crystals distribution curve. The method provided significant results similar to the company's criterion regarding core sample intervals as coarse spodumene crystal (P1) and fine spodumene crystal (P2). The correlation summary for modal quartz shows a statistically significant negative relationship with spodumene crystal size, while modal spodumene shows a positive relationship, given the 95% confidence level applied. There was no statistically significant positive or negative relationship between albite and microcline at any reasonable uncertainty level. Visual inspection of sample images shows that zones of dominant quartz and albite contain mainly 'P1' materials, while zones of dominant quartz and microcline contain dominant 'P2' materials.

These observations were also confirmed by Černý and Ercit (2005). According to Černý and Ercit, albite-spodumene pegmatite is characterized by dominance quartz and albite over K-feldspar, which produces bulk pegmatite Li concentrations around 2 wt% Li_2O . In addition, an attempt was made to link SAM-LWIR core (unsieved and unwashed) and cuttings (sieved and washed) mineralogy. For this purpose, the abundance of each core sample at exactly the same depth was linearly correlated with SAM-LWIR core and SAM-LWIR and XRD cuttings samples, thus constituting a relatively simple proxy for both datasets. The results revealed no statistically significant positive or negative relationships between SAM-LWIR core and SAM-LWIR and XRD cuttings for modal albite, microcline, quartz, and spodumene at a 95% confidence level. These non-significance results could be attributed to samples not precisely aligning within the twin drill holes, as shown in the graphical representation (Figure 3.19 A and B, C and D).

Moreover, the non-significance results could be linked to limited statistical data, sample preparation (sieved and washed), and, in some cases, the classification results. SAM-LWIR core and cuttings were plotted on a one-to-one relationship line to confirm the effect of sample preparation (figure 3.18 A, B, C). The relationship shows that albite and quartz were lost during the sieving and washing, thus contributing to the low abundance from SAM classification. At the same time, spodumene and microcline were mainly concentrated and later imaged, thus confirming the high abundances of both minerals. On the contrary, SAM-LWIR cuttings and XRD cuttings were plotted on a one-to-one relationship line (figure 3.18 D, E, F). The results further validated the effect of sample preparation in that unsieved, unwashed XRD samples resulted in a high abundance of albite and quartz. This confirms that sample preparation has contributed to the low abundance of albite and quartz from SAM classification. Even though the classification method has its limitation in fully mapping all pixels in the image, it still proves ideal in mapping spodumene and its constituents minerals in core and cuttings. It can later be used on mine sites, provided hyperspectral drill core scanning is available to support the geologist in the core-logging procedure. The derived modal mineralogy can prove useful at every exploration stage as they are essential in defining geometallurgical domains (P1 and P2).

SWIR imaging spectroscopy works well in mapping hydrothermal minerals that could be used as accessory minerals in discriminating coarse spodumene crystals size (P1) and fine spodumene crystals (P2) pegmatite in drill core and cuttings based on advanced data integration methods. For example, muscovite, one primary constituent mineral in most pegmatite detected by SWIR could be used as an accessory mineral for discriminating both material types ('P1' and 'P2'). Furthermore, montmorillonite and ammonio smectite could also substitute for albite and microcline. LWIR and SWIR imaging spectroscopy can complement each other. For example, pixels classified as microcline in the LWIR data were also mapped as ammonio smectite from the same pixels in the SWIR, thus adding additional information.

6. CONCLUSION AND RECOMMENDATIONS

6.1 Conclusion

The primary objective of this study was to characterize and discriminate coarse-spodumene and fine spodumene crystal pegmatite applied to drill core based on mineralogy as a proxy for cuttings samples using LWIR and SWIR imaging spectroscopy. Results and discussion of spectroscopy study together with XRD and crystal size analysis on drill core and cuttings of the Berriman supergroup sequences resulted in the following conclusions:

- Hyperspectral LWIR imaging spectroscopy has proven its potential as a powerful tool for producing mineralogical maps of drill core and cuttings samples. HSI can identify minerals even at a low percentage of < 1%. Mineral identification and characterization use Spectral Angle Mapper (SAM) classification, which tries to match and fit the entire spectra. SAM results strongly depend on the threshold settings of each inputted endmembers. SAM algorithm has demonstrated its usefulness in mapping over 50% of the identified minerals. The most common minerals detected from the LWIR drill core and cuttings include Albite, quartz, microcline, and spodumene. Similarly, Muscovite, ammonio smectite, montmorillonite, and lepidolite were the most common hydrothermal alteration minerals detected from SWIR drill core and cuttings. SAM algorithm also generates mineral abundance estimates used to calculate the modal mineralogy. Therefore, this approach can be used as a standard core-logging procedure to complement conventional on-site logging by geologists and serve as a background for metallurgical analysis.
- Spodumene spectral signature identified from LWIR range has a broad feature covering the wavelength range at 8322 nm, 9086 nm, and 10506 nm, which can easily be distinguished from other lithium-bearing minerals such as lepidolite. These two lithium-bearing minerals (lepidolite and spodumene) are highly distinguishable due to both minerals being detected from two different wavelength ranges. Given its broad features, spodumene was observed to be extensively overlapped with other associated minerals. XRD analytical method has proven its potential in validating spectroscopy results. XRD confirmed all minerals detected from LWIR and SWIR core and cuttings except for montmorillonite and smectite, which XRD did not detect. This might be some limitation of the technique in detecting hydrothermal minerals.
- Spodumene crystal size analysis on ~4m continuous core sample shows variation in spodumene crystal size at varying depths. Based on a predefined threshold, If the mean of the three largest spodumene crystals size in a 10 cm interval was $\geq 100 \text{ mm}^2$, the interval was described as a coarse spodumene crystal interval (P1); otherwise, the interval was deemed fine-crystal (P2). The study results show that the top section of ~4m continuous core corresponding to depth intervals from 65.9 to 67.4 m was mainly described as **'P2'**. The middle section contains dominant 'P1' $>150\text{mm}^2$ from depth intervals 67.5 to 69.1 m, with some 'P2' mixed at a depth ranging from 67.8 to 68.7. The lower section of the core from depth intervals 69.2 to 69.9 were mainly described as 'P2' with crystals size $<100\text{mm}^2$. The end of the cored section with depth intervals of 69.6 to 70.3 meters was mainly classified as **'P1'** with crystals size $< 100\text{mm}^2$. Given the methodology and threshold applied, the study results were similar to what the company's experienced employee determined, who visually described the cored sections without fancy technology.

Modal mineralogy of spodumene, albite, microcline, and quartz was plotted and correlated with the mean spodumene crystals size data. The result revealed no statistically significant positive or negative relationship between spodumene crystal size and modal mineralogy of albite and microcline. Modal spodumene shows a statistically significant positive relationship with spodumene crystal size; Modal quartz revealed a statistically significant negative relationship with both P-values $< \alpha$ (alpha = 0.05). Visual inspection of classified images and physical core for confirmation revealed that zones of dominant quartz and albite were associated with coarse spodumene crystals size '**P1**', and zones of dominant quartz and microcline were related to fine spodumene crystal sizes '**P2**', confirming Cerny's information. Based on the above results, modal quartz and spodumene could be used as a proxy for spodumene crystal size (**P1 and P2**), considering their statistical significance. The non-statistical significant relationship between core and cuttings mineralogy at exactly the same depth interval, which could serve as a simple proxy, shows non statistically significant due to low data values and samples not precisely aligning within the twin drill holes. The above methodology applied for spodumene crystal size analysis is repeatable and can be applied to other datasets.

6.2 Recommendations

The following are recommended based on the results:

- Limited core and cuttings samples at precisely the same depth make comparison scanty. For this reason, it is recommended that additional core and cuttings samples at precisely the same depth intervals be provided to increase confidence level for future work.
- It was observed that sample preparation of cuttings for imaging resulted in a mineral loss. Therefore, coarse size fraction of cuttings samples is highly recommended. This will eliminate sample preparation and solve the issue of mineral loss.
- Spectral angle mapper was extensively used to map minerals in the study dataset. However, not all mineral species were mapped using SAM. Selecting the appropriate threshold to map all mineral species was challenging and almost tricky. Therefore, an optimal knowledge-based classification approach, such as a decision- tree is highly recommended for future works.
- Spodumene crystal size measurements were done manually by selecting the three largest crystal sizes within a 10cm interval on a 100cm print-out core section. The results show crystal variation in the core pretty well. However, an automated technique such as machine learning is recommended for better improvement in measuring all the crystals in the samples to improve correlation results.
- Hyperspectral core mineralogy as a proxy for cuttings samples requires other analytical methods to increase the confidence level of the validation method. For this purpose, analytical techniques are recommended for future work, including ICP- MS or ICP – OES spectrometry(minor or trace element); Additionally, petrography, and micro-XRF analysis.

LIST OF REFERENCES

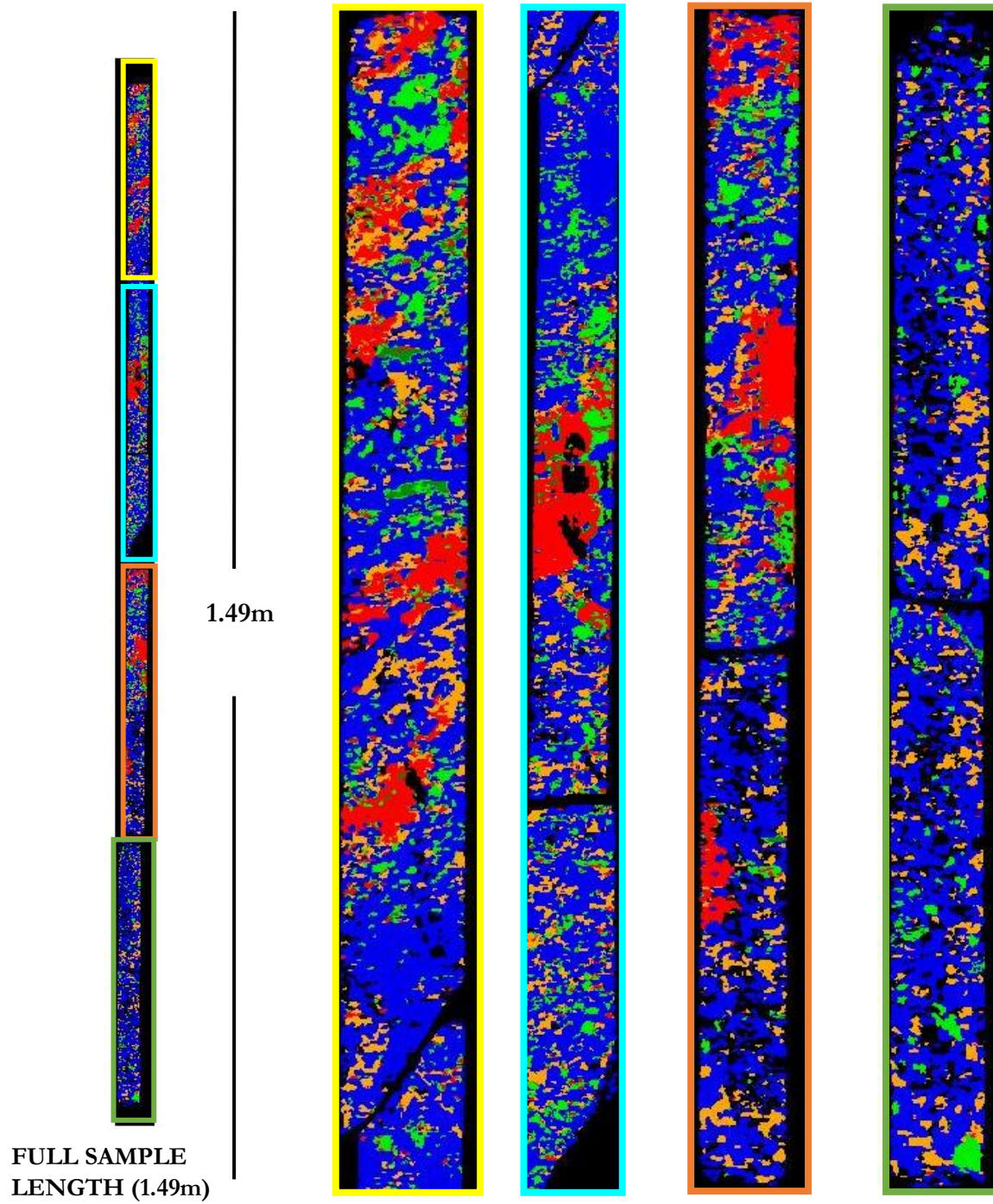
- Aylmore, M.G., Merigot, K., Rickard, W.D.A., Evans, N.J., McDonald, B.J., Catovic, E., Spitalny, P., 2018. Assessment of a spodumene ore by advanced analytical and mass spectrometry techniques to determine its amenability to processing for the extraction of lithium. *Minerals Engineering* 119, 137–148. <https://doi.org/10.1016/j.mineng.2018.01.010>
- Cao, Z., Ren, Y., Wang, Q., Yao, B., Zhang, X., 2021. Evolution Mechanism of Water-Conducting Channel of Collapse Column in Karst Mining Area of Southwest China. *Geofluids* 2021. <https://doi.org/10.1155/2021/6630462>
- Černý, P., Černý, Č., 2005. The classification of granitic pegmatites revisited. *The Canadian Mineralogist* 43, 2005–2026.
- Charoy, B., Noronha, F., Lima, A., 2001. Spodumene - petalite - eucryptite: Mutual relationships and pattern of alteration in Li-rich aplite-pegmatite dykes from Northern Portugal. *Canadian Mineralogist* 39, 729–746. <https://doi.org/10.2113/gscanmin.39.3.729>
- Chen, T., Jin, Y., Lv, H., Yang, A., Liu, M., Chen, B., Xie, Y., Chen, Q., 2020. Applications of Lithium-Ion Batteries in Grid-Scale Energy Storage Systems. *Transactions of Tianjin University* 26, 208–217. <https://doi.org/10.1007/S12209-020-00236-W>
- Clark, R.N., 1999. USGS Spectroscopy Lab: Spectroscopy of Rocks and Minerals, and Principles of Spectroscopy. *Spectroscopy of Rocks and Minerals, and Principles of Spectroscopy*.
- Clark, R.N., King, T.V.V., Klejwa, M., Swayze, G.A., Vergo, N., 1990. High spectral resolution reflectance spectroscopy of minerals. *Journal of Geophysical Research* 95. <https://doi.org/10.1029/JB095IB08P12653>
- Dennison, P.E., Halligan, K.Q., Roberts, D.A., 2004. A comparison of error metrics and constraints for multiple endmember spectral mixture analysis and spectral angle mapper. *Remote Sensing of Environment* 93, 359–367. <https://doi.org/10.1016/J.RSE.2004.07.013>
- Dzighbodi-Adjimah, K., 1993. Geology and geochemical patterns of the Birimian gold deposits, Ghana, West Africa. *Journal of Geochemical Exploration* 47, 305–320. [https://doi.org/10.1016/0375-6742\(93\)90073-U](https://doi.org/10.1016/0375-6742(93)90073-U)
- Greenberger, R.N., Ehlmann, B.L., Blaney, D.L., Cloutis, E.A., Wilson, J.H., Fraeman, A.A., 2015. Imaging spectroscopy of geological samples and outcrops: Novel insights from microns to meters. *GSA Today* 25. <https://doi.org/10.1130/GSATG252A.1>
- Greim, P., Solomon, A.A., Breyer, C., 2020. Assessment of lithium criticality in the global energy transition and addressing policy gaps in transportation 1–2. <https://doi.org/10.1038/s41467-020-18402-y>
- Grosjean, C., Herrera Miranda, P., Perrin, M., Poggi, P., 2012. Assessment of world lithium resources and consequences of their geographic distribution on the expected development of the electric vehicle industry. *Renewable and Sustainable Energy Reviews*. <https://doi.org/10.1016/j.rser.2011.11.023>
- Hecker, C., der Meijde, M. van, van der Meer, F.D., 2010. Thermal infrared spectroscopy on feldspars — Successes, limitations and their implications for remote sensing. *Earth-Science Reviews* 103, 60–70. <https://doi.org/10.1016/J.EARSCIREV.2010.07.005>
- Hecker, C., van Ruitenbeek, F.J.A., Bakker, W.H., Fagbohun, B.J., Riley, D., van der Werff, H.M.A., van der Meer, F.D., 2019. Mapping the wavelength position of mineral features in hyperspectral thermal infrared data. *International Journal of Applied Earth Observation and Geoinformation* 79, 133–140. <https://doi.org/10.1016/j.jag.2019.02.013>
- Herzog, T., Pershing, J., Baumert, K.A., 2005. Navigating the Numbers: Greenhouse Gas Data and International Climate Policy, World Resources Institute.
- Hirdes, W., Davis, D.W., Eisenlohr, B.N., 1992. Reassessment of Proterozoic granitoid ages in Ghana on the basis of U/Pb zircon and monazite dating. *Precambrian Research* 56, 89–96. [https://doi.org/10.1016/0301-9268\(92\)90085-3](https://doi.org/10.1016/0301-9268(92)90085-3)

- IronRidge Resources, 2021. Exceptional Lithium Scoping Study Results, Ghana - 07:00:04 19 Jan 2021 - IRR News article | London Stock Exchange [WWW Document]. URL <https://www.londonstockexchange.com/news-article/IRR/exceptional-lithium-scoping-study-results-ghana/14831473?lang=en> (accessed 4.28.21).
- Jacq, K., Giguët-Covex, C., Sabatier, P., Perrette, Y., Fanget, B., Coquin, D., Debret, M., Arnaud, F., 2019. High-resolution grain size distribution of sediment core with hyperspectral imaging. *Sedimentary Geology* 393–394, 105536. <https://doi.org/10.1016/J.SEDGEO.2019.105536>
- Kesse, G.O. (Godfried O., 1985. The mineral and rock resources of Ghana. A.A. Balkema ;;Distributed in USA & Canada by A.A. Balkema Publishers, Rotterdam ;;Boston ;Accord MA.
- Kraal, K.O., Ayling, B., 2019. Hyperspectral Characterization of Fallon FORGE Well 21-31: New Data and Technology Applications. *Proceedings, 44th Workshop on Geothermal Reservoir Engineering* 1–15.
- Kruse, F.A., Lefkoff, A.B., Boardman, J.W., Heidebrecht, K.B., Shapiro, A.T., Barloon, P.J., Goetz, A.F.H., 1993. The spectral image processing system (SIPS)-interactive visualization and analysis of imaging spectrometer data. *Remote Sensing of Environment* 44, 145–163. [https://doi.org/10.1016/0034-4257\(93\)90013-N](https://doi.org/10.1016/0034-4257(93)90013-N)
- Leube, A., Hirdes, W., Mauer, R., Kesse, G.O., 1990. The early Proterozoic Birimian Supergroup of Ghana and some aspects of its associated gold mineralization. *Precambrian Research* 46, 139–165. [https://doi.org/DOI:10.1016/0301-9268\(90\)90070-7](https://doi.org/DOI:10.1016/0301-9268(90)90070-7)
- Luo, G., Chen, G., Tian, L., Qin, K., Qian, S.E., 2016. Minimum Noise Fraction versus Principal Component Analysis as a Preprocessing Step for Hyperspectral Imagery Denoising. *Canadian Journal of Remote Sensing* 42, 106–116. <https://doi.org/10.1080/07038992.2016.1160772>
- Menendez, J., Torano, M.G., 2004. (10) (PDF) Optimisation of spodumene flotation [WWW Document]. URL https://www.researchgate.net/publication/268058316_Optimisation_of_spodumene_flotation (accessed 6.13.22).
- Menéndez, M., Vidal, A., Toraño, J., Gent, M., 1303. Optimisation of spodumene flotation. *The European Journal of Mineral Processing and Environmental Protection* 4, 130–135.
- Morgan, S., 2015. Mining Sector Recovery to Benefit Suppliers | Morgan Stanley [WWW Document]. URL <https://www.morganstanley.com/ideas/commodities-mining-capex-to-benefit-suppliers> (accessed 6.13.22).
- Nikonow, W., Rammlmair, D., Meima, J.A., Schodlok, M.C., 2019. Advanced mineral characterization and petrographic analysis by μ -EDXRF, LIBS, HSI and hyperspectral data merging. *Mineralogy and Petrology* 417–431. <https://doi.org/10.1007/s00710-019-00657-z>
- Perrouy, S., Aillères, L., Jessell, M.W., Baratoux, L., Bourassa, Y., Crawford, B., 2012. Revised Eburnean geodynamic evolution of the gold-rich southern Ashanti Belt, Ghana, with new field and geophysical evidence of pre-Tarkwaian deformations. *Precambrian Research* 204–205, 12–39. <https://doi.org/10.1016/J.PRECAMRES.2012.01.003>
- Portela, B., Sepp, M.D., van Ruitenbeek, F.J.A., Hecker, C., Dilles, J.H., 2021. Using hyperspectral imagery for identification of pyrophyllite-muscovite intergrowths and alunite in the shallow epithermal environment of the Yerington porphyry copper district. *Ore Geology Reviews* 131, 104012. <https://doi.org/10.1016/j.oregeorev.2021.104012>
- Salisbury, J.W., D’Aria, D.M., Jarosewich, E., 1991. Midinfrared (2.5–13.5 μ m) reflectance spectra of powdered stony meteorites. *Icarus* 92, 280–297. [https://doi.org/10.1016/0019-1035\(91\)90052-U](https://doi.org/10.1016/0019-1035(91)90052-U)
- Savitri, Kartika P., Hecker, C., van der Meer, F.D., Sidik, R.P., 2021. VNIR-SWIR infrared (imaging) spectroscopy for geothermal exploration: Current status and future directions. *Geothermics* 96, 102178. <https://doi.org/10.1016/J.GEOTHERMICS.2021.102178>
- Selway, J.B., Breaks, F.W., Tindle, A.G., 2005. A review of rare-element (Li-Cs-Ta) pegmatite exploration techniques for the superior province, Canada, and large worldwide tantalum deposits. *Exploration and Mining Geology* 14, 1–30. <https://doi.org/10.2113/gsemg.14.1-4.1>
- Tadesse, B., Makuei, F., Albijanic, B., Dyer, L., 2019. The beneficiation of lithium minerals from hard rock ores: A review. *Minerals Engineering* 131, 170–184. <https://doi.org/10.1016/j.mineng.2018.11.023>
- van der Meer, F.D., van der Werff, H.M.A., van Ruitenbeek, F.J.A., Hecker, C.A., Bakker, W.H., Noomen, M.F., van der Meijde, M., Carranza, E.J.M., de Smeth, J.B., Woldai, T., 2012. Multi- and hyperspectral

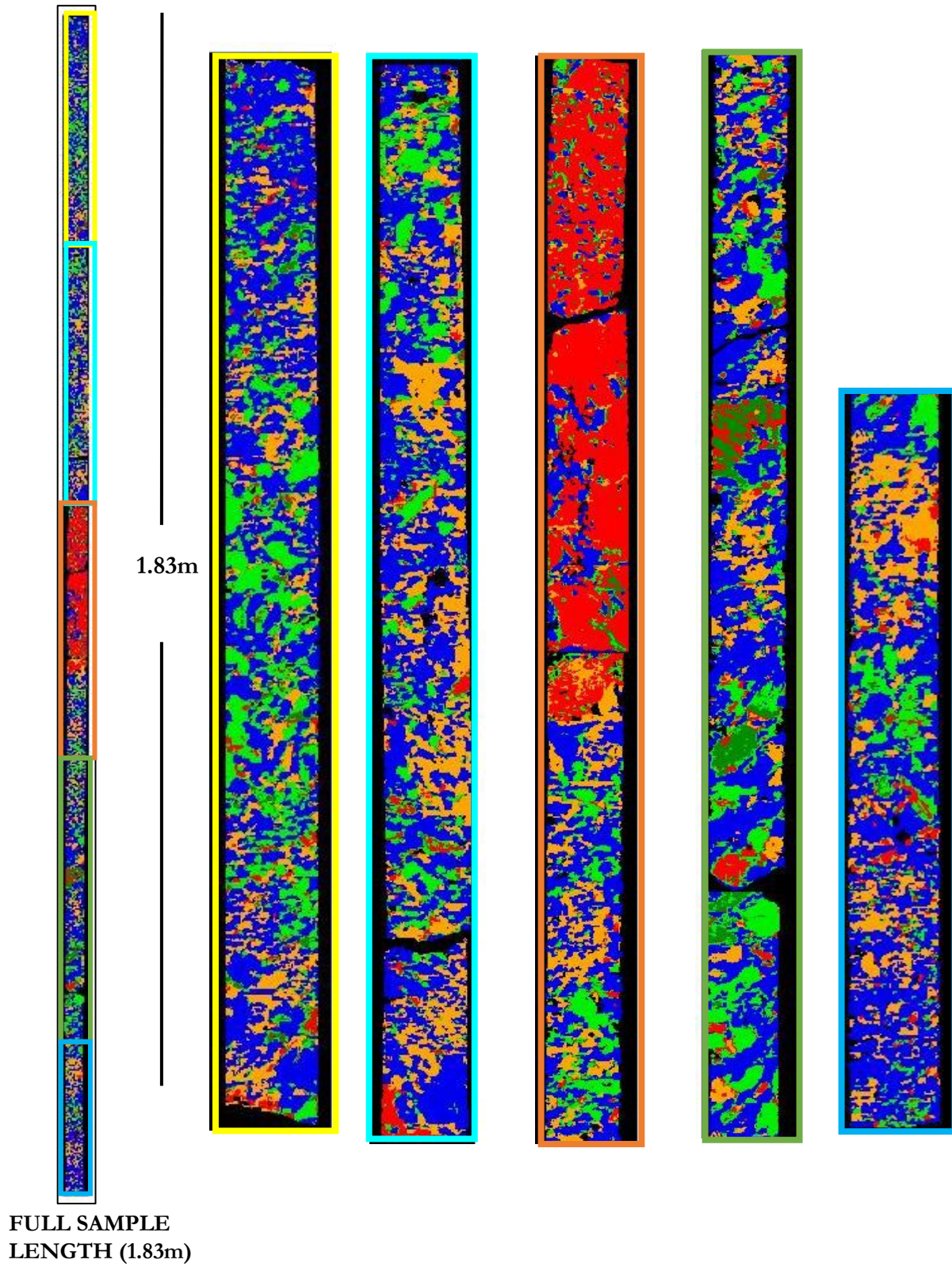
- geologic remote sensing: A review. *International Journal of Applied Earth Observation and Geoinformation* 14, 112–128. <https://doi.org/10.1016/J.JAG.2011.08.002>
- Vieceli, N., Nogueira, C.A., Pereira, M.F.C., Durão, F.O., Guimarães, C., Margarido, F., 2017. Optimization of Lithium Extraction from Lepidolite by Roasting Using Sodium and Calcium Sulfates. *Mineral Processing and Extractive Metallurgy Review* 38, 62–72. <https://doi.org/10.1080/08827508.2016.1262858>
- Yuen, P.W.T., Richardson, M., 2010. An introduction to hyperspectral imaging and its application for security, surveillance and target acquisition. *Imaging Science Journal* 58, 241–253. <https://doi.org/10.1179/174313110X12771950995716>

APPENDICES

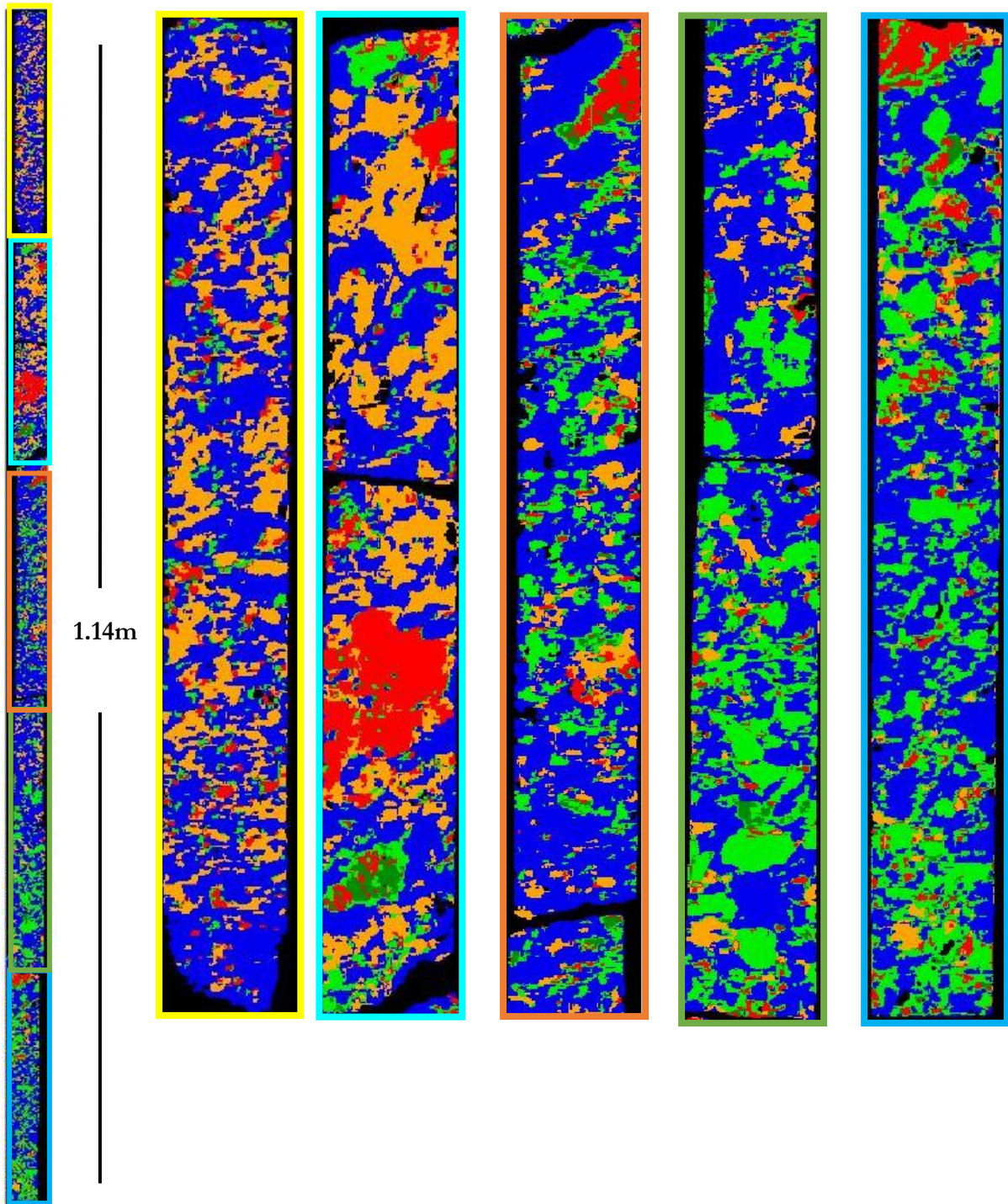
Appendix 1: Hyperspectral classified SAM-LWIR core images of 100cm core section (GMS0507)



Appendix 2: Hyperspectral classified SAM-LWIR core images of 100cm core section (GMS0508)

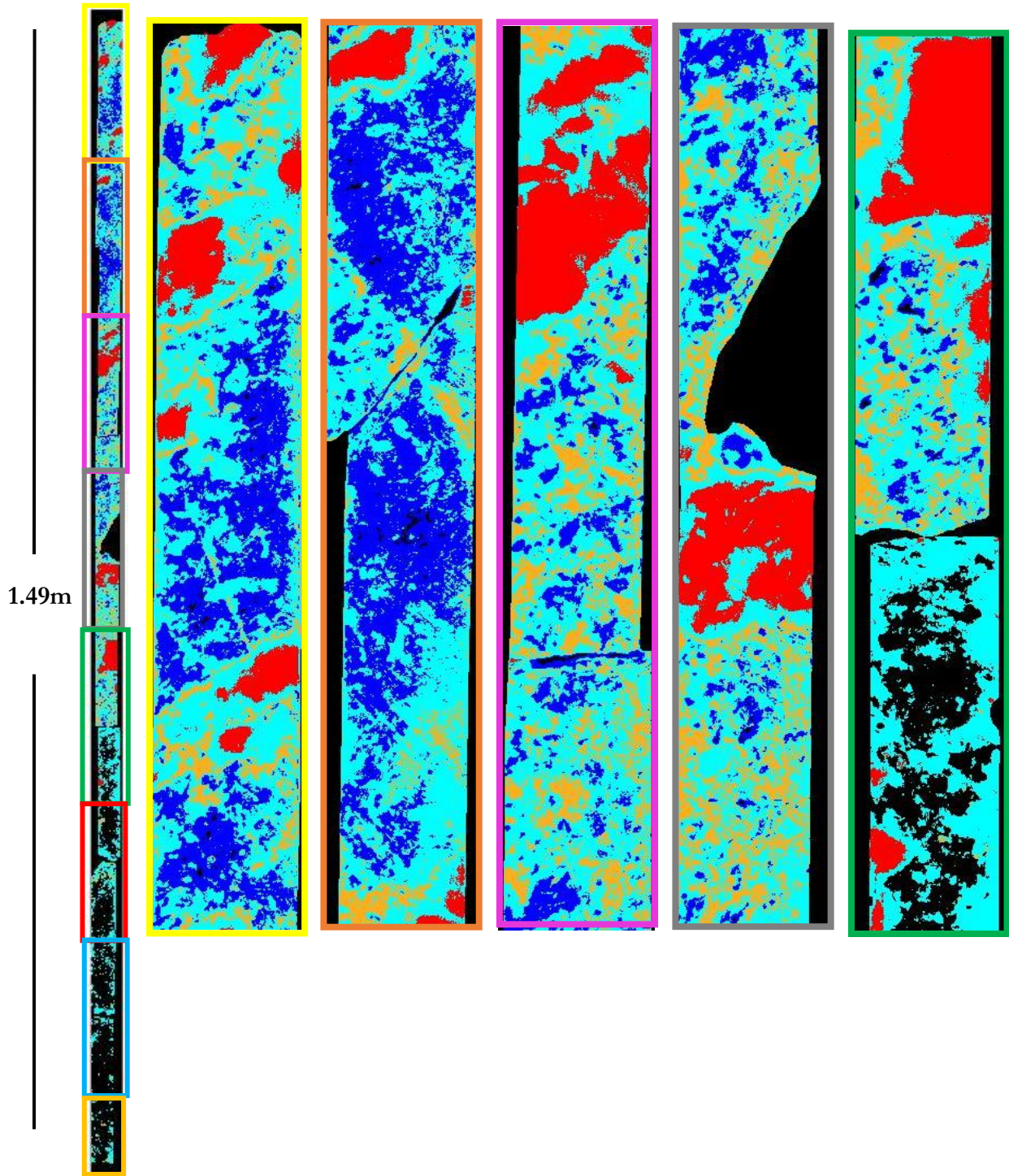


Appendix 3: Hyperspectral classified SAM-LWIR core images of 100cm core section (GMS0509)



FULL SAMPLE
LENGTH (1.14 m)

Appendix 4: Hyperspectral classified SAM-SWIR core images of 100cm core section (GMS0507)

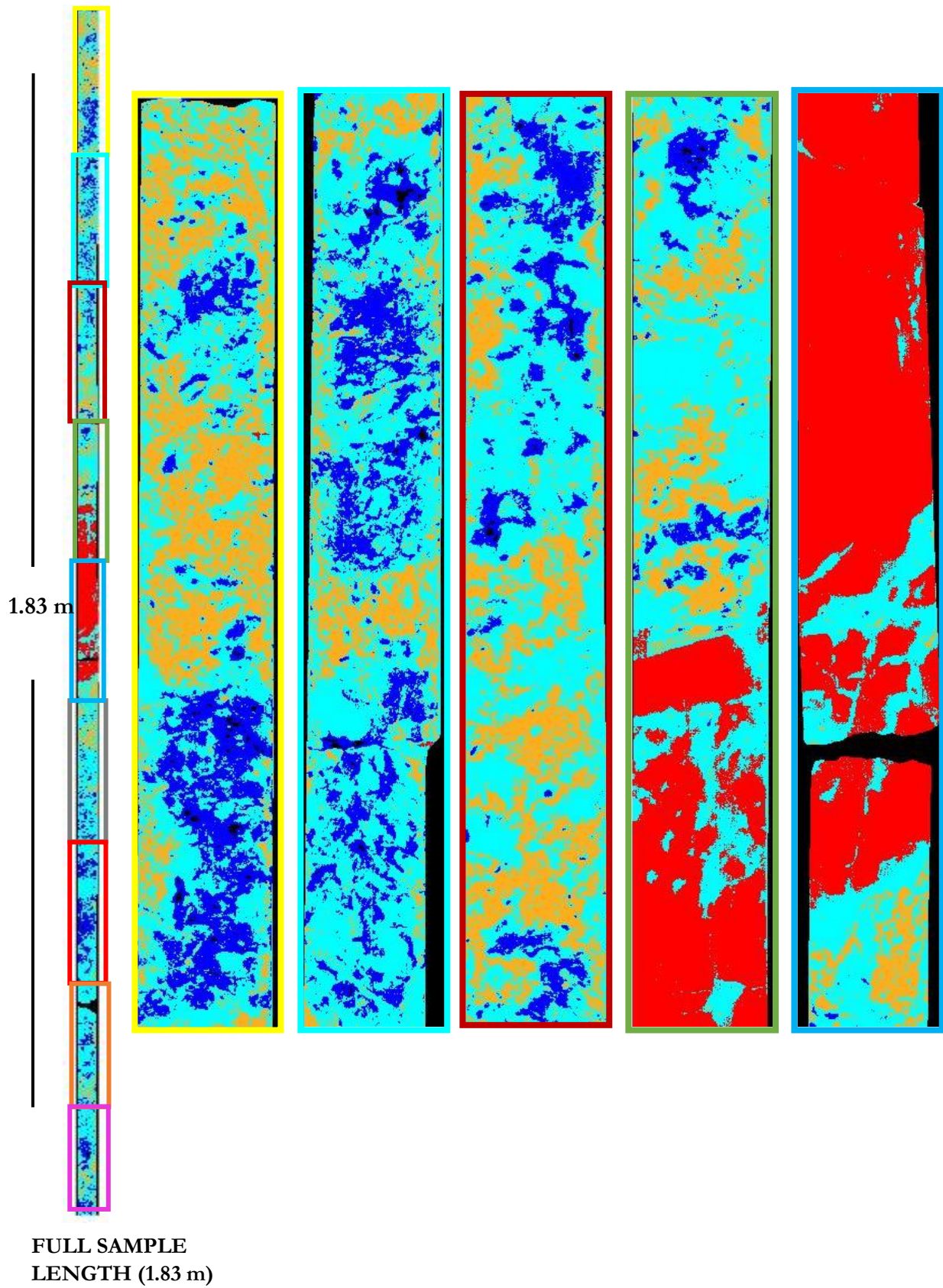


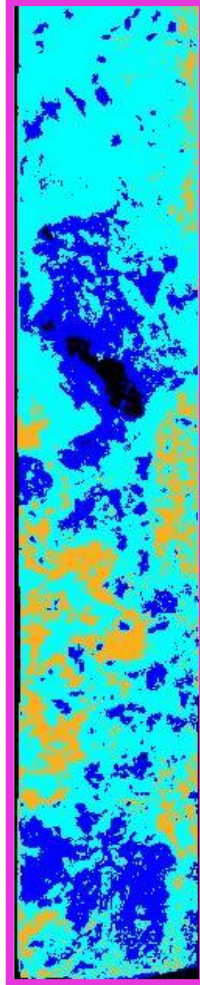
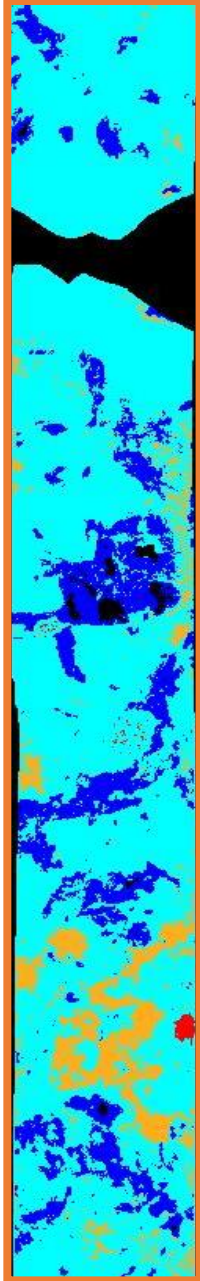
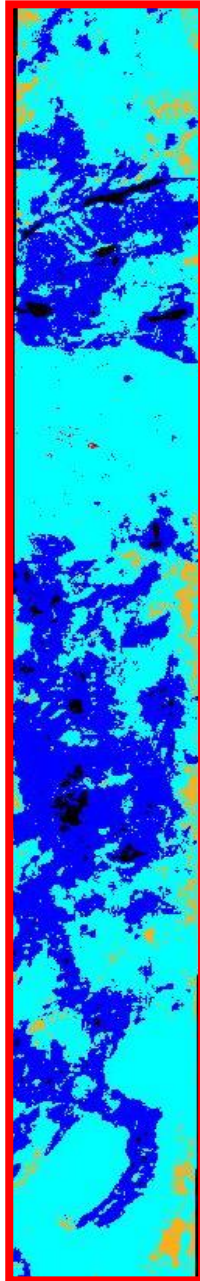
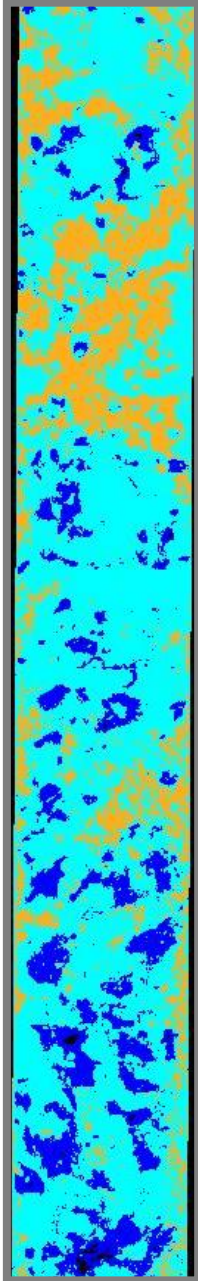
1.49m

FULL SAMPLE
LENGTH (1.49 m)

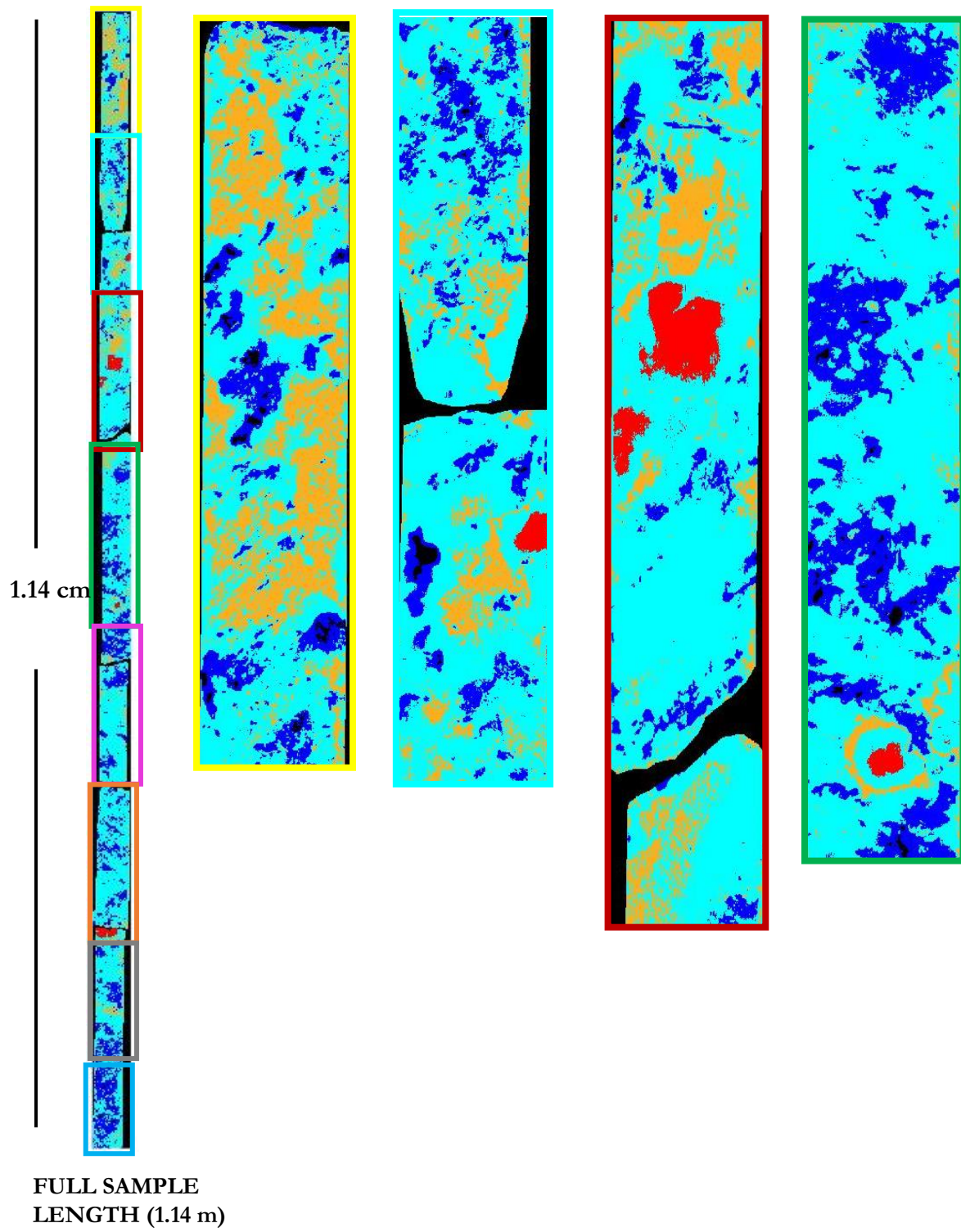


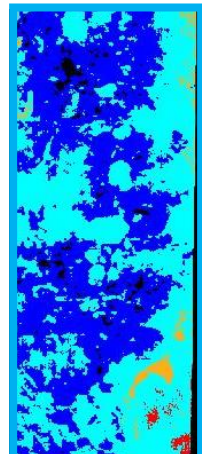
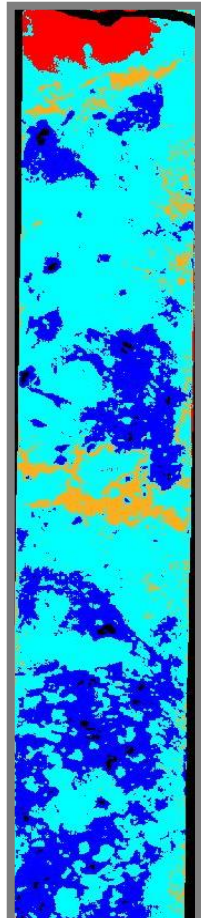
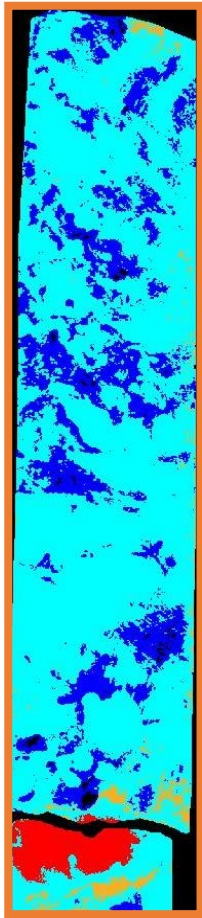
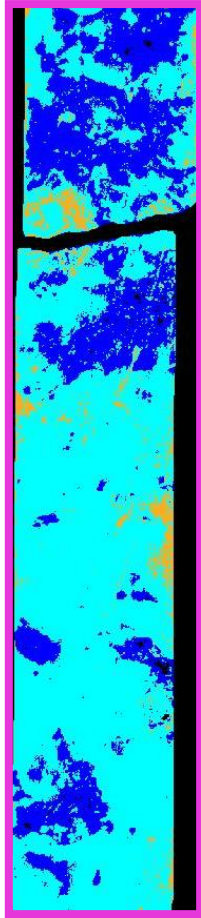
Appendix 5: Hyperspectral classified SAM-SWIR core images of 100cm core section (GMS0508)



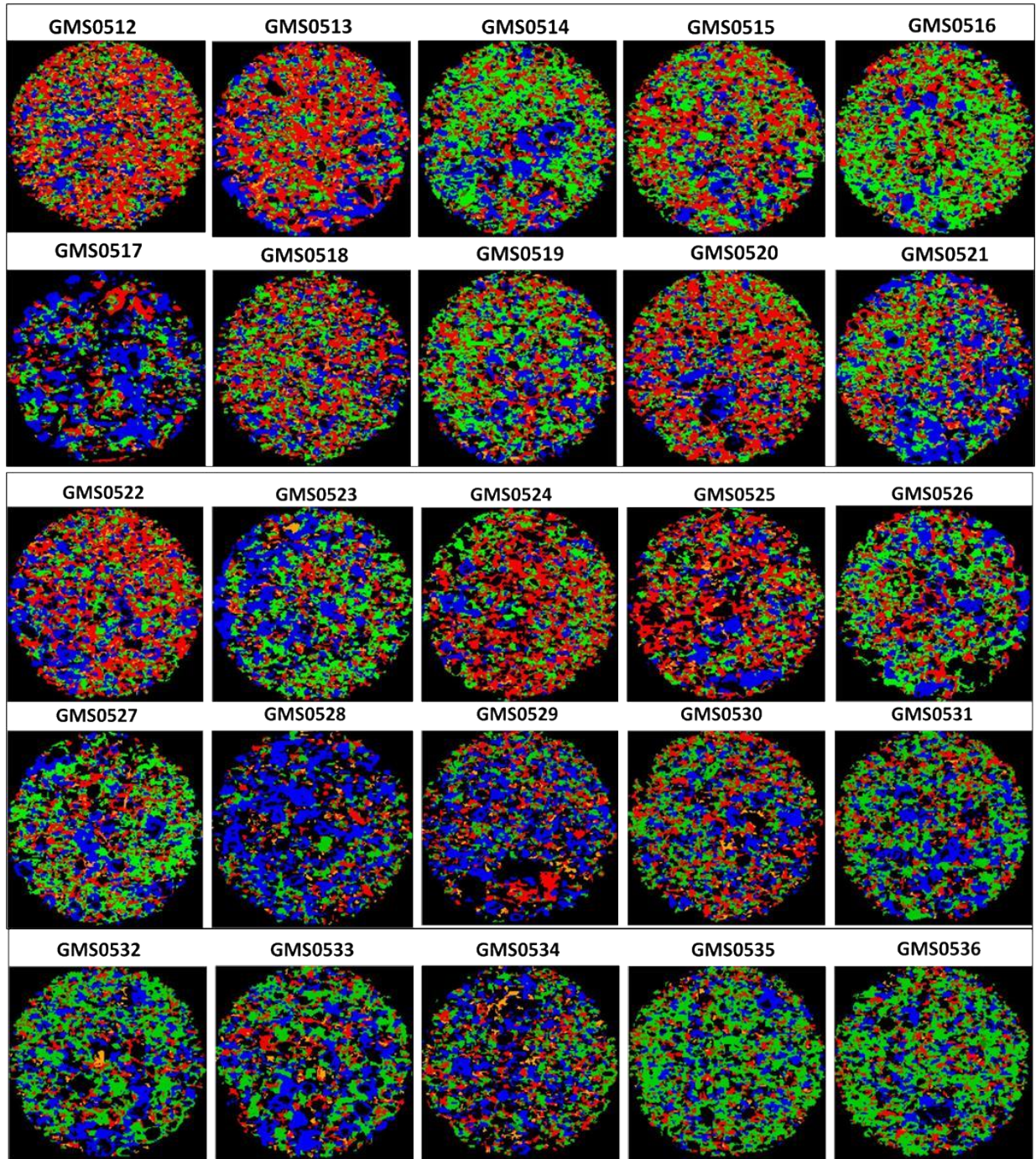


Appendix 6: Hyperspectral classified SAM-SWIR core images of 100cm core section (GMS0509)

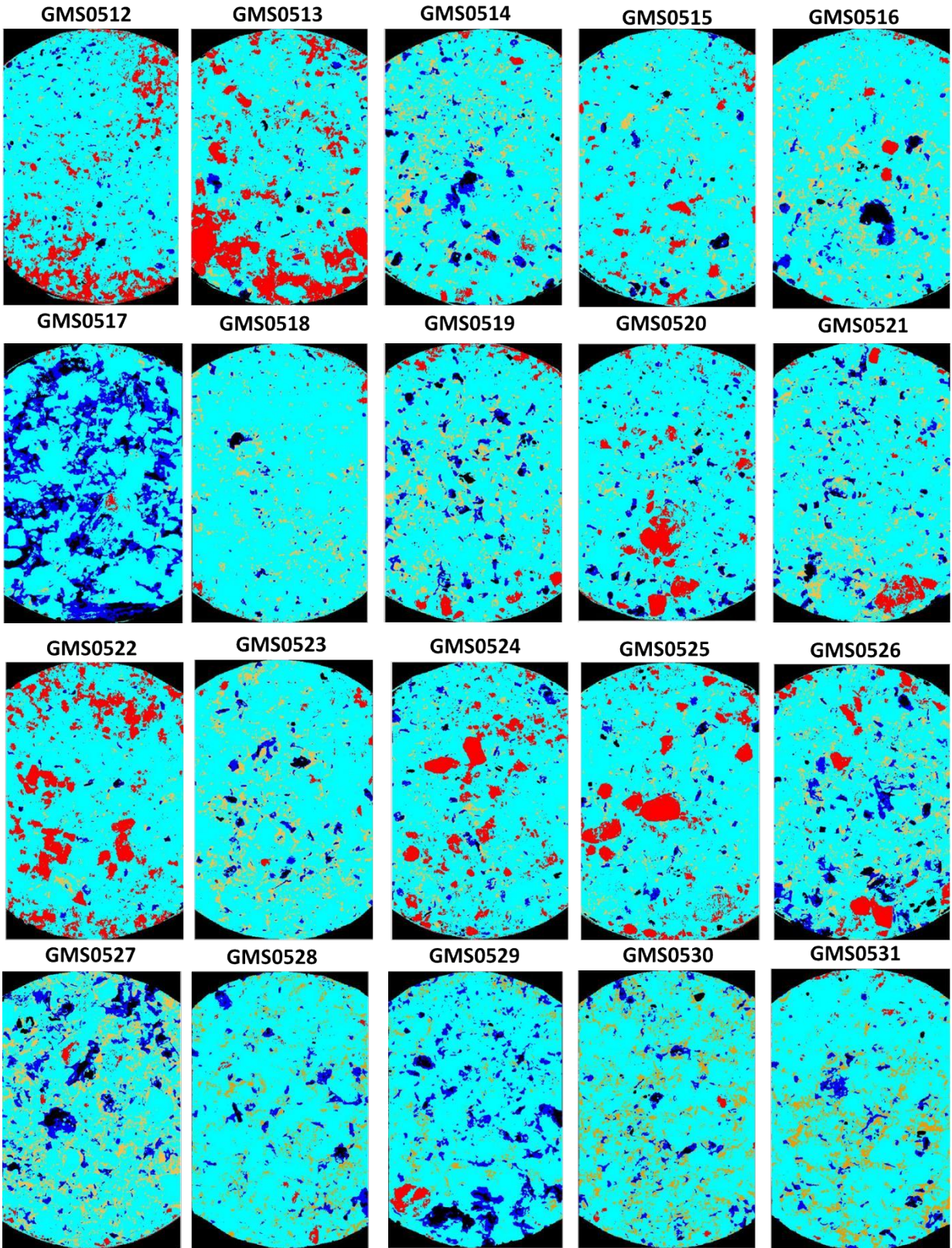




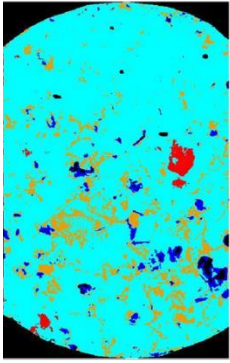
Appendix 7: Twenty-five classified SAM- LWIR cuttings images



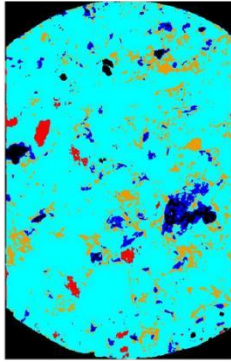
Appendix 8: Twenty-five classified SAM- SWIR cuttings images.



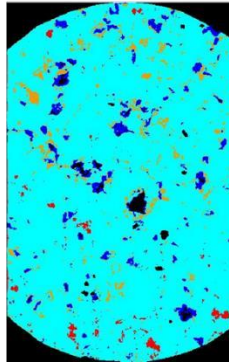
GMS0532



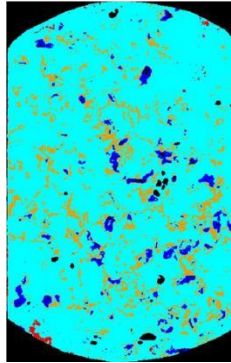
GMS0533



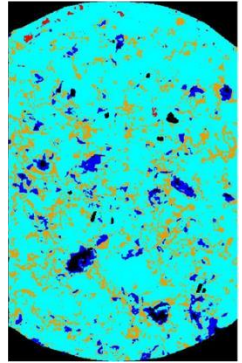
GMS0534



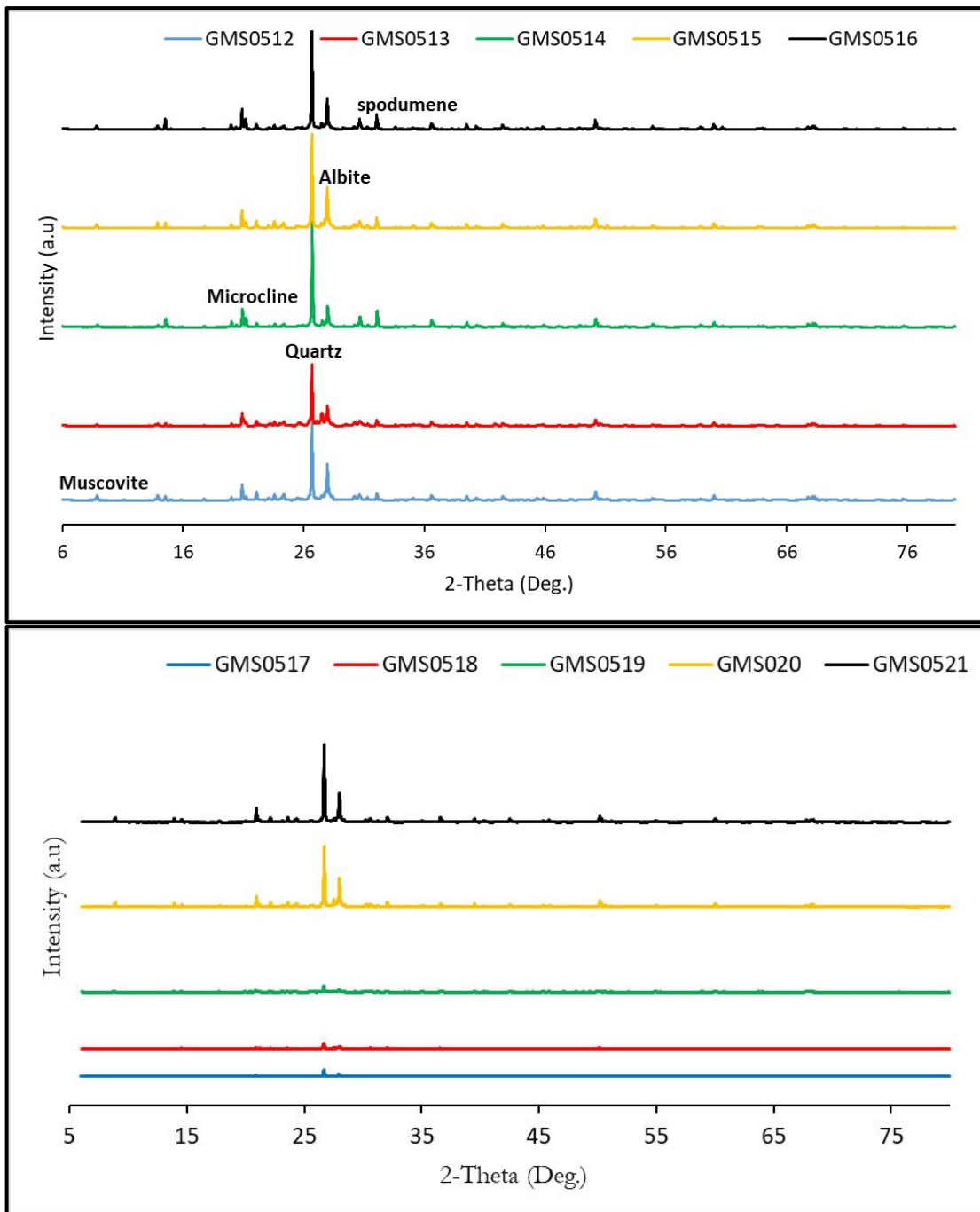
GMS0535

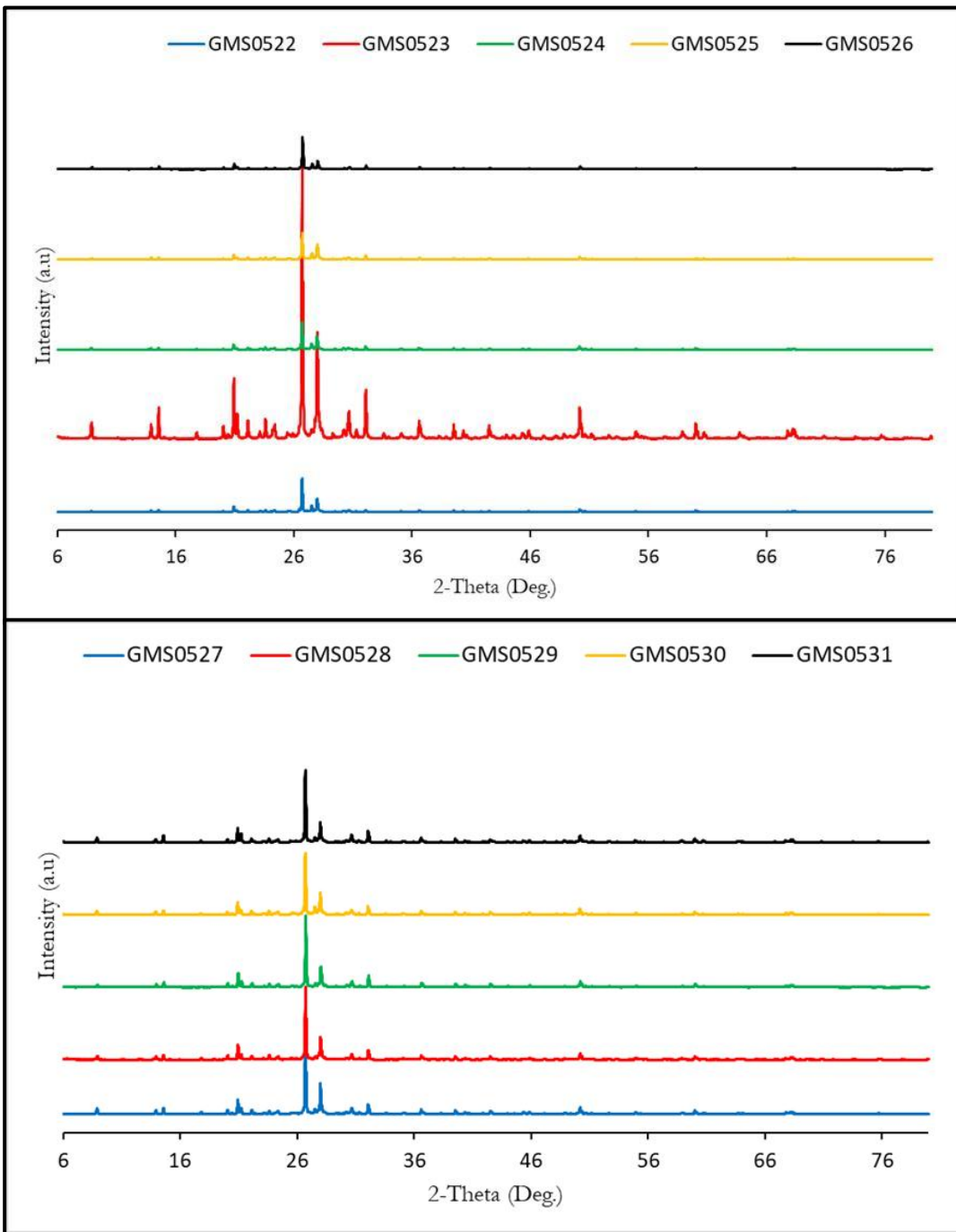


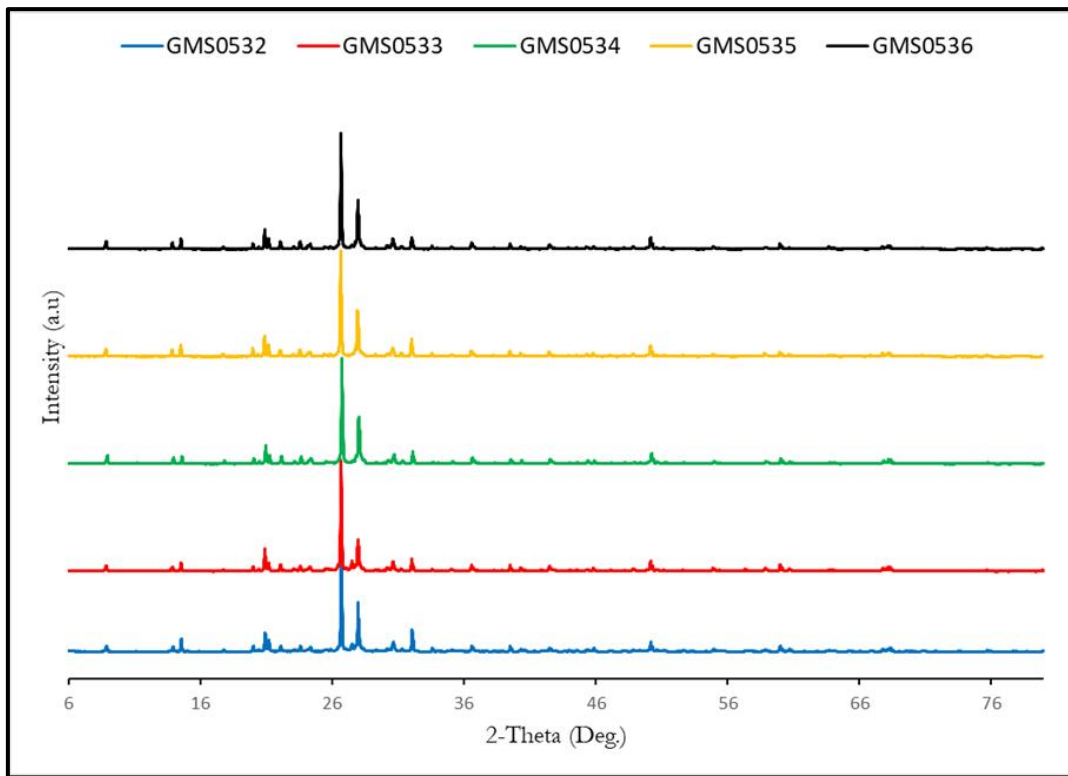
GMS0536



Appendix 9: Twenty-five XRD diffractogram cuttings samples(unsieved and unwashed)







Appendix 10: Modal mineralogy proportion database of quartz, microcline, albite, and spodumene

Sample id	Depth_from	Depth_To	Quartz	Microcline	Albite	Spodumene
GMS0507	65.9	66	44.9	21.2	14.7	19.3
GMS0507	66	66.1	59.4	15.3	14.9	10.4
GMS0507	66.1	66.2	71.7	9.4	10.6	8.3
GMS0507	66.2	66.3	62.4	11.7	5.1	20.9
GMS0507	66.3	66.4	49.0	27.5	11.1	12.4
GMS0507	66.4	66.5	67.5	3.6	16.0	12.9
GMS0507	66.5	66.6	52.5	21.8	8.8	16.8
GMS0507	66.6	66.7	50.8	25.3	10.8	13.1
GMS0507	66.7	66.8	68.1	8.5	13.3	10.2
GMS0507	66.8	66.9	69.0	7.1	21.0	3.0
GMS0507	66.9	67	79.9	1.2	11.5	7.4
GMS0507	67	67.1	73.1	1.1	18.8	7.1
GMS0507	67.1	67.2	77.4	0.4	14.5	7.7
GMS0507	67.2	67.3	71.6	0.7	17.7	10.0
GMS0508	67.3	67.4	71.9	5.9	6.3	16.0
GMS0508	67.4	67.5	64.2	4.8	12.6	18.5
GMS0508	67.5	67.6	51.0	3.7	17.3	28.1
GMS0508	67.6	67.7	44.2	5.1	10.3	40.3
GMS0508	67.7	67.8	47.6	5.6	21.7	25.1
GMS0508	67.8	67.9	47.4	7.0	19.7	26.0
GMS0508	67.9	68	52.0	2.8	25.3	19.9
GMS0508	68	68.1	54.0	3.5	27.5	14.9
GMS0508	68.1	68.2	48.3	4.8	33.9	13.0
GMS0508	68.2	68.3	51.4	5.6	24.2	18.7
GMS0508	68.3	68.4	36.4	41.2	14.5	8.0
GMS0508	68.4	68.5	10.7	78.5	4.3	6.5
GMS0508	68.5	68.6	19.3	72.5	3.3	4.8
GMS0508	68.6	68.7	37.5	25.9	22.9	13.8
GMS0508	68.7	68.8	47.5	5.0	21.0	26.5
GMS0508	68.8	68.9	53.5	10.4	19.2	16.8
GMS0508	68.9	69	46.5	9.6	6.9	37.0
GMS0508	69	69.1	48.7	6.7	24.7	19.9
GMS0508	69.1	69.2	63.8	4.3	23.3	8.5
GMS0509	69.2	69.3	68.1	3.5	20.0	8.4
GMS0509	69.3	69.4	57.5	5.1	32.1	5.2
GMS0509	69.4	69.5	57.1	9.4	25.2	8.3
GMS0509	69.5	69.6	44.0	14.2	37.5	4.3
GMS0509	69.6	69.7	51.1	19.0	14.8	15.1
GMS0509	69.7	69.8	60.5	2.9	11.0	25.7
GMS0509	69.8	69.9	68.1	3.6	12.6	15.6
GMS0509	69.9	70	63.1	2.1	11.4	23.3
GMS0509	70	70.1	49.2	3.9	5.6	41.2
GMS0509	70.1	70.2	48.2	12.8	6.7	32.3
GMS0509	70.2	70.3	52.5	6.5	2.3	38.7

Appendix 11: Twenty-five XRD cuttings samples mineral abundance database.

Mineral abundance %								
Sample I	depth_from (m)	depth_To(m)	XRD code	Quartz	Spodumene	Albite	Microcline	Muscovite
GMS0512	55.0	56.0	22067	21.9	12.2	33.2	9.9	22.8
GMS0513	56.0	57.0	22068	19.6	12.3	26.7	21.7	19.7
GMS0514	57.0	58.0	22069	29.2	14.1	21.4	10.9	24.4
GMS0515	58.0	59.0	22070	19.4	14.5	36.8	8.8	20.5
GMS0516	59.0	60.0	22072	21.5	19.3	29	8.7	21.5
GMS0517	60.0	61.0	22073	26.1	11.9	19.7	14.6	27.7
GMS0518	61.0	62.0	22074	20.7	14.3	29.9	15.2	19.9
GMS0519	62.0	63.0	22075	18.3	14.4	37.6	8.4	21.3
GMS0520	63.0	64.0	22076	24.7	9.9	24.6	17.2	23.6
GMS0521	64.0	65.0	22077	28.5	10.4	25.6	11.2	24.4
GMS0522	65.0	66.0	22078	23.8	10.9	26.3	18.6	20.4
GMS0523	66.0	67.0	22079	26.6	15.3	24.1	9.8	24.2
GMS0524	67.0	68.0	22082	19.9	11.3	29.9	18.5	20.4
GMS0525	68.0	69.0	22083	21.2	11.2	26.3	20.3	20.9
GMS0526	69.0	70.0	22084	17.7	9.8	16.2	27.9	28.5
GMS0527	70.0	71.0	22085	25.1	12.7	19.7	16.1	26.4
GMS0528	71.0	72.0	22100	23.2	12.3	20	17	27.6
GMS0529	72.0	73.0	22101	21.2	11.2	16.2	20.3	20.9
GMS0530	73.0	74.0	22102	25.3	12.5	19.7	15.6	23.6
GMS0531	74.0	75.0	22103	27.7	15.3	20	12.3	24.8
GMS0532	75.0	76.0	22104	24.4	15.3	26.3	13.4	23.8
GMS0533	76.0	77.0	22105	25.9	15.1	23.1	11.9	22.7
GMS0534	77.0	78.0	22106	13.9	10.4	19.9	25.8	29.3
GMS0535	78.0	79.0	22107	5.3	7.4	22.1	39.7	25.2
GMS0536	79.0	80.0	22108	23.3	16.1	24.4	7.2	22.6

Appendix 12: Database used for the quantitative analysis, including Hyperspectral imaging and XRD.

Sample ID	depth_from	depth_To	XRD code	Quartz_XRD	Quartz_HSI	Spodumene_XRD	Spodumene_HSI	Albite_XRD	Albite_HSI	Microcline_XRD	Microcline_HSI
GMS0512	55	56	22067	21.90	11.77	12.20	14.47	33.20	4.07	9.90	31.45
GMS0513	56	57	22068	19.60	16.94	12.30	13.18	26.70	2.77	21.70	30.40
GMS0514	57	58	22069	29.20	15.75	14.10	27.84	21.40	0.49	10.90	16.24
GMS0515	58	59	22070	19.40	12.36	14.50	22.04	36.80	1.04	8.80	25.99
GMS0516	59	60	22072	21.50	9.88	19.30	32.31	29.00	0.32	8.70	18.92
GMS0517	60	61	22073	26.10	21.04	11.90	10.26	19.70	0.43	14.60	9.71
GMS0518	61	62	22074	20.70	12.55	14.30	16.79	29.90	1.40	15.20	22.46
GMS0519	62	63	22075	18.30	15.01	14.40	22.55	37.60	1.52	8.40	18.08
GMS0520	63	64	22076	24.70	11.87	9.90	15.72	24.60	1.19	17.20	28.38
GMS0521	64	65	22077	28.50	23.46	10.40	18.52	25.60	1.88	11.20	16.83
GMS0522	65	66	22078	23.80	17.32	10.90	13.70	26.30	2.33	18.60	25.89
GMS0523	66	67	22079	26.60	20.60	15.30	19.71	24.10	1.74	9.80	11.81
GMS0524	67	68	22082	19.90	8.53	11.30	14.87	29.90	0.79	18.50	24.93
GMS0525	68	69	22083	21.20	11.49	11.20	11.54	26.30	1.95	20.30	22.29
GMS0526	69	70	22084	17.70	14.48	9.80	21.11	16.20	0.41	27.90	16.36
GMS0527	70	71	22085	25.10	16.19	12.70	21.99	19.70	1.12	16.10	13.34
GMS0528	71	72	22100	23.20	23.63	12.30	10.09	20.00	1.65	17.00	7.13
GMS0529	72	73	22101	21.20	18.69	11.20	10.36	16.20	1.69	20.30	12.22
GMS0530	73	74	22102	25.30	14.06	12.50	16.83	19.70	1.59	15.60	16.26
GMS0531	74	75	22103	27.70	16.08	15.30	23.34	20.00	0.69	12.30	11.66
GMS0532	75	76	22104	24.40	15.98	15.30	24.48	26.30	1.24	13.40	8.65
GMS0533	76	77	22105	25.90	17.25	15.10	19.11	23.10	1.56	11.90	10.00
GMS0534	77	78	22106	13.90	14.38	10.40	14.78	19.90	2.39	25.80	10.89
GMS0535	78	79	22107	5.30	12.31	7.40	31.10	22.10	0.71	39.70	10.49
GMS0536	79	80	22108	23.30	11.45	16.10	31.03	24.40	0.52	7.20	10.44

Appendix 13: spodumene crystals size analysis database

Sample ID	Depth_from	Depth_To	(longer axes)	(shorter axes)	Area(cm ²)	Area(mm ²)	(longer axes)	(shorter axes)	Area(cm ²)	Area(mm ²)	(longer axes)	(shorter axes)	Area(cm ²)	Area(mm ²)	Ave. crystals	Area(mm ²)
GMS0507	65.9	66	1.5	0.6	0.71	70.65	1.5	0.7	0.82	82.43	0.9	0.5	0.35	35.33		62.80
GMS0507	66	66.1	1.7	0.4	0.53	53.38	0.7	0.4	0.22	21.98	1	0.4	0.31	31.40		35.59
GMS0507	66.1	66.2	0.6	0.3	0.14	14.13	0.4	0.3	0.09	9.42	0.3	0.2	0.05	4.71		9.42
GMS0507	66.2	66.3	0.6	0.4	0.19	18.84	1	0.5	0.39	39.25	1.5	1	1.18	117.75		58.61
GMS0507	66.3	66.4	1	0.5	0.39	39.25	1	0.7	0.55	54.95	0.8	0.5	0.31	31.40		41.87
GMS0507	66.4	66.5	1	0.5	0.39	39.25	1.2	0.2	0.19	18.84	0.5	0.2	0.08	7.85		21.98
GMS0507	66.5	66.6	0.7	0.3	0.16	16.49	0.5	0.5	0.20	19.63	0.7	0.3	0.16	16.49		17.53
GMS0507	66.6	66.7	1	0.8	0.63	62.80	1.5	0.5	0.59	58.88	0.6	0.4	0.19	18.84		46.84
GMS0507	66.7	66.8	1.5	0.5	0.59	58.88	1	0.3	0.24	23.55	1	0.3	0.24	23.55		35.33
GMS0507	66.8	66.9	1	0.4	0.31	31.40	0.7	0.2	0.11	10.99	0.5	0.3	0.12	11.78		18.06
GMS0507	66.9	67	0.5	0.4	0.16	15.70	0.4	0.2	0.06	6.28	0.5	0.2	0.08	7.85		9.94
GMS0507	67	67.1	0.6	0.3	0.14	14.13	0.5	0.3	0.12	11.78	0.7	0.2	0.11	10.99		12.30
GMS0507	67.1	67.2	0.9	0.7	0.49	49.46	0.5	0.5	0.20	19.63	0.6	0.3	0.14	14.13		27.74
GMS0507	67.2	67.3	1.5	0.6	0.71	70.65	1.2	1	0.94	94.20	1	0.5	0.39	39.25		68.03
GMS0508	67.3	67.4	1.7	0.7	0.93	93.42	1	0.5	0.39	39.25	1.5	0.4	0.47	47.10		59.92
GMS0508	67.4	67.5	1.5	1	1.18	117.75	2.2	0.7	1.21	120.89	2	0.5	0.79	78.50		105.71
GMS0508	67.5	67.6	2.5	1.9	3.73	372.88	2	0.7	1.10	109.90	1.5	1	1.18	117.75		200.18
GMS0508	67.6	67.7	2	1	1.57	157.00	1.9	1.4	2.09	208.81	1.7	0.7	0.93	93.42		153.08
GMS0508	67.7	67.8	1.3	0.6	0.61	61.23	1.5	0.7	0.82	82.43	1	0.3	0.24	23.55		55.74
GMS0508	67.8	67.9	1.5	1	1.18	117.75	1.6	0.6	0.75	75.36	1.5	0.7	0.82	82.43		91.85
GMS0508	67.9	68	2.3	0.8	1.44	144.44	1.5	0.6	0.71	70.65	1	0.6	0.47	47.10		87.40
GMS0508	68	68.1	1	0.5	0.39	39.25	0.9	0.6	0.42	42.39	0.6	0.6	0.28	28.26		36.63
GMS0508	68.1	68.2	2	0.9	1.41	141.30	2	0.6	0.94	94.20	1	0.5	0.39	39.25		91.58
GMS0508	68.2	68.3	0.9	0.5	0.35	35.33	0.9	0.2	0.14	14.13	1	0.4	0.31	31.40		26.95
GMS0508	68.3	68.4	0.7	0.5	0.27	27.48	2.3	0.3	0.54	54.17	1	0.5	0.39	39.25		40.30
GMS0508	68.4	68.5	1.4	0.5	0.55	54.95	1	0.6	0.47	47.10	0.7	0.4	0.22	21.98		41.34
GMS0508	68.5	68.6	2.5	1.1	2.16	215.88	1.2	0.6	0.57	56.52	1	0.5	0.39	39.25		103.88
GMS0508	68.6	68.7	2.7	0.6	1.27	127.17	1.8	0.7	0.99	98.91	1	0.5	0.39	39.25		88.44
GMS0508	68.7	68.8	2	0.6	0.94	94.20	3	1.7	4.00	400.35	1	0.4	0.31	31.40		175.32
GMS0508	68.8	68.9	1.5	1.5	1.77	176.63	1.5	0.6	0.71	70.65	2.5	1.2	2.36	235.50		160.93
GMS0508	68.9	69	2	1.5	2.36	235.50	1.8	1.7	2.40	240.21	2.5	0.7	1.37	137.38		204.36
GMS0508	69	69.1	2.8	0.9	1.98	197.82	2.5	1.4	2.75	274.75	1.8	1	1.41	141.30		204.62
GMS0508	69.1	69.2	2	0.8	1.26	125.60	1.2	0.5	0.47	47.10	1.2	0.5	0.47	47.10		73.27
GMS0509	69.2	69.3	0.4	0.2	0.06	6.28	0.4	0.3	0.09	9.42	0.4	0.3	0.09	9.42		8.37
GMS0509	69.3	69.4	1.6	0.6	0.75	75.36	0.5	0.3	0.12	11.78	0.4	0.2	0.06	6.28		31.14
GMS0509	69.4	69.5	0.7	0.3	0.16	16.49	0.6	0.3	0.14	14.13	0.4	0.2	0.06	6.28		12.30
GMS0509	69.5	69.6	2.5	1.5	2.94	294.38	0.6	0.4	0.19	18.84	0.7	0.4	0.22	21.98		111.73
GMS0509	69.6	69.7	1.5	0.6	0.71	70.65	2	0.4	0.63	62.80	1	0.5	0.39	39.25		57.57
GMS0509	69.7	69.8	1.5	0.7	0.82	82.43	1.2	0.6	0.57	56.52	1	0.4	0.31	31.40		56.78
GMS0509	69.8	69.9	1.5	0.3	0.35	35.33	2	0.4	0.63	62.80	0.9	0.3	0.21	21.20		39.77
GMS0509	69.9	70	2.5	1.5	2.94	294.38	1.5	0.8	0.94	94.20	1.2	0.7	0.66	65.94		151.51
GMS0509	70	70.1	2	2	3.14	314.00	2	0.7	1.10	109.90	1.7	0.7	0.93	93.42		172.44
GMS0509	70.1	70.2	2	1	1.57	157.00	1	1	0.79	78.50	1.5	1	1.18	117.75		117.75
GMS0509	70.2	70.3	2	1	1.57	157.00	1.9	0.5	0.75	74.58	1.5	0.7	0.82	82.43		104.67

Appendix 14: Correlation statistical summary output of spodumene, quartz, microcline, and albite against mean spodumene crystal size.

SUMMARY OUTPUT OF MODAL SPODUMENE vs SPODUMENE CRYSTALS SIZE								
<i>Regression Statistics</i>								
Multiple R	0.66843							
R Square	0.44679							
Adjusted R Square	0.43330							
Standard Error	43.93488							
Observations	43.00000							
ANOVA								
	<i>df</i>	<i>SS</i>	<i>MS</i>	<i>F</i>	<i>Significance F</i>			
Regression	1.00000	63917.52358	63917.52358	33.11319	0.00000			
Residual	41.00000	79141.21520	1930.27354					
Total	42.00000	143058.73879						
	<i>Coefficients</i>	<i>Standard Error</i>	<i>t Stat</i>	<i>P-value</i>	<i>Lower 95%</i>	<i>Upper 95%</i>	<i>Lower 95.0%</i>	<i>Upper 95.0%</i>
Intercept	12.07115	12.97608	0.93026	0.35768	(14.13457)	38.27687	(14.13457)	38.27687
	19.27150	3.81649	0.66323	5.75441	0.00000	2.47707	5.15590	2.47707

SUMMARY OUTPUT OF MODAL ALBITE vs SPODUMENE CRYSTALS SIZE								
<i>Regression Statistics</i>								
Multiple R	0.059985713							
R Square	0.003598286							
Adjusted R Square	-0.020704195							
Standard Error	58.96339761							
Observations	43							
ANOVA								
	<i>df</i>	<i>SS</i>	<i>MS</i>	<i>F</i>	<i>Significance F</i>			
Regression	1	514.7662226	514.7662226	0.148062487	0.702382681			
Residual	41	142543.9726	3476.682258					
Total	42	143058.7388						
	<i>Coefficients</i>	<i>Standard Error</i>	<i>t Stat</i>	<i>P-value</i>	<i>Lower 95%</i>	<i>Upper 95%</i>	<i>Lower 95.0%</i>	<i>Upper 95.0%</i>
Intercept	82.71498512	19.59169771	4.221940658	0.000131046	43.14874891	122.2812213	43.14874891	122.2812213
	14.67622178	-0.416075748	1.081309161	-0.384788887	0.70238268	-2.5998239	1.767672404	-2.5998239

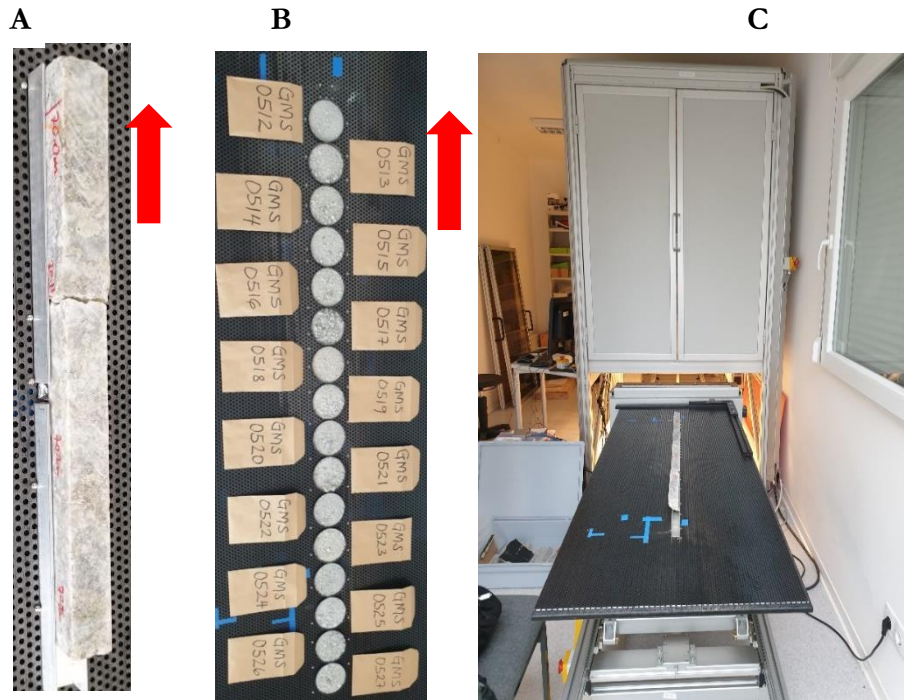
SUMMARY OUTPUT OF MODAL MICROCLINE vs SPODUMENE CRYSTALS SIZE									
<i>Regression Statistics</i>									
Multiple R	0.078384155								
R Square	0.006144076								
Adjusted R Square	-0.018096313								
Standard Error	58.88802418								
Observations	43								
ANOVA									
	<i>df</i>	<i>SS</i>	<i>MS</i>	<i>F</i>	<i>Significance F</i>				
Regression	1	878.9637177	878.9637177	0.253464407	0.617340492				
Residual	41	142179.7751	3467.799392						
Total	42	143058.7388							
	<i>Coefficients</i>	<i>Standard Error</i>	<i>t Stat</i>	<i>P-value</i>	<i>Lower 95%</i>	<i>Upper 95%</i>	<i>Lower 95.0%</i>	<i>Upper 95.0%</i>	
Intercept	79.36287422	11.17176857	7.103877395	1.17626E-08	56.80102988	101.9247186	56.80102988	101.9247186	
	21.15178626	-0.27686433	0.549931397	-0.503452488	0.617340492	-1.387473318	0.833744658	-1.387473318	0.833744658

SUMMARY OUTPUT OF MODAL QUARTZ vs SPODUMENE CRYSTALS SIZE									
<i>Regression Statistics</i>									
Multiple R	0.36107248								
R Square	0.13037333								
Adjusted R Squa	0.10916293								
Standard Error	55.0847892								
Observations	43								
ANOVA									
	<i>df</i>	<i>SS</i>	<i>MS</i>	<i>F</i>	<i>Significance F</i>				
Regression	1	18651.04461	18651.0446	6.14666829	0.01736859				
Residual	41	124407.6942	3034.334						
Total	42	143058.7388							
	<i>Coefficients</i>	<i>Standard Error</i>	<i>t Stat</i>	<i>P-value</i>	<i>Lower 95%</i>	<i>Upper 95%</i>	<i>Lower 95.0%</i>	<i>Upper 95.0%</i>	
Intercept	159.269379	34.61439363	4.60124712	4.0037E-05	89.364193	229.174565	89.364193	229.174565	
	44.90049297	-1.51193964	0.609838115	-2.47924753	0.01736859	-2.7435327	-0.28034658	-2.7435327	-0.28034658

Appendix 15: Hyperspectral cameras specification

Optical Characteristics	Typical Specification	
Stage Type: Lab stage	OWL-LWIR Camera	SWIR Camera
Spectral range	8-12 μm	1-2.5 μm
Spectral bands	84	288
Spectral resolution	100 nm	12 nm
Spectral sampling	48nm	5.6 nm
Spatial resolution	400 μm	384 μm
Pixel size	400 μm	24 x 24 μm
Frame rate	14.81	46.67
Exposure Time	0.95	10.42

(Sources:https://www.specim.fi/downloads/SWIR_SpeCam_ver4-15.pdf, https://www.specim.fi/wp-content/uploads/2021/02/Spectral-Cameras-LWIR_ver1-21.pdf),



A) Core sample and B) Cuttings samples on an aluminum scanning platform(Red arrow indicates hyperspectral camera scanning direction), C) hyperspectral cameras setup

Appendix 16: XRD sample preparation procedures



Appendix 17: XRD measurement using Bruker D2 phaser



Appendix 18: Twenty-five cuttings samples preparation procedures for hyperspectral imaging



Step 4: Sample drying



Step 4: Oven dry samples

